TIME RESOLVED OPTICAL STUDIES OF SPIN AND QUASIPARTICLE DYNAMICS IN FERROMAGNETIC THIN FILMS AND SUPERCONDUCTORS

by

YU GONG

A dissertation submitted to the Graduate Faculty in Physics in partial fulfillment of the
requirements for the degree of Doctor of Philosophy,
The City University of New York
2013

This manuscript has been read and accepted for the
Graduate Faculty in Physics in satisfaction of the
dissertation requirement for the degree of Doctor of Philosophy

Professor Yuhang Ren

Date

Chair of Examining Committee

Professor Steven Greenbaum

Date

Executive Officer

Professor Ying-Chih Chen

Professor Kai Shum

Professor Aidong Shen

Supervisory Committee

THE CITY UNIVERSITY OF NEW YORK

Abstract

Time Resolved Optical Studies of Spin and Quasiparticle Dynamics in Ferromagnetic Thin Films and Superconductors

by

Yu Gong

Adviser: Professor Yuhang Ren

This thesis presents the studies of spin and quasiparticle dynamics in ferromagnetic thin films and iron based superconductors by ferromagnetic resonance (FMR) and time-resolved pump-probe optical techniques.

First, the FMR spectroscopies were applied to study the spin dynamics both in frequency and time domains for the epitaxially grown Fe/GaAs thin films and FeCoB/Cr/FeCoB multilayer structures. In the single layer Fe/GaAs thin films, magnetization precessions were studied to characterize the magnetic dynamical parameters. Our results show that the magnetic crystalline anisotropy is dominative and the magnetic damping is strongly dependent on the in-plane magnetic field orientations. In FeCoB/Cr/FeCoB multilayer films, both the acoustic and the optical spin wave modes were identified in the FMR spectra. We reveal that the adjacent magnetic layers in the trilayer structures are antiferromagnetic coupled with an effective interlayer coupling constant J_{eff}. The magnetic dynamical parameters can be accurately optimized by the interlayer coupling constant J_{eff}.

Second, we employed the time-resolved pump-probe magneto-optical Kerr effect (MOKE) spectroscopy to study the spin dynamics in the Fe/GaAs thin films at picosecond time scale. The time-resolved MOKE results were combined with static magnetic hysteresis

loops at various time delays to understand the ultrafast demagnetization dynamics. The ultrafast demagnetization process is faster than the time required for the electron-phonon equilibration and therefore the spin-orbital coupling has to be included with the conventional electron thermalization model to understand our results. Moreover, we show that the ultrafast magnetization excitation and reorientation can be coherently controlled by varying the polarization of the pump beam. The magnetization excitation and reorientation are attributed to the laser induced effective magnetic field in the sample.

Third, the quasiparticle relaxation dynamics were studied in electron-doped $BaFe_{1.9}Ni_{0.1}As_2$ and $BaFe_{1.85}Co_{0.15}As_2$ superconductors by time-resolved pump-probe optical spectroscopy. Two distinct relaxation components observed in the transient reflectivity spectra are attributed to the quasiparticle recombination in the superconducting state and quasiparticle relaxations from the higher excited band due to the multiband excitation. The results show the multi-gap characteristic in $BaFe_{1.9}Ni_{0.1}As_2$ and $BaFe_{1.85}Co_{0.15}As_2$ superconductors. Moreover, the estimated electron-phonon coupling constant and the Coulomb pseudopotential indicate that the electron-phonon interaction is not large enough to induce the SC transition. A spin mediated pairing mechanism is necessary to understand the SC phase transition in the iron based superconductors.

Acknowledgements

I still remember the August of 2007 when I arrived at New York City and began my Ph.D career at the City University of New York. Time has been flying since then, silently. The life of a Ph.D candidate here is rhythmic, colorful and fruitful. All the memories of the previous years are precious to me. Looking back at those memories now, I realize that the most important things which have made me walk thus far are the help and encouragement of my mentors, family and friends.

First, I would like to thank my advisor, Prof. Yuhang Ren, for his guidance and mentoring throughout my Ph.D. career at Hunter College of the City University of New York. I feel blessed to work with Prof. Ren who is equipped with intensive knowledge of ultrafast optics and condensed matter physics. His insightful suggestions always broaden my mind in my research. Every time I encountered difficulties in the experiments, he would come and check the setup mirror by mirror, lens by lens, until problem solved. I could not reach the criteria of a Ph.D. degree without his encouragement and guidance. I also thank Prof. Ying-Chih Chen, Prof. Steve Greenbaum，Prof. Godfrey Gumbs and Prof. Leon Cohen at Hunter College, Prof. Kai Shum at Brooklyn College and Prof. Aidong Shen at City College for their generous help and comments to my research projects. Moreover, I would like to thank Prof. Guoping Zhang at Indiana State University who is our research collaborator. His insightful suggestions helped me a lot for understanding the results in my experiments. I would also like to thank Prof. Xinhui Zhang, Prof. Jianhua Zhao at Chinese Academy of Science and Prof. Nianxiang Sun at Northeastern University for providing the outstanding samples.

Second, I would like to appreciate the support from my family throughout my Ph.D. career. When I was in junior high school, I had no idea about my future career. My father gave me a science fiction novel called *Twenty Thousand Leagues under the Sea* by Jules Verne. I was obsessed by the exciting story and advanced technologies. Since then, I made up my mind to learn science and do research in the future. My parents also supported me and made me well educated until Master's degree in China. In addition, I would also like to thank my wife Bo Gao. Because of her assistance in my everyday life, I can focus more on my Ph.D. study. She always encourages me to go forward and work harder.

Furthermore, I would like to thank my former and current group members Wei lai, Mark Ebrahim, Zehra Cevher, Tetiana Nosuch and Ryan Kutayiah for their kind help and comments on my research. Special thanks to Dr. Phil Stallworth and Dr. Paul Sideris from Prof. Steve Greenbaum's group. They always helped me unreservedly. Also they provided me a lot of insightful discussions and comments to my research projects.

Finally, I would like to thank Ms. Diane Rock, Ms. Patricia Harris at Hunter College and Mr. Daniel Moy at Graduate Center for their great help to my Ph.D. studies.

Contents

Abstract iv
Acknowledgements vi
List of Tables x
List of Figures xi
Chapter 1 Introduction 1
  1.1 Spin dynamics in soft magnetic thin films 1
  1.2 Ultrafast magnetization dynamics in magnetic thin films 4
  1.3 Quasiparticle relaxation dynamics in *Fe* based superconductors 5
  1.4 Scope of the dissertation 7
Chapter 2 Theory of magnetization dynamics and quasiparticle relaxation dynamics 10
  2.1 Magnetization precessional dynamics in magnetic thin films 10
  2.2 Ultrafast optical detection of spin dynamics in magnetic thin films 16
  2.3 Ultrafast demagnetization dynamics 21
  2.4 Quasiparticle relaxation dynamics in FeAs based superconductors 24
Chapter 3 Experimental Techniques 30
  3.1 Samples 30
    3.1.1 Multilayer FeCoB/Cr/FeCoB thin films 30
    3.1.2 Epitaxially grown Fe/GaAs thin films 31
    3.1.3 Electron-doped iron-arsenic superconductors 32
  3.2 Ferromagnetic resonance technique 34
  3.3 Time-resolved pump-probe optical spectroscopy 36
    3.3.1 Femtosecond laser systems 36
    3.3.2 Mode-locked Ti: sapphire oscillator 37
    3.3.3 Autocorrelations of laser pulses 40
    3.3.4 Time-resolved pump-probe optical spectroscopy setups 43
    3.3.5 Time-resolved pump-probe MOKE spectroscopy 44
Chapter 4 Magnetization dynamics in magnetic single layer and trilayer structures 46
  4.1 Magnetization dynamics in iron thin film 46
    4.1.1 Brief theoretical description 46
    4.1.2 Magnetization precession spectrum with applied field along [100] axis 48
    4.1.3 Magnetization precession spectra with applied field along [1-10] axis 51
    4.1.4 Magnetization precession spectra under various applied field orientation 53
  4.2 Magnetization dynamics in FeCoB/Cr/FeCoB trilayer Structures 57
    4.2.1 Acoustic and Optical spin wave modes 57
    4.2.2 FMR linewidth and spin wave relaxation 65
Chapter 5 Non-thermal excitation and control of magnetization in Fe/GaAs thin film by femtosecond laser pulses 68
  5.1 Pump polarization dependent time-resolved pump-probe MOKE spectra 69
  5.2 Double Pump pulses induced magnetization excitation 75
Chapter 6 Ultrafast demagnetization in Fe/GaAs thin films 78
  6.1 Time-resolved pump-probe MOKE results 79
  6.2 Femtosecond demagnetization 79

6.3 Laser power dependent time-resolved hysteresis loops 83
Chapter 7 Ultrafast quasiparticle relaxation dynamics in electron-doped superconductor $BaFe_{1.9}Ni_{0.1}As_2$ and $BaFe_{1.85}Co_{0.15}As_2$ 87
7.1 Temperature dependent transient reflectivity spectra in BFNA 88
7.2 Distinct quasiparticle relaxations in BFNA 89
7.4 Distinct quasiparticle relaxations in BFCA 94
Chapter 8 Summary 97
References 99

List of Tables

Table 4.1 Interlayer coupling constant: Jeff and the effective in-plane uniaxial magnetic anisotropy: $2K_{\parallel}/M$ for samples with different Cr layer thicknesses. 63

List of Figures

Fig. 2.1 Stoner model of magnetism. Spin up and spin down electrons take up different density of states, the unequal of the occupation causes the magnetism. 10

Fig. 2.2 Magnetization precession and damping. The spiral trajectory stands for the magnetization vector precession and relaxation to the effective magnetic field direction. 12

Fig. 2.3 Geometry of sample setup. The φ is defined according to the in-plane easy axis. The θ is the angle between magnetization vector and the normal of the sample plane. φ_H and θ_H are the in-plane and out-of-plane angle of applied magnetic field, respectively. 13

Fig. 2.4 in phase and out of phase precession of the magnetization vector ***M*** in the ferromagnetic (FM)/non-magnetic (NM)/ferromagnetic (FM) layered structure. 15

Fig. 2.5 The geometry of the time-resolved pump-probe MOKE experiments. The applied magnetic field is along x-direction. The magnetization vector precesses in the *y-z* plane. The pump beam incidents normal to the sample plane. 17

Fig. 3.1 Sample geometry of multilayer FeCoB/Cr/FeCoB thin films. Ten periods of soft magnetic FeCoB/Cr/FeCoB sandwich layers and one 50 Å Cu seed layer were grown on the glass substrate. A series samples with *Cr* layer thickness varied from 4 to 40 angstroms were investigated in our experiments. 30

Fig. 3.2 Geometry of the single crystalline Fe/GaAs thin film. 10 nm iron thin film were epitaxially grown on the GaAs substrate. The [001] crystal axis are perpendicular to the sample plane. 31

Fig. 3.3 In-plane resistivity of BFNA (empty boxes). The superconducting transition is clearly identified at 20 K. The inset shows the conventional cell structure of $BaFe_2As_2$. 32

Fig. 3.4 Schematic of the conventional cavity-based FMR. The FMR measures absorption of microwave by magnetic materials under scanning magnetic field. The strong absorption peak is observed when the magnetization precession frequency matches with the applied microwave frequency. 34

Fig. 3.5 532 nm CW-Nd: vanadate Laser (Millennia Pro, Spectra Physics, right) and *Ti:sapphire* ooscillator system (Tsunami, Spectra Physcis, right). The broad band tunable *Ti:sapphire* oscillator is pumped by the 532 nm CW-Nd: vanadate laser . The system delivers 100 fs, 800 nm laser pulses with a repetition rate 82 MHz . .. 36

Fig. 3.6 Schematic of the optics and beam path in the Tsunami oscillator. 38

Fig. 3.7 Example of mode locking principle. The laser pulse train is generated by accumulating as many as laser modes with same phase in the cavity. The more in-phase modes are accumulated, the shorter pulse width and higher pulse intensity can be achieved. 39

Fig. 3.8 Intensity autocorrelation by second-harmonic generation. The delay stage controls the time delay between two isogenous pulses. The second harmonic generation signal can be detected when the two isogenous pulse reach the second harmonic crystal at the same time. 40

Fig. 3.9 Intensity autocorrelation obtained in our experiment by measuring the second harmonic generation signal as a function of time delay between the two isogenous laser pulses. The pulse width is around 100 femtoseconds. 41

Fig. 3.10 Spectrum distribution of the pulsed laser from an optical spectrum analyzer (Newport OSM-100-VIS/NIR). In our experiments, we tune the wavelength of both the pump an the probe beam to 800 nm and the bandwidth of laser beams were identified to be 15 nm. 42

Fig. 3.11 Schematic diagram for the time-resolved pump-probe optical spectroscopy setups. The reflectivity change of the probe beam is measured as a function of time delay between pump pulse and probe pulse. 43

Fig. 3.12 Schematic diagram for the time-resolved pump-probe MOKE spectroscopy setups. The polarization change of the probe beam is measured as a function of time delay between pump pulse and probe pulse. 44

Fig. 4.1 (a) Time-resolved pump-probe MOKE spectra for the Fe/GaAs thin film measured with a magnetic field applied along [100] easy axis. (b) Precessional time-resolved pump-probe MOKE data for various applied fields (solid lines) and simulated time-resolved pump-probe MOKE (surface) according to the Eq. (4.2). 48

Fig. 4.2 Measured magnetic-field dependence of the precession frequencies and fit. The precession frequency increases monotonically as a function of the applied magnetic field. The results are fit by Eq. (4.2). 50

Fig. 4.3 (a) Time-resolved pump-probe MOKE spectra for the Fe/GaAs thin film measured as magnetic field applied along [1-10] hard axis direction and their fit. (b) 3-D simulation (surface) of time-resolved pump-probe MOKE spectra as a function of magnetic field calculated according to Eq. (4.2). 51

Fig. 4.4 Measured precession frequencies as a function of applied magnetic field. The solid line shows the fit based on Eq. (4.2) by considering the magnetic field dependent equilibrium magnetization angle. 52

Fig. 4.5 Calculated φ as a function of applied magnetic field. In the case applied magnetic field is applied 45 degree compared to the magnetization vector, the magnetization vector rotates towards the magnetic field orientation as the magnetic field is increasing. 53

Fig. 4.6 Time-resolved pump-probe MOKE spectra for the Fe/GaAs thin film measured under various in-plane magnetic field angles (from 0 to 170 degree). The signal evolves periodically as a function of the applied magnetic field orientation...53

Fig. 4.7 Time-resolved pump-probe MOKE spectra for the Fe/GaAs thin film measured under various in-plane magnetic field angles (from 180 to 350 degree)..........54

Fig. 4.8 Magnetization precession frequency as a function of in-plane magnetic field orientation, the red solid line is the fit. The four-fold distribution of the magnetization frequency indicates that the in-plane cubic anisotropy is dominative. The results are fit by Eq. (4.2). 55

Fig. 4.9 Damping constant α as a function of in-plane magnetic field orientation. The distribution of the damping constant shows uniaxial dependence on the applied magnetic field orientation. The result is attributed to the uniaxial anisotropy in the sample plane. 56

Fig. 4.10 FMR resonance spectra as a function of magnetic field orientations in the sample with the 20-Å *Cr* layers measured under (a) in-plane configuration, (b) out-of-plane configuration. 57

Fig. 4.11 FMR spectrum in the sample with the 20-Å *Cr* layers. The red dashed lines show the deconvolution of the spectrum indicating an acoustic mode and an optical mode. The inset of the figure shows the schematic of these two modes. The in-phase precession refers to the acoustic spin wave resonance; the out-of-phase precession is attributed to the optical spin wave resonance...58

Fig. 4.12 Angular dependencies of resonance fields of the FMR spectrum in both (a) the in-plane and (b) the out-of-plane configurations for the sample with the 20 Å *Cr* layers. The solid lines show the fitting using Eq. (2.18) and (2.19) in chapter 2. The resonant field at $\theta_H \approx 0$ and 180° is a singularity and cannot be reached in our measurements. The two-fold result indicates the uniaxial anisotropic symmetry for the in-plane and the out of plane configurations as the applied field is rotated away from the easy axis..59

Fig. 4.13 Equilibrium angle of the magnetization, θ, as a function of the angle of the applied field θ_H in the out-of-plane configuration (φ = 0°). In the out-of-plane configuration, the magnetization can only be tilted to a small angle out of the sample plane by the applied magnetic field...60

Fig. 4.14 Angular dependence of resonance fields of the acoustic mode and optical mode in both (a) the in-plane and (b) the out-of-plane configurations for the sample with 20 Å *Cr* layers. The solid lines of the optical mode represent the fitting results using Eq. (2.20) and (2.21) in chapter 2. 61

Fig. 4.15 *Cr* layer thickness dependent out-of-plane effective anisotropy $2K_\perp/M$. The oscillatory behavior indicates the influence from the interlayer coupling. The dashed line is only meant to guide the eyes. 64

Fig. 4.16 FMR linewidth as a function of the in-plane applied field angle, φ, for the sample with 20 Å *Cr* layers. The solid red line shows the fitting result using Eq. (4.9)66

Fig. 4.17 FMR linewidth and magnetization damping constant α as a function of the thickness of *Cr* layers. Both of them show the oscillatory change, which is consistent with the variation of interlayer constant J_{eff}. This suggests that the interlayer coupling plays an important role in determining the magnetization relaxation dynamics in multilayer materials. The dashed line is only meant to guide the eyes. 66

Fig. 5.1 Time-resolved pump-probe MOKE spectrum at various pump polarization angle. The rapid jump in the first few picosecond of the time-resolved MOKE signal periodically appears as a function of the pump polarization. 69

Fig. 5.2 (a) Schematic diagram of the signal collection system. The output signal represents the rotation of reflected probe beam induced by the interaction between the sample and pump beam. (b) Definition of positive and negative excitation amplitude in the time-resolved pump-probe MOKE spectra. The positive excitation stands for the clockwise rotation of the reflective probe polarization, while the negative excitation is because of the counter-clockwise rotation of the reflected probe beam after pump pulse hits the sample. 70

Fig. 5.3 (a) Excitation amplitudes plot as a function of pump beam polarization angle. The excitation amplitudes show four-fold distribution as a function of the pump polarization. The reversal of the excitation from positive to negative appears close to the crystal axis. (b) Evolution of time-resolved MOKE spectra around the [-100] axis. The excitation gradually evolves from positive to negative as the pump polarization is rotated from the 262.70° to 263.02°. 72

Fig. 5.4 Magnetization excitation and reorientation mechanism. Under pump laser different polarization, the magnetization vector is excited and reoriented to the different direction followed by the precession and relaxation. 73

Fig. 5.5 Excitation amplitude vs. pump polarization angle from -0.4° to 0.5° compared to the [-100] axis. The hysteresis loop like result indicates that the magnetization is driven by an effective field induced by the femtosecond laser pulse in the sample. Inset shows the measurement configurations. 74

Fig. 5.6 (a) Time-resolved pump-probe MOKE spectra under the applied single pump polarization angle at -30° (pink) and -60° (red). The solid blue curve is the result when two pump beams were applied simultaneously. (b) Time-resolved pump-probe MOKE spectra under the applied single pump polarization angle at -30° (pink) and +30° (red). The solid blue curve is the result when two pump pulses were applied simultaneously. The three curves are offset for a better view. The polarizations of the double pump excitations are displayed in the inset. 75

Fig. 6.1 Time-resolved MOKE trace from -400 to 400 femtoseconds (blue dots). The autocorrelation is shown in red solid line. The inset shows the sample structure and the experimental geometry. The rapid decrease of the MOKE signal represents the ultrafast demagnetization process. 79

Fig. 6.2 (a) Time-resolved MOKE signal with step size 3.3 *fs*. The inset figures (b), (c), (d), (e), (f) show the time-resolved hysteresis loops at various time delays. The evolution of the time resolved hysteresis loops show an ultrafast demagnetization happens with in hundreds femtoseconds time scale. 80

Fig. 6.3 Intensity of the magnetic hysteresis loops as a function of time. Red solid line is the fitting to the intensity curve with exponential decay function. Inset shows the schematic diagram of the Elliot–Yafet type of spin scattering. 82

Fig. 6.4 (a), (b), (c), (d) show the hysteresis loops at ± 139 *fs* with various pump powers. The variation of the time-resolved hysteresis loop profile indicates that the electron thermalization model cannot fully explain the ultrafast demagnetization in our sample. 83

Fig. 6.5 Illustration of laser changing the magnetization under spin-orbital coupling mechanism. The electric field of the laser pulse alters the orbital momentum of the electrons. With the spin-orbital coupling, the spin momentum is changed corresponding to the orbital momentum. 84

Fig. 7.1 Transient reflectivity spectra under different temperature. Inset shows the fitting procedure. Two distinct quasiparticle relaxations and one long lived relaxation component are identified in our measured transient reflectivity signal. 88

Fig. 7.2 (a) Temperature dependent relaxation time, τ_{slow}, and (b) Temperature dependent relaxation amplitude, A_{slow}. The SC gap is extracted from the temperature dependent relaxation time, τ_{slow}, according to Kabanov's model. By using the extracted SC gap, the temperature dependent relaxation amplitude , A_{slow}, is well fitted. 89

Fig. 7.3 (a) Temperature dependent relaxation time, τ_{fast}, and (b) Temperature dependent relaxation amplitude, A_{fast} for the fast relaxation. The quasiparticle gap is extracted from the fitting to $A_{fast.}$ The inset demonstrates that fast relaxation process is governed by a cascade relaxation from the upper bound of Δ_G to that of the SC gap 91

Fig. 7.4 Amplitude of long-lived relaxation component vs temperature. The long-lived relaxation component is attributed to the relaxation of heat via diffusion. 94

Fig. 7.5 Experimental R_s/R_n ratio at three temperatures together with BCS single gap and two-gap fits at 5 *K*. $T = 27$ *K* data is used for R_n .The inset shows the temperature dependent $I^2\chi(\omega)$, the inverted electron boson spectral function in $BaFe_{1.85}Co_{0.15}As_2$. 95

Chapter 1 Introduction

The spin and quasiparticle dynamics in the materials triggers tremendous studies in the field of solid state physics for both the fundamental research and industrial application purposes. For example, investigations on the spin dynamics such as spin-orbital coupling, magnetic anisotropies and magnetic damping are essential to understand the spin correlations in magnetic films and nanostructures and therefore to improve the performance of magnetic devices. In this thesis, the spin and quasiparticle dynamics are discussed in magnetic thin films and iron based superconductors. For magnetic thin films, we use the results from ferromagnetic resonance experiments to reveal important dynamical magnetic properties. As an addition, we demonstrate ultrafast manipulation of magnetization by using the time-resolved pump-probe MOKE spectroscopy. Further, we present intriguing quasiparticle relaxation dynamics and discuss the paring mechanism in the recently discovered iron based superconductors.

1.1 Spin dynamics in soft magnetic thin films

Soft magnetic materials have attracted a lot of attention through recent years because of their potential applications in spintronics, magnetic sensors and microwave devices [1-5]. Among these, layered film structures such as exchange biased bilayers, have been studied extensively. The strong magnetic coupling between the ferromagnetic (FM) and antiferromagnetic (AFM) layers creates effective anisotropy as well as exchange bias in the ferromagnetic layer [6-9]. For example, Grimsditch *et al.* showed a large magnetic anisotropy was induced in the *Co* film by an antiferromagnetic FeF_2 substrate even well above its Neel temperature [13]. The result was explained by interactions of the ferromagnet with locally ordered regions within the antiferromagnet. Zhou *et al*. further revealed a large coercivity and a strong surface anisotropy field in *Co-Ni/FeMn* bilayers [10]. The local field is induced by ferromagnetic layer and determines the spin structure of antiferromagnetic layer. Compared with the bilayer structures, the hybrid sandwich FM/AFM/FM structures have shown unique advantages [11]. First, the sandwiched films have a higher effective magnetization resulting in a higher flux conduction capability and show excellent magnetic softness with a uniaxial anisotropy field and a low coercivity [11, 12]. Second, the magnetic behaviors of the FM/AFM/FM structures are influenced by the thickness of FM and AFM layers, crystalline phase growth conditions and strain between these juxtaposed crystalline layers. The relevant magnetic parameters include magnetic ordering temperature, magnetic anisotropy, magnetic axis, and magnetic coupling of magnetic layers through a non-magnetic or an AFM layer [13-16]. Moreover, they are the essential component required to build blocks of the so-called spin valves, which usually generate the giant magnetoresistance and other interesting magnetic properties [17-19].

The interlayer interactions between FM layers and between FM and AFM layers seem to be critical for controlling the magnetic properties in multilayer structures. In the case of rather thin (from several to tens of angstroms) interlayers; this interaction brings about the magnetic ordering [20]. Ferromagnetic or antiferromagnetic ordering of the neighboring ferromagnetic layers can be tuned by changing the thickness of the interlayer. For example, Planckaert *et al.* discussed the static magnetic ordering affected by the interlayer coupling in

Fe/FeSi/Fe trilayer [21]. Heinrich *et al.* showed that a long-range dynamic interaction is communicated by non-equilibrium spin currents in the *Fe/Cu/Fe* structure and the magnetic coupling between the Fe layers changes from FM to AFM as *Cu* interlayer thickness increases from several to tens of monolayers [22, 23]. The interlayer interactions also affect the dynamical performance of the multilayer structure [12, 24, 25]. Although much progress has been made in the past few years, there are still some fundamental problems regarding the underlying physics of magnetic interactions, exchange couplings, and magnetization relaxations. In particular, little is known about the dynamic magnetic properties of FM/AFM/FM structures, such as magnetic anisotropies, interlayer coupling, and the mechanism of magnetization damping, which are of great importance to assess the technological potential of these materials. Because of the high resistivity and relatively high saturation magnetization it can reach, the *FeCoB* alloys are desired for ultrahigh frequency devices such as future write heads and wireless inductors [26]. It is fundamentally important to investigate the magnetic dynamical properties of FM/AFM/FM sandwich structures based on *FeCoB*.

In this thesis, we present our investigations on the magnetic dynamic properties including magnetic anisotropies, spin wave modes, interlayer coupling, and magnetization damping of single layer iron thin films and multilayer FeCoB/Cr/FeCoB thin films. We answered some key questions raised from our experiments such as: How does the magnetic crystalline anisotropy affect the magnetization precession in ultra-thin magnetic films? How are the behaviors of the magnetization precessions different in single layer structures? What is the dependence of anisotropy field distribution on thicknesses of spacing AFM layers in soft magnetic FeCoB/Cr/FeCoB trilayer structures?

1.2 Ultrafast magnetization dynamics in magnetic thin films

Understanding of magnetism in the picosecond to sub-picosecond time scales becomes more and more important, due to demands on higher speed magnetic information storage devices and magnetic sensors [27-30]. Many groups have attempted to employ ultrafast laser pulses as a new means to control switching of magnetization at picoseconds (or less) [31-34]. In 2009, Rasing and his coworkers [35] realized a 30 ps inverse-Faraday writing in $Gd_{24}Fe_{66.5}Co_{9.5}$, where the magnetization switching occurs non-thermally without involving the spin reorientation or precession. Ultrafast magnetization dynamics in metallic films are more complex than those in ferromagnetic semiconductors. The magnetization reduction in metallic materials is usually mixed with the thermal effect caused by the strong absorption of pump laser pulses in ferromagnetic layers due to the weak spin orbital interactions. It has been a long challenge to find an effective non-thermal way to excite and control the magnetization reduction and therefore the coherent motion of its vector. Time-resolved pump-probe MOKE spectroscopy has been practically used in the studies of ultrafast laser-induced magnetization dynamics. Two pulse trains are employed in this technique, one is used as the pump beam, which triggers the magnetization dynamics, another is used as the probe beam, which detects the pump induced magnetization changes [36]. Analysis of the polarization of the probe beam after its interaction with the medium at various time delays between pump and probe pulses allows one to study the ultrafast laser-induced magnetization dynamics. The depictions of pump pulses on magnetic materials can be classified into thermal and non-thermal mechanisms. Thermal effects are usually described as follows: pump pulses deposit energy into the electron and phonon systems and magnetization change is due to the internal thermal equilibration processes [31]. Non-thermal effects include two possible schemes: 1) photons are absorbed via various electronic states that have a direct influence on magnetic parameters (e.g. magneto-crystalline anisotropies, spin-orbital coupling etc.) [37, 38]. 2) Circularly polarized laser pulses act as a magnetic field to reverse magnetization in a collinear M-H geometry [39]. The laser beam works as a short magnetic field pulse along the direction of the incident beam [35, 40].

In this thesis, the ultrafast magnetization dynamics were discussed in iron thin film by using the time-resolved pump-probe MOKE spectroscopy. Important questions are discussed including: What is the origin of the magnetization dynamics induced by the laser pulses on picosecond time scale? Are there any alternative mechanisms for ultrafast demagnetization in the femtosecond time scale?

1.3 Quasiparticle relaxation dynamics in *Fe* based superconductors

High temperature superconductivity discovered in iron pnictides has been the subject of attention due to their high superconducting (SC) transition temperature (as high as 56 K) and new possibilities to investigate unconventional superconducting mechanisms [41-45]. These new superconductors show some similar features with cuprates, such as anti-ferromagnetic (AF) parent compounds, doping induced superconductivity, and their layered crystal structure. However, they demonstrate unconventional s-wave band gap symmetry in SC characteristics [46, 47] and the existence of multi-gap superconducting gaps

[46]. *(Ba,K)*Fe_2As_2 was the first superconductor found in the 122 series (oxygen-free system); its superconducting transition temperature, T_C, can be as high as 38 K [48]. Its parent compound $BaFe_2As_2$ shows a first-order structural phase transition from tetragonal to orthorhombic with the simultaneous onset of long-range AF order around 140 K [49]. The presence of static AF ordering in the parent compounds and the remarkable similar doping dependent phase diagram to that of the high T_C copper oxides suggests that local AF fluctuations may also play an important role in the superconductivity of these materials. Indeed, recent neutron scattering measurements on spin fluctuations of powder samples of superconducting $Ba_{0.6}K_{0.4}Fe_2As_2$ (T_C = 38 K) and crystalline samples of $CeFeAsO_{0.84}F_{0.16}$ (T_C = 41 K) identified a clear evidence from the resonant-like magnetic peaks below T_C at $\hbar\omega \sim$ 14 meV and $\hbar\omega \sim$18.7 meV, respectively [50-54]. It is important to investigate the interplay between spin fluctuations and superconductivity in iron pnictides because spin fluctuations may indeed mediate electron pairing for superconductivity. Time-resolved pump-probe optical spectroscopic techniques are ideal to study quasiparticle (QP) dynamics involving SC gaps, spin fluctuations, and other ordering parameters [55-59], which are extremely important in establishing the microscopic picture of superconductivity in iron pnictides. Femtosecond pump-probe spectroscopy has been proven to be a superior tool to discriminate coexisting or competing phases such as the pseudogap phase [60], the suppression of superconductivity by antiferromagnetic phase [61], and the competition between spin density wave (SDW) and the precursor superconductivity phase [62]. In the SC states, SC gaps open in the QP density of states. In time-resolved pump-probe optical experiments, coherent pump photons break Cooper pairs and excite QPs into energy states far above the SC gaps. The subsequent

relaxation processes, recombination of the photo-excited carriers back into the superconducting condensate, are detected by probe pulses. Dynamic information on the low-lying electronic/spin states of superconductors can be obtained, when the QP relaxation and recombination are studied on a picosecond time scale as a function of temperature, polarization, and magnetic field.

In our research, the time-resolved pump-probe optical spectroscopy was employed to study the QP relaxation dynamics in the electron-doped superconducting single crystal, $BaFe_{1.9}Ni_{0.1}As_2$ (BFNA) and $BaFe_{1.85}Co_{0.15}As_2$ (BFCA). The mechanism of the quasiparticle relaxations observed in the transient reflectivity results were investigated based on the estimated quasiparticle energy gaps. The electron-phonon interaction contribution in the SC transition is discussed according to the theory described in Chapter 2.

1.4 Scope of the dissertation

Chapter 1 gives an introduction and motivations of our investigations on the spin dynamics in the soft magnetic thin films, the ultrafast magnetization dynamics in the single layer and multilayer ferromagnetic metallic thin films and the QP relaxation mechanism in the iron based superconductors.

Chapter 2 introduces the theoretical models of spin dynamics in the soft magnetic single layer and trilayer structures, the ultrafast magnetization dynamics in the ferromagnetic metallic thin films and the QP relaxations in the superconductors. The content of this chapter provides us the theoretical support for analyzing the experimental data in the following chapters.

Chapter 3 shows the samples geometry, laser systems and characterizations, and time-resolved pump-probe optical spectroscopy used in our experiments. Detailed descriptions of principles and setups are discussed for ferromagnetic resonance and time-resolved pump-probe optical spectroscopy.

Chapter 4 presents investigation on the magnetic dynamic properties of single layer iron thin film and multilayer FeCoB/Cr/FeCoB thin films by using time-resolved pump-probe MOKE optical spectroscopy and ferromagnetic resonance techniques. In single layer structures, the coherent spin precession trajectories were utilized to study the magnetic anisotropies and damping in the time domain. In trilayer structures, the spin wave model considering the interlayer coupling developed in chapter 2 is employed to understand the different spin wave modes observed in the ferromagnetic resonance spectra. The influence of the interlayer coupling on the magnetic dynamical parameters is discussed in the FeCoB/Cr/FeCoB samples with various thicknesses of the spacer layer.

Chapter 5 presents our study on the non-thermal manipulation of magnetization in Fe/GaAs thin films by time-resolved pump-probe MOKE optical spectroscopy. The coherently control of the magnetization excitation and reorientation were explored by varying the polarization of the pump.

Chapter 6 presents our investigations on ultrafast demagnetization in iron thin films by femtosecond laser pulses. The temporal evolution of the magnetic hysteresis loops was combined with time-resolved pump-probe MOKE to investigate the ultrafast demagnetization in iron thin film. The demagnetization dynamics is discussed according to the electron thermalization and spin-coupling mechanisms.

Chapter 7 presents our studies on the quasiparticle relaxation dynamics in electron-doped BFNA and BFCA superconductors over a wide range of temperature. The mechanism of the distinct quasiparticle relaxations is discussed according to Kabanov's model by considering the phonon scatterings. The paring mechanism of the quasiparticles in the iron based superconductor is discussed based on the calculated electron-phonon coupling constant and the pseudo coulomb potential.

Chapter 8 gives a summary of studies in this thesis.

Chapter 2 Theory of magnetization dynamics and quasiparticle relaxation dynamics

2.1 Magnetization precessional dynamics in magnetic thin films

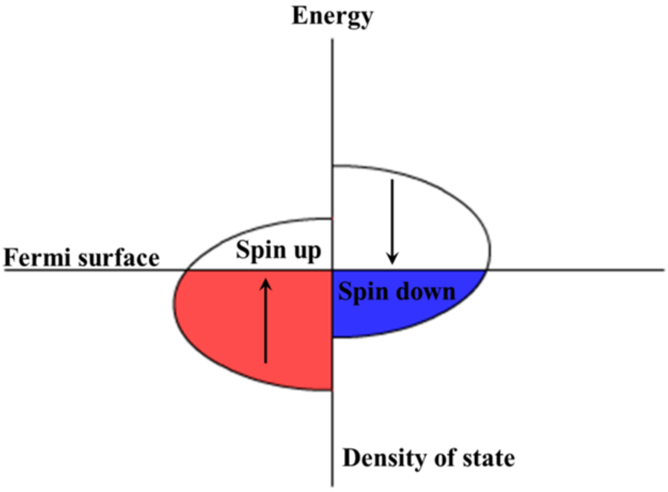

Fig. 2.1 Stoner model of magnetism. Spin up and spin down electrons take up different density of states, the unequal of the occupation causes the magnetism.

Magnetism is the phenomenon of the collective electron spins in the material. As described in simple Stoner model (Fig. 2.1), the spin up and spin down electron bands in the magnetic materials spontaneously split. If spin up or spin down electrons take up more density of states, there will be net spin which leads to magnetism.

In quantum mechanics, the time dependent spin dynamics can be described as:

$$i\hbar\frac{d}{dt}\boldsymbol{S} = [\boldsymbol{S}, \boldsymbol{\mathcal{H}}]. \tag{2.1}$$

in which $\boldsymbol{\mathcal{H}}$ is the Hamiltonian of spin, $\boldsymbol{S}$. When considering the interaction induced by the applied magnetic field H, the Hamiltonian is expressed as

$$\boldsymbol{\mathcal{H}} = -\frac{\mu_0 g \mu_B}{\hbar}\boldsymbol{S}\cdot\boldsymbol{H}. \tag{2.2}$$

in which μ_B is the Bohr magneton while g is the gyromagnetic factor for a free electron. For example, the Z-component of the commutator in Eq. 2.1 can be expanded as:

$$[\boldsymbol{S_z}, \boldsymbol{\mathcal{H}}] = -\frac{\mu_0 g \mu_B}{\hbar}\left[\boldsymbol{S_z}, \boldsymbol{S_x H_x} + \boldsymbol{S_y H_y} + \boldsymbol{S_z H_z}\right] = -\frac{\mu_0 g \mu_B}{\hbar}\left([\boldsymbol{S_z}, \boldsymbol{S_x}]\boldsymbol{H_x} + [\boldsymbol{S_z}, \boldsymbol{S_y}]\boldsymbol{H_y}\right). \quad (2.3)$$

Commutation relation of the spin operators yields:

$$[\boldsymbol{S_i}, \boldsymbol{S_j}] = i\hbar\varepsilon_{ijk}S_k., \quad (2.4)$$

Hence, equation 2.3 can be written as:

$$[\boldsymbol{S_z}, \boldsymbol{\mathcal{H}}] = -i\mu_0 g \mu_B\left(\boldsymbol{H_x S_y} - \boldsymbol{H_y S_x}\right). \quad (2.5)$$

Therefore, the other components can be expressed as:

$$[\boldsymbol{S_x}, \boldsymbol{\mathcal{H}}] = -i\mu_0 g \mu_B\left(\boldsymbol{H_y S_z} - \boldsymbol{H_z S_y}\right), \quad (2.6)$$

$$\left[\boldsymbol{S_y}, \boldsymbol{\mathcal{H}}\right] = -i\mu_0 g \mu_B(\boldsymbol{H_z S_x} - \boldsymbol{H_x S_z}). \quad (2.7)$$

Combing the Eq. 2.5, 2.6 and 2.7, we can write Eq. 2.1 as:

$$\frac{d}{dt}\boldsymbol{S} = -\mu_0\gamma(\boldsymbol{H} \times \boldsymbol{S}), \quad (2.8)$$

in which $\gamma = g\mu_B/\hbar$ is the gyromagnetic ratio.

In magnetic materials, the magnetization vector is the summation of the magnetic moments of net electron spins. The relation between magnetization, ***M***, magnetic moments, ***μ*****,** and spin, ***S*****,** can be expressed as:

$$\begin{aligned} M &= \sum \mu_i, \\ \mu &= -\gamma\hbar S. \end{aligned} \quad (2.9)$$

Therefore, the motion of magnetization under external magnetic field can be expressed as:

$$\frac{dM}{dt} = -\mu_0\gamma\left(M \times H\right). \quad (2.10)$$

In magnetic materials, however, the applied magnetic field is not the only source which induces torque to the spin; therefore, *H* is substituted by the effective field, $H_{eff,}$ which includes external magnetic field, magneto-crystalline anisotropy, magnetic shape anisotropy exchange field, etc. After this modification, we obtain the famous Landau–Lifshitz (LL) equation:

$$\frac{dM}{dt} = -\gamma\left(M \times H_{eff}\right). \tag{2.11}$$

The term $-\gamma\left(M \times H_{eff}\right)$ acts as the torque on the magnetization vector. A consequence of this equation is, under disturbance or absorption of energy, if the magnetization vector is not well aligned with the effective field orientation, it will do precessional motion around the vector H_{eff}.

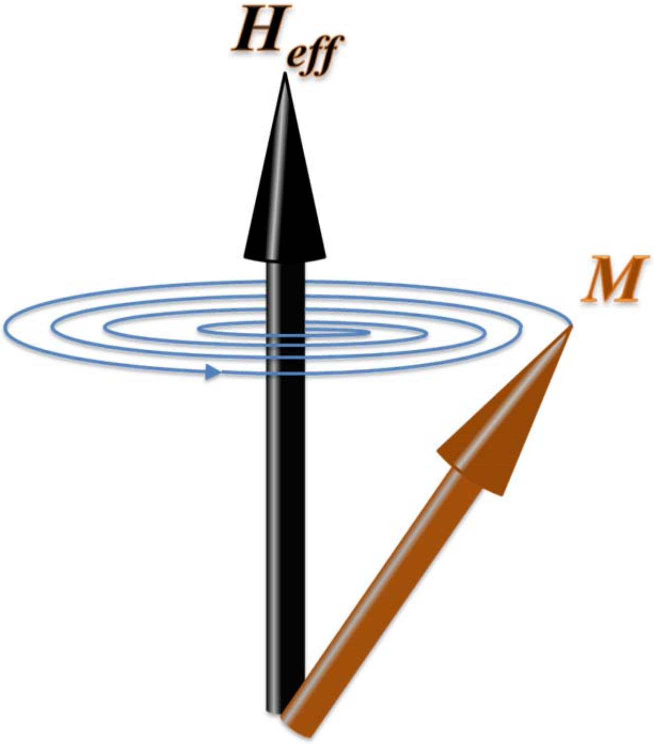

Fig. 2.2 Magnetization precession and damping. The spiral trajectory stands for the magnetization vector precession and relaxation to the effective magnetic field direction.

In the experiments, the magnetization eventually aligns with the effective field as shown in Fig. 2.2. This experimentally observable fact demands the introduction of a dissipation term into the LL equation. Gilbert initially induced the damping term,

$$\frac{\alpha}{M}\left(M\times\frac{dM}{dt}\right) .$$

By adding the damping term to Eq. (2.11), the equation of motion is expressed as the so-called Landau-Lifshitz-Gilbert (LLG) equation [63-65]:

$$\frac{dM}{dt}=-\gamma\left(M\times H_{eff}\right)+\frac{\alpha}{M}\left(M\times\frac{dM}{dt}\right). \qquad (2.12)$$

where α is the Gilbert damping constant. The ferromagnetic damping is the energy dissipation process through which precessional (in Gigahertz) magnetization motion comes to an end. Understanding and controlling ultrafast magnetization dynamics is crucial to the spintronic devices' performance.

In magnetic recording devices, the magnetic multilayer structures are more favorable compared to single layer structures due to the tunability of magnetic properties by the interlayer couplings.

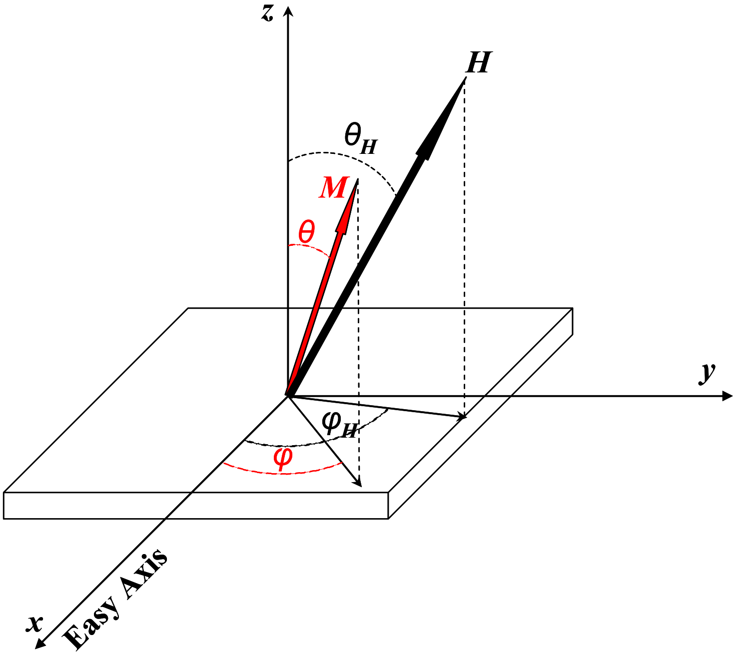

Fig. 2.3 Geometry of sample setup. The φ is defined according to the in-plane easy axis. The θ is the angle between magnetization vector and the normal of the sample plane. φ_H and θ_H are the in-plane and out-of-plane angle of applied magnetic field, respectively.

In order to understand the distribution of the magnetic dynamical parameters, we introduce the free energy of the trilayer system with two FM layers as:

$$
\begin{aligned}
F = {} & \sum_{i=1}^{2}\Big[-d_i M_i H\left(\sin\theta_i \sin\theta_H \cos(\varphi_i-\varphi_H)+\cos\theta_i\cos\theta_H\right)+ \\
& -d_i(2\pi M_i^{2}-K_{\perp}^{i})\sin^2\theta_i - d_i K_{//}^{i}\sin^2\theta_i\cos^2\varphi_i\Big]+ \\
& -J_{\text{inter}}\left[\sin\theta_1\sin\theta_2\cos(\varphi_1-\varphi_2)+\cos\theta_1\cos\theta_2\right].
\end{aligned}
\tag{2.13}
$$

where d_i is the thickness and M_i is the magnetization of each FM layer. H is the applied magnetic field. θ_i, θ_H, φ_i, and φ_H, show the orientation of the magnetization and magnetic field in different FM layers with respect the normal of the sample plane and in-plane easy axis respectively as shown in Fig. 2.3. $K_\perp$ and $K_\parallel$ are the out-of-plane uniaxial and in-plane uniaxial anisotropy constant. The J_{inter} term is included in the free energy formula which describes the interlayer coupling between the FM layers. The dispersion relation of spin wave resonances is calculated by applying the equation of resonance frequency of the form [66]:

$$
a\omega^4 + b\omega^2 + c = 0 \quad . \tag{2.14}
$$

where

$$
a = \frac{d_1^2 M_1^2 \sin^2\theta_1}{\gamma_1^2}\frac{d_2^2 M_2^2 \sin^2\theta_2}{\gamma_2^2} \quad . \tag{2.15}
$$

$$
\begin{aligned}
b = {} & \left(F_{\theta_1\varphi_1}^2 - F_{\theta_1\theta_1}F_{\varphi_1\varphi_1}\right)\frac{d_2^2 M_2^2 \sin^2\theta_2}{\gamma_2^2} + \left(F_{\theta_2\varphi_2}^2 - F_{\theta_2\theta_2}F_{\varphi_2\varphi_2}\right)\frac{d_1^2 M_1^2 \sin^2\theta_1}{\gamma_1^2} + \\
& + 2\left(F_{\theta_1\varphi_2}F_{\theta_2\varphi_1} - F_{\theta_1\theta_2}F_{\varphi_1\varphi_2}\right)\frac{d_1 d_2 M_1 M_2 \sin\theta_1 \sin\theta_2}{\gamma_1\gamma_2} \quad .
\end{aligned}
\tag{2.16}
$$

$$
\begin{aligned}
c = {} & F_{\theta_1\theta_2}^2 F_{\varphi_1\varphi_2}^2 + F_{\theta_1\varphi_1}^2 F_{\theta_2\varphi_2}^2 + F_{\theta_1\varphi_2}^2 F_{\theta_2\varphi_1}^2 - F_{\theta_1\theta_2}^2 F_{\varphi_1\varphi_1} F_{\varphi_2\varphi_2} - F_{\varphi_1\varphi_2}^2 F_{\theta_1\theta_1} F_{\theta_2\theta_2} + \\
& - F_{\theta_2\varphi_2}^2 F_{\theta_1\theta_1} F_{\varphi_1\varphi_1} - F_{\theta_1\varphi_2}^2 F_{\theta_2\theta_2} F_{\varphi_1\varphi_1} - F_{\theta_1\varphi_1}^2 F_{\theta_2\theta_2} F_{\varphi_2\varphi_2} - F_{\theta_2\varphi_1}^2 F_{\theta_1\theta_1} F_{\varphi_2\varphi_2} + \\
& + F_{\theta_1\theta_1} F_{\varphi_1\varphi_2} F_{\theta_2\theta_2} F_{\varphi_2\varphi_2} + 2F_{\theta_1\theta_1} F_{\varphi_1\varphi_2} F_{\theta_2\varphi_1} F_{\theta_2\varphi_2} + 2F_{\theta_1\varphi_1} F_{\theta_1\varphi_2} F_{\varphi_1\varphi_2} F_{\theta_2\theta_2} + \\
& + 2F_{\theta_1\theta_2} F_{\theta_1\varphi_2} F_{\varphi_1\varphi_1} F_{\theta_2\varphi_2} + 2F_{\theta_1\theta_2} F_{\theta_1\varphi_1} F_{\theta_2\varphi_1} F_{\varphi_2\varphi_2} - 2F_{\theta_1\theta_2} F_{\varphi_1\varphi_2} F_{\theta_1\varphi_2} F_{\theta_2\varphi_1} + \\
& - 2F_{\theta_1\varphi_1} F_{\theta_2\varphi_2} \left(F_{\theta_1\theta_2} F_{\varphi_1\varphi_2} + F_{\theta_1\varphi_2} F_{\theta_2\varphi_1} \right)
\end{aligned}
\quad . \tag{2.17}
$$

In Eq. (2.17) and (2.17), the free energy terms are differentiated two times with respect to θ and φ. The γ stands for gyromagnetic ratio that is ~ 1.835×10^{11}Hz/T in our experiment. There are two solutions In Eq. (2.14) which are $\left(\omega^{\pm}\right)^2 = \left(-b \pm \sqrt{b^2 - 4ac}\right)/2a$, corresponding to the in-phase and the out-of-phase processions frequency (ω^+ and ω^-) of M_1 and M_2 in the two neighboring FM layers. The precessions are named as acoustic mode and optical mode [67] of the magnetic trilayer structure as shown in Fig. 2.4.

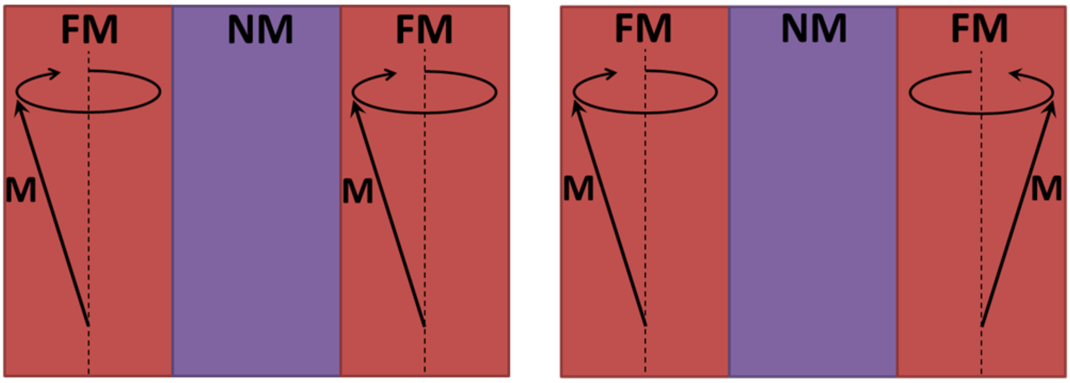

In phase precession **Out of phase precession**

Fig. 2.4 in phase and out of phase precession of the magnetization vector ***M*** in the ferromagnetic (FM)/non-magnetic (NM)/ferromagnetic (FM) layered structure.

The frequencies of the acoustic mode related to the in-plane and out-of-plane resonance fields are written as:

$$
\left(\frac{\omega^+}{\gamma}\right)^2 = \left(H_R^a - \frac{2K_{//}}{M}\cos 2\varphi\right) \times \left(H_R^a + 4\pi M - \frac{2K_\perp}{M} + \frac{2K_{//}}{M}\sin^2\varphi\right) .
$$

(2.18)

$$\left(\frac{\omega^{+}}{\gamma}\right)^{2}=\left(H_{R}^{a}\cos\left(\theta_{H}-\theta\right)-(4\pi M-\frac{2K_{\perp}}{M})\cos 2\theta\right)\times\left(H_{R}^{a}\cos\left(\theta_{H}-\theta\right)-(4\pi M-\frac{2K_{\perp}}{M})\cos^{2}\theta-\frac{2K_{//}}{M}\right).$$

(2.19)

while the equations of the in-plane and out-of-plane resonance fields for the optical mode are written as:

$$\left(\frac{\omega^{-}}{\gamma}\right)^{2}=\left(H_{R}^{o}-\frac{2K_{//}}{M}\cos 2\varphi-J_{eff}\right)\times\left(H_{R}^{o}+4\pi M-\frac{2K_{\perp}}{M}+\frac{2K_{//}}{M}\sin^{2}\varphi-J_{eff}\right).$$

(2.20)

$$\left(\frac{\omega^{-}}{\gamma}\right)^{2}=\left(H_{R}^{a}\cos\left(\theta_{H}-\theta\right)-(4\pi M-\frac{2K_{\perp}}{M})\cos 2\theta-J_{eff}\right)\times\left(H_{R}^{a}\cos\left(\theta_{H}-\theta\right)-(4\pi M-\frac{2K_{\perp}}{M})\cos^{2}\theta-\frac{2K_{//}}{M}-J_{eff}\right).$$

(2.21)

The above equations were applied to fit the dependence of the observed mode frequencies upon the strength and orientation of the static field. We extract the values of the anisotropy, exchange bias and exchange coupling constants for multilayer FM materials.

2.2 Ultrafast optical detection of spin dynamics in magnetic thin films

In the time-resolved pump-probe MOKE technique, two steps need to be considered to detect the spin dynamics. The first step is the generation of the coherent spin precession by pump pulses and the second step is the scattering of probe pulses due to the generated spin precesions and relaxations.

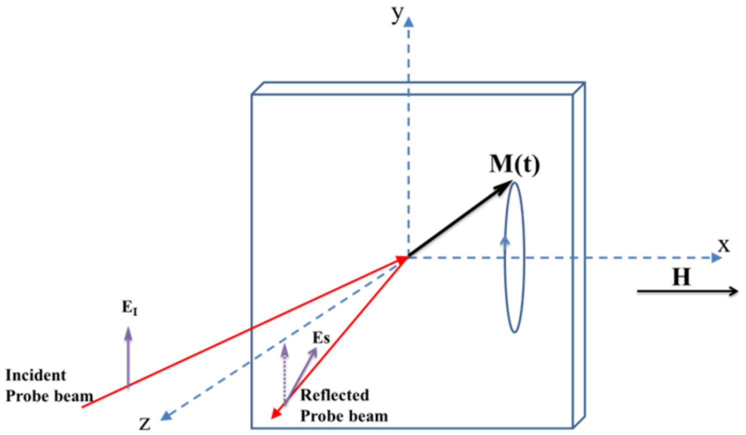

Fig. 2.5 The geometry of the time-resolved pump-probe MOKE experiments. The applied magnetic field is along x-direction. The magnetization vector precesses in the *y*-*z* plane. The pump beam incidents normal to the sample plane.

The pump-probe geometry is in so called Voigt scheme as shown in Fig. 2.5. The pump beam is nearly perpendicularly incident to the sample plane. The external magnetic field is applied along the *x*-direction. Under the pump laser excitation, the magnetization vector precesses in the *y*-*z* plane. The magnetization precession induces the polarization change in the probe beam.

In our detection scheme, the coherent scattering field is associated with a slow varying modulation of the refractive index [68]:

$$\delta n_R(t) = (2\pi\chi_M / Ln_R)\int_{-L/2}^{L/2} m_z(z,t)dz = (2\pi\chi_M / n_R)\langle m_z\rangle. \qquad (2.22)$$

where n_R is the refractive index, $\chi_M = \frac{\partial\chi^{(0)}}{\partial M}$, and $\chi^{(0)}$is the linear susceptibility. There are three preconditions for Eq. (2.22): 1) $L \cdot n_R/c \ll 2\pi/\Omega$ where L is the layer thickness, Ω is the spin precession frequency. 2) The light penetration depth (~100 nm) is >> L. 3) Multiple reflections can be ignored. These preconditions are well satisfied in the materials we investigated and our experiments.

In a ferromagnetic system, the Hamiltonian of the spin system can be written as:

$$\tilde{\mathrm{H}} = -J\sum_{j,\delta}\mathbf{S}_{\mathrm{J}}\cdot\mathbf{S}_{\mathrm{J}+\delta} - g\mu_B\sum_{j}\mathbf{S}_{\mathrm{J}}\cdot H_0 - \varepsilon g\mu_{\mathrm{B}}G\mathbf{E}_{\mathrm{S}}\times\mathbf{E}_{\mathrm{I}}^{*}\cdot\mathbf{S}_{\mathrm{I}}\,. \tag{2.23}$$

where the first term represent the spin-spin interaction, the second term is the Zeeman energy, the third term stands for the interaction between the optical field and a single spin in a cubic system [69]. The coefficient G describes the efficiency of spin-orbital and electric-dipole couplings. The $\boldsymbol{E_S}$ and $\boldsymbol{E_I}$ are the electric field of the incident and scattered laser beam.

The polarization change of the reflected probe beam is measured by a balanced detector. The magnetic susceptibility for a cubic system is written as [69]:

$$\chi^{ij}(M) = \begin{bmatrix} \chi & -iGm_z & iGm_y \\ iGm_z & \chi & -iGm_x \\ -iGm_y & iGm_x & \chi \end{bmatrix}. \tag{2.24}$$

After the excitation by the pump beam, the evolutions of spin component in y- and z-direction are written as $m_y(t) = C\cdot m_y(z)\cos(\Omega t)$, $m_z(t) = C\cdot m_z(z)\sin(\Omega t)$ where t is the time delay between the pump and probe pulses. The change in the susceptibility due to coherent spin precession is:

$$\delta\chi^{ij}(M) = \frac{\partial\chi^{ij}(M)}{\partial M}\delta M = \begin{bmatrix} 0 & -iGCm_z\sin\Omega t & iGCm_y\cos\Omega t \\ iGCm_z\sin\Omega t & 0 & 0 \\ -iGCm_y\cos\Omega t & 0 & 0 \end{bmatrix}.$$

(2.25)

The polarization induced by the response of each spin precession to the probe pulse ($E \parallel y$) is:

$$\vec{P} = \delta\chi^{ij}(M)\vec{E}^{*}(r,t) = -iGm_z(z,t)\cdot E(z)e^{-i\Omega t}\,\hat{e}_x\,. \tag{2.26}$$

The scattered radiation interferes with the reflected probe pulses. By considering the fact that spin precession frequency is much lower than the laser frequency (~ 375 THz for an 800 nm laser). The total electric field satisfies the Maxwell equations:

$$\frac{\partial^2\vec{E}}{\partial z^2} - \frac{n(z)^2}{c^2}\frac{\partial^2\vec{E}}{\partial t^2} = \mu\frac{\partial^2\vec{P}}{\partial t^2} = \mu\frac{\partial^2}{\partial t^2}\left(-iGm_z(z,t)\cdot E(z)e^{-i\Omega t}\,\hat{e}_x\right) = i\mu Gm_z(z)\Omega^2 E(z)e^{-i\Omega t}\,\hat{e}_x\,.$$

(2.27)

Assume that $\vec{E}^{(0)} = e^{-i\Omega t}E_{\Omega}^{(0)}(z)\hat{e}_y$ represents a general solution of the homogeneous wave equation:

$$\frac{\partial^2 \vec{E}}{\partial z^2} - \frac{n(z)^2}{c^2}\frac{\partial^2 \vec{E}}{\partial t^2} = 0 \cdot \tag{2.28}$$

where $n(z) = 1$ for $z > l/2$ (in the vacuum), $n(z) = n$ for $z < l/2$. The z-dependent part can be solved to be:

$$\begin{aligned} E_{\Omega}^{(0)}(z) &= e^{-i\frac{\Omega}{c}z} + re^{i\frac{\Omega}{c}z} \quad (z > l/2), \\ E_{\Omega}^{(0)}(z) &= te^{-i\frac{n\Omega}{c}z} \quad (z < l/2). \end{aligned} \tag{2.29}$$

where r and t are the reflectivity and transmittivity coefficients for the electric field. The time-independent perturbation method is applied to calculate the scattered field. The total field with the contribution from the scattering of the induced polarization is

$$\vec{E}' = e^{-i\Omega t}\vec{E}_{\Omega}(z) = e^{-i\Omega t}\left(E_{\Omega}^{(0)}(z)\hat{e}_y + \sum_{\omega} C_{\omega}E_{\omega}^{(0)}(z)\hat{e}_x \right). \tag{2.30}$$

Substituting the above expression into Eq. (2.27) yields:

$$\left(\frac{\partial^2}{\partial z^2} - \frac{n(z)^2}{c^2}\frac{\partial^2}{\partial t^2}\right)\sum_{\omega} C_{\omega}E_{\omega}^{(0)}(z)e^{-i\Omega t}\hat{e}_x = i\mu G m_z(z)\Omega^2 E_{\Omega}^{(0)}(z)e^{-i\Omega t}\hat{e}_x \cdot \tag{2.31}$$

where C_{ω} is the perturbation coefficient. By neglecting the small terms, the Eq. (2.31) is simplified:

$$\sum_{\omega} C_{\omega}\left(-\frac{n^2(z)\omega^2}{c^2} + \frac{n^2(z)\Omega^2}{c^2}\right)E_{\omega}^{(0)}(z) = i\mu G m_z(z)\Omega^2 E_{\Omega}^{(0)}(z) \cdot \tag{2.32}$$

Using the normalizing condition:

$$\frac{1}{E_{probe}^2}\int n^2(z)E_{\omega'}^{*(0)}(z)E_{\omega}^{(0)}(z)dz = \delta(\omega-\omega')\,. \tag{2.33}$$

Multiplying both sides of Eq. (2.31) by $\int dzn^2(z)E_{\omega'}^{*(0)}(z)$ yields:

$$C_{\omega'} = i\mu G\Omega^2 \frac{c^2}{n^2(z)}\left(\frac{1}{\Omega^2-\omega'^2}\right)\int n^2(z')E_{\omega'}^{*(0)}(z')m_z(z')E_{\Omega}^{(0)}(z')dz',$$

$$\vec{E}_{\Omega}(z) = E_{\Omega}^{(0)}(z)\hat{e}_y + E_{\omega}^{(0)}(z)\sum_{\omega} i\mu G\Omega^2 \frac{c^2}{n^2(z)}\left(\frac{1}{\Omega^2-\omega'^2}\right)\int n^2(z')E_{\omega'}^{*(0)}(z')m_z(z')E_{\Omega}^{(0)}(z')dz'\hat{e}_x\,. \tag{2.34}$$

For $z > 0$,

$$\vec{E}_{\Omega}(z) = E_{\Omega}^{(0)}(z)\hat{e}_y + i\mu G\Omega^2 E_{probe}c^2\sum_{\omega}\left(\frac{e^{-i\frac{\omega}{c}z}+re^{+i\frac{\omega}{c}z}}{\Omega^2-\omega'^2}\right)\int n^2(z')E_{\omega'}^{*(0)}(z')m_z(z')E_{\Omega}^{(0)}(z')dz'\hat{e}_x.$$

(2.35)

The single pole at *Ω* = *ω*\` is considered as the other pole *Ω* =– *ω*\` is not physical meaningful. For $z > 0$, $\Omega = \omega - \mathrm{i}\Gamma$, including the decay term Γ, should be used in order to satisfy causality. In addition, only the term that travels in the positive *z*-direction needs to be retained.

$$\vec{E}_{\Omega}(z) = E_{\Omega}^{(0)}(z)\hat{e}_y + E_{probe}\mu G\Omega c^2\, 2\pi re^{i\frac{\Omega}{c}z}\int n^2(z')E_{\Omega}^{*(0)}(z')m_z(z')E_{\Omega}^{(0)}(z')dz'\hat{e}_x\,.$$

(2.36)

where the integral is over the thin film and the field is $E_{\Omega}^{(0)}(z) = te^{-i\frac{n\Omega}{c}z}$ which yields:

$$\vec{E}_{\Omega}(z) = E_{probe}\left(e^{-i\frac{\Omega}{c}z}+re^{i\frac{\Omega}{c}z}\right)\hat{e}_y + E_{probe}\mu G\Omega c^2\, 2\pi rt^2n^2e^{i\frac{\Omega}{c}z}\int m_z(z')dz'\hat{e}_x\,.$$

(2.37)

The second term in the above expression is the coherent scattered field. The polarizations of the reflected (with a reflection coefficient *r*) and scattered probe are rotated by 45^0 using a half wave-plate. The balance-detected signal yields:

$$
\begin{aligned}
I &= \left| \frac{rE_{probe} + E_s}{\sqrt{2}} \hat{e}_x \right|^2 - \left| \frac{rE_{probe} - E_s}{\sqrt{2}} \hat{e}_y \right|^2 = 2rE_{probe}E_s^* \\
&= 2r^2 E^2{}_{probe} \mu G \Omega c^2 2\pi t^2 n^2 \int m_z(z,t)dz = 4\pi r^2 t^2 n^2 E^2{}_{probe} \mu G \Omega c^2 \int m_z(z)dz
\end{aligned}
.
$$

(2.38)

The results prove the magnetic origin of the time-resolved pump-probe MOKE signal which is directly related to the temporal change of magnetization in the sample. The mechanism described in this section is fundamental to our studies of ultrafast magnetization dynamics bytime-resolved laser spectroscopy.

2.3 Ultrafast demagnetization dynamics

Under laser excitation, the interactions between electron and spin, lattice and spin are crucial to understand the ultrafast demagnetization dynamics. In 2005, a model that explains the ultrafast equilibration of magnetic order in ferromagnetic metals was developed [70]. The model is based on the Hamiltonian incorporated with Elliot-Yafet type of spin-flip scattering [71] in which the electrons interact with impurities or phonons. The spin-orbit interactions dominate scattering processes and transfer the angular momentum between the electrons and lattice. The Hamiltonian is expressed as:

$$
\begin{aligned}
&H = H_e + H_s + H_{ee} + H_{si}, \\
&H_{si} = \frac{\lambda_{si}}{N} \sum_k \sum_{k'} \sum_j^{Ns} c_k^\dagger c_{k'} (s_{j,+} + s_{j,-}).
\end{aligned}
\tag{2.39}
$$

in which H_e and H_s are the Hamiltonians for electron and spin systems respectively, H_{ee} is the Coulomb term. H_{si} is the spin-flip term. $c_k^\dagger$ and $c_{k'}$ are the creation and annihilation of the k state electrons. $s_{j,+}$ and $s_{j,-}$ stand for the flip-up or -down of the spin j. λ_{si} is the concentration of the impurity. From the Hamiltonian, the rate of the spin change after the photo excitation can be obtained which is expressed as:

$$\tau_M = \frac{C_0 F(T/T_c)}{\pi D_F^2 \lambda_{si}^2} \frac{\hbar}{k_B T_c}. \tag{2.40}$$

in which the constant is $C_0 = 1/4$ when demagnetization process is much slower than that of electron-phonon equilibrium and $C_0 = 1/8$ in the reverse case. $F(T/T_c)$ is a dimensionless factor which depends on the ratio between T and Tc. D_F is density of states of the spinless electrons.

Most recently, Koopmans *et al*, [72] developed a microscopic three temperature model (M3TM), which treat the spin excitations with a mean-field Weiss model. Based on the model, three coupled differential equations are derived:

$$\begin{aligned} &C_e[T_e]\frac{dT_e}{dt} = \nabla_z(\kappa \nabla_z T_e) + g_{ep}(T_p - T_e), \\ &C_p\frac{dT_p}{dt} = g_{ep}(T_e - T_p), \\ &\frac{dm}{dt} = Rm\frac{T_p}{T_c}(1 - m\coth(\frac{mT_c}{T_e})). \end{aligned} \tag{2.41}$$

where ∇_z is the differentiation along z direction(perpendicular to the film surface), κ is the electronic thermal conductivity, the electron and phonon temperature T_p and T_e are all z dependent. The model successfully explained the ultrafast laser pulse induced demagnetization in both the magnetic materials with magnetization contributed from the 3d4sp electron bands and the 5d6sp electron bands. The obtained demagnetization time τ_M agrees well with the experimental results. However, there still needs studies which consider more electronic band structure and spin excitation spectrum.

In addition to the electron thermalization model, the spin-orbital coupling mechanism which describes the laser induced ultrafast demagnetization through the interaction between the orbital momentum and spin momentum also attracts a lot of attentions [73-75]. The Hamiltonian under the Heisenberg model with the spin-orbital coupling can be expressed as [75]:

$$H = -\sum_{ij} J_{ij}(R_{ij}) S_i \cdot S_j + \sum_i \lambda(R_i) L_i \cdot S_i. \tag{2.42}$$

where the first term is the exchange interactions between spins with J_{ij} as exchange coupling constant. The second term represents the spin-orbital coupling. R_{ij} is a position vector. $\lambda(R_i)$, S_i and L_i is the spin-orbital coupling constant, spin and orbital operators at position R_i, respectively. The ultrafast laser pulses induce an additional term, H_i to the Hamiltonian:

$$H_i = \frac{e}{mc} \sum_i P_i \cdot A(t). \tag{2.43}$$

in which e and c are the electron charge and the speed of light, respectively, m stands for the electron mass, p represents the electron momentum operator while $A(t)$ is the time-dependent vector potential of the laser field. With the laser pulse and the spin-orbital coupling effect, the time-dependent orbital momentum can be expressed as:

$$\hbar\frac{dL_{ix}}{dt}=\frac{1}{i}[L_{ix},H_{soc}+HI]=\lambda(R_i)(L_{iz}S_{iy}-L_{iy}S_{iz})$$
$$+\frac{e}{mc}[p_{iz}A_y(t)-p_{iy}A_z(t)],$$
$$\hbar\frac{dL_{iy}}{dt}=\frac{1}{i}[L_{iy},H_{soc}+HI]=\lambda(R_i)(L_{ix}S_{iz}-L_{iz}S_{ix})$$
$$+\frac{e}{mc}[p_{ix}A_z(t)-p_{iz}A_x(t)],$$
$$\hbar\frac{dL_{iz}}{dt}=\frac{1}{i}[L_{iz},H_{soc}+HI]=\lambda(R_i)(L_{iy}S_{ix}-L_{ix}S_{iy})$$
$$+\frac{e}{mc}[p_{iy}A_x(t)-p_{ix}A_y(t)].$$

(2.44)

in which H_{soc} is the second term in Eq. 2.42. The three differential equations show that under each of the polarization orientation, the laser manipulates two components of orbital momentum. Because of the entanglement of spin components and orbital momentum, an orbital momentum change along one direction must consequently change the spin components along other directions. The spin-orbital coupling model is utilized to discuss the temporal variation of the hysteresis loop and ultrafast demagnetization mechanism in our experiments.

2.4 Quasiparticle relaxation dynamics in FeAs based superconductors

The time-resolved pump-probe experiments have been applied to the traditional high temperature superconductors [76-78]. It has been found that the amplitude and relaxation time of the transient photo-induced reflectivity or transmission is strongly related to the superconducting gap in the photo-excited quasiparticle density of states. Kabanov et al [79], discussed the quasiparticle relaxation in the $YBa_2Cu_3O_{7-\delta}$ superconductor. The approximate distribution functions of non-equilibrium phonon: n_{ω_q} and quasiparticle (f_ε) take the form [80]:

$$n_{\omega_q} = \begin{cases} \dfrac{1}{\exp(\frac{\hbar\omega_q}{k_B T}) - 1}, \hbar\omega_q < 2\Delta \\ \dfrac{1}{\exp(\frac{\hbar\omega_q}{k_B T'}) - 1}, \hbar\omega_q > 2\Delta \end{cases}, \qquad (2.45)$$

$$f_\varepsilon = \frac{1}{\exp(\frac{\varepsilon}{k_B T'}) + 1}.$$

in which ω_q is the phonon frequency, ε is the quasiparticle energy, T is the lattice temperature and T' is the temperature of quasiparticle. Δ is the quasiparticle energy gap. Considering the number of the photo-excited quasiparticles is much less than that of the quasiparticles under T and $n_T = 2N(0)k_B T exp(-\Delta/k_B T)$ (*N(0)* is the density of states at Fermi level), the number of the photo-excited quasiparticles is written as:

$$n_{pe} = \frac{E_I / \Delta}{1 + \frac{2\nu}{N(0)\hbar\Omega_c} \exp[-\Delta / k_B T]}. \qquad (2.46)$$

in which ν is the effective number of phonon modes per unit cell participating in the relaxation, Ω_c, stands for the phonon frequency cut off, E_I represents the absorbed laser energy density per unit cell. If Δ is temperature dependent, then $n_T \approx 2N(0)\sqrt{\frac{\pi\Delta(\mathrm{T})k_B T}{2}} exp(-\Delta(\mathrm{T})/k_B T)$ [81]. The number of the photo-excited quasiparticles should be modified as:

$$n_{pe} = \frac{E_I / (\Delta(T) + k_B T / 2}{1 + \frac{2\nu}{N(0)\hbar\Omega_c} \sqrt{\frac{2k_B T}{\pi\Delta(T)}} \exp[-\Delta(T) / k_B T]}. \qquad (2.47)$$

The reflectivity change and transmittance change signal in the pump-probe measurement are all proportional to this quantity.

Moreover, the relaxation rate of the photo-excited quasiparticles is determined by the energy transfer from high frequency phonons ($\hbar\omega > 2\Delta$) to relatively low frequency phonons ($\hbar\omega < 2\Delta$). By considering the phonon-phonon scattering [82], the kinetic equation for the energy can be written as:

$$\frac{\partial E_{<}}{\partial t} = \sum_{q(\omega_q < 2\Delta)} \hbar\omega_q I_{ph-ph}\{n_\omega\},$$

$$I_{ph-ph}\{n_\omega\} = 2\pi \sum_{q_1,q_2} \left|w_{q_1,q_2}\right|^2 \left\{ \begin{array}{l} \frac{1}{2}[(n_\omega+1)n_{\omega 1}n_{\omega 2} - n_\omega(n_{\omega 1}+1)(n_{\omega 2}+1)]\delta(\omega-\omega_1-\omega_2) \\ +[(n_\omega+1)(n_{\omega 1}+1)n_{\omega 2} - n_{\omega 1}n_{\omega 2}(n_{\omega 2}+1)]\delta(\omega_2-\omega-\omega_1) \end{array} \right\}.$$

(2.48)

in which $W_{q1,q2}$ is the coupling constant and n_ω represents the phonon distribution function. In Debye approximation, the phonon density of states is $\rho(\omega) = 3\nu\omega^2/\Omega_c^3$. The total phonon energy that satisfies $\hbar\omega < 2\Delta$ is written as:

$$E_{<} = \int_0^{2\Delta} n_\omega \rho(\omega)\hbar\omega d\omega = \frac{8\nu k_B T\Delta^3}{(\hbar\Omega_c)^3}. \tag{2.49}$$

The kinetic equation for the energy, after considering the condition that $\Delta \ll \hbar\Omega_c$ takes the form:

$$\frac{8\nu k_B \Delta^3}{(\hbar\Omega_c)^3}\frac{\partial T}{\partial t} = \frac{8}{3}\pi w^2 \left[\frac{3\nu}{(\hbar\Omega_c)^2}\right]^3 k_B^2 T'(T'-T)\Delta^4. \tag{2.50}$$

which is further simplified as:

$$\frac{\partial T}{\partial t} = \frac{9\pi\nu^2 w^2 k_B T'\Delta(T)}{(\hbar\Omega_c)^3}(T'-T). \tag{2.51}$$

Therefore, the reciprocal of the relaxation rate is written as:

$$\frac{1}{\tau} = \frac{9\pi\nu^2 w^2 k_B T'\Delta(T)}{(\hbar\Omega_c)^3}. \tag{2.52}$$

Under low temperature $k_BT \ll \hbar\omega$, the Raman phonon linewidth $\Gamma_\omega \simeq \frac{3\pi w^2 v^2 \omega^2}{4\hbar\Omega_c^3}$ is applied into the expression of the relaxation rate which takes the form:

$$\frac{1}{\tau} = \frac{12\Gamma k_B T'\Delta(T)}{\hbar\omega^2}. \tag{2.53}$$

The k_BT' under low temperature ($T < T_c$) can be estimated by $n_{T'} - n_T = E_I / \Delta(0)$ and considering $n_T \simeq 2N(0)\Delta(0)\exp[-\Delta(T)/k_BT$. The relaxation rate of quasiparticles under the temperature $0 < T < T_c$ is written as:

$$\frac{1}{\tau} = \frac{12\Gamma_\omega \Delta(T)^2}{\hbar\omega^2 \ln\{1/[E_I/2N(0)\Delta(0)^2 + \exp\left(-\Delta(T)/k_BT\right)]\}}. \tag{2.54}$$

The electron-phonon coupling is important to understand the superconducting mechanism. Under the illumination of laser pulses, electrons are first pumped from the ground states to the excited states. After that, the excited electrons relax via the relaxation energy to the lattice and spin system. In the electron bath, the electron-electron thermalization time can be expressed as $\tau_{e\text{-}e} \sim \hbar E_f/2\pi E^2$ [83] in which the E is the carrier energy obtained from the Fermi energy, E_f. The time scale of this electron-electron thermalization is usually in several femtoseconds scale. Because this time scale is much shorter than our laser pulse duration (~ 100 *fs*), it is reasonable to think the electron-electron thermalization as instantaneous. In this case, we can define the temperature of the illuminated electron system as T_e. Usually, the heat capacity of the electron is much small than that of the lattice, the electron temperature can reach thousand degrees higher than the lattice under the illumination.

The energy dissipated via the electron-phonon interaction has been studied by the model which applied the thermal distribution functions f_K and n_Q to the system of electron and phonons [84]. The time dependence of the distribution functions is expressed as:

$$\frac{\partial f_k}{\partial t} = -\frac{2\pi}{\hbar N_c}\sum_Q \left|M_{kk'}\right|^2 \{f_k(1-f_{k'})[(n_Q+1)\delta(\varepsilon_k-\varepsilon_{k'}-\hbar\omega_Q)+n_Q\delta(\varepsilon_k-\varepsilon_{k'}+\hbar\omega_Q)]$$
$$-(1-f_k)f_{k'}[(n_Q+1)\delta(\varepsilon_k-\varepsilon_{k'}+\hbar\omega_Q)+n_Q\delta(\varepsilon_k-\varepsilon_{k'}-\hbar\omega_Q)]\},$$

$$\frac{\partial n_Q}{\partial t} = -\frac{4\pi}{\hbar N_c}\sum_k \left|M_{kk'}\right|^2 f_k(1-f_{k'})[n_Q\delta(\varepsilon_k-\varepsilon_{k'}+\hbar\omega_Q)-[(n_Q+1)\delta(\varepsilon_k-\varepsilon_{k'}-\hbar\omega_Q)].$$

(2.55)

in which k and Q are the wave vectors of electrons and phonons, respectively, N_c represents the number of unit cells in the sample, the $M_{kk'}$ stands for the electron-phonon matrix elements. If the electron mean free path is too short to match the optical skin depth, the rate of the electron temperature change can be expressed as a simple form in the model:

$$\frac{\partial T_e}{\partial t} = \gamma_T(T_l - T_e),$$

(2.56)

$$\gamma_T = \frac{3\hbar\lambda\left\langle\omega^2\right\rangle}{\pi k_B T_e}\left[1-\frac{\hbar^2\left\langle\omega^4\right\rangle}{12\left\langle\omega^2\right\rangle k_B^2 T_l T_e}+\ldots\right].$$

in which $\lambda < \omega^n >= 2\int_0^\infty [\alpha^2 F(\Omega)/\Omega]\Omega^n d\Omega$. α^2 is the electron-phonon coupling strength while $F(\Omega)$ is the phonon density states. Based on Eq. (2.56) we can extract the electron-phonon coupling constant. The electron-phonon coupling constant is an important factor in the investigation of superconductivity, since the superconducting transition is ascribed to the electron-lattice correlation at low temperature.

The equations in this section were utilized to analyze our temperature dependent transient reflectivity results of Fe-based superconductor, from which the important parameters such as photo-excited quasiparticle gaps and electron-phonon coupling constant etc. can be extracted. The obtained quasiparticle gaps helped us understand the quasiparticle excitation and relaxation mechanism. The extracted electron-phonon coupling constant suggests that the electron-phonon interaction is not strong enough to induce the SC transition. A non-electron-phonon mediated quasiparticle pairing mechanism was included in Fe based superconductor.

Chapter 3 Experimental Techniques

In this chapter, we present some details of samples and experimental setups we employed for investigating dynamical electron, phonon and spin properties of ferromagnetic thin films and iron based superconductors.

3.1 Samples

Our experimental results are based on three different kinds of samples including multilayer FeCoB/Cr/FeCoB thin films, epitaxially grown Fe/GaAs thin films and electron-doped superconductor $BaFe_{1.9}Ni_{0.1}As_2$ and $BaFe_{1.85}Co_{0.15}As_2$ single crystals.

3.1.1 Multilayer FeCoB/Cr/FeCoB thin films

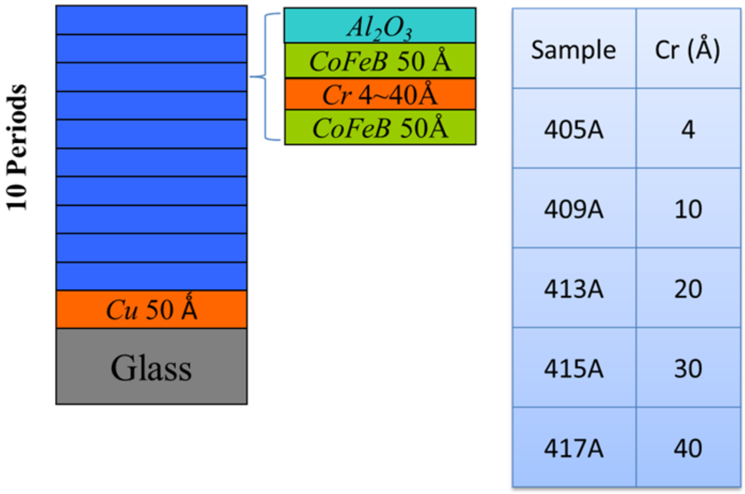

Sample	Cr (Å)
405A	4
409A	10
413A	20
415A	30
417A	40

Fig. 3.1 Sample geometry of multilayer FeCoB/Cr/FeCoB thin films. Ten periods of soft magnetic FeCoB/Cr/FeCoB sandwich layers and one 50 Å Cu seed layer were grown on the glass substrate. A series samples with *Cr* layer thickness varied from 4 to 40 angstroms were investigated in our experiments.

The structure of multilayer FeCoB/Cr/FeCoB samples applied in our experiments is shown in Fig. 3.1. Ten periods of trilayers composed of FeCoB/Cr/FeCoB were deposited on

Cu/Glass substrate and coated with Al_2O_3 layer by *dc* magnetron sputtering with base pressure in the order of 10^{-9} Torr. The composition ratio of Co:Fe:B is 2:2:1. In order to investigate how the interlayer coupling affects the magnetic dynamical properties, the thickness of the *FM* layers was fixed at 50 Å. We varied the thickness of Cr layer from 4 Å to 40 Å. During the deposition procedure, a uniaxial anisotropy field was introduced by applying magnetic field annealing. The sample preparation and characterization were carried out at Prof. N. X. Sun's lab at the Northeastern University.

3.1.2 Epitaxially grown Fe/GaAs thin films

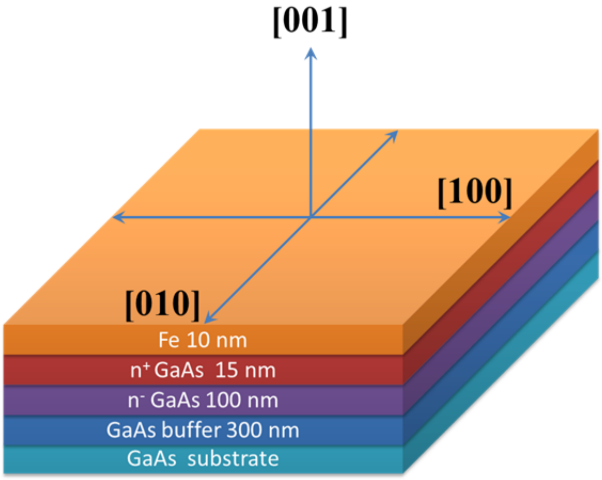

Fig. 3.2 Geometry of the single crystalline Fe/GaAs thin film. 10 nm iron thin film were epitaxially grown on the GaAs substrate. The [001] crystal axis are perpendicular to the sample plane.

In order to study the ultrafast manipulation of magnetization by femtosecond laser pulses in soft magnetic thin films, 10 nm Fe thin films were grown on the GaAs substrate by low temperature molecular beam epitaxy (MBE) technique. Two vacuum chambers were used to grow the GaAs buffer layer and the Fe film separately. Two chambers were connected by an ultrahigh vacuum preparation chamber. A reflection high-energy electron diffraction

(RHEED) detector was employed to in-vivo monitor the surface reconstruction. GaAs (300 nm) /n$^-$-GaAs(100 nm) /n$^+$-GaAs (15 nm) buffer layers were first grown on the oxide-desorbed GaAs [001] semi-insulating substrates at 560 °C in the growth chamber I. After cooling down to room temperature, the substrates were transferred to the growth chamber II through the preparation chamber under ultrahigh vacuum condition. Then the Fe thin film was deposited on top of it with the temperature below 50 °C. The epitaxial relationship of Fe thin film and GaAs substrate was confirmed by the RHEED patterns along different crystal axis orientations. The magnetization exhibits a hard axis out-of-plane along [001] crystal axis, and uniaxial in-plane anisotropy superimposed on a four-fold cubic anisotropy [85-89]. The samples were prepared by Professor Xinhui Zhang and Professor Jianhua Zhao's groups at the State Key Laboratory for Superlattices and Microstructures, Institute of Semiconductors, Chinese Academy of Sciences.

3.1.3 Electron-doped iron-arsenic superconductors

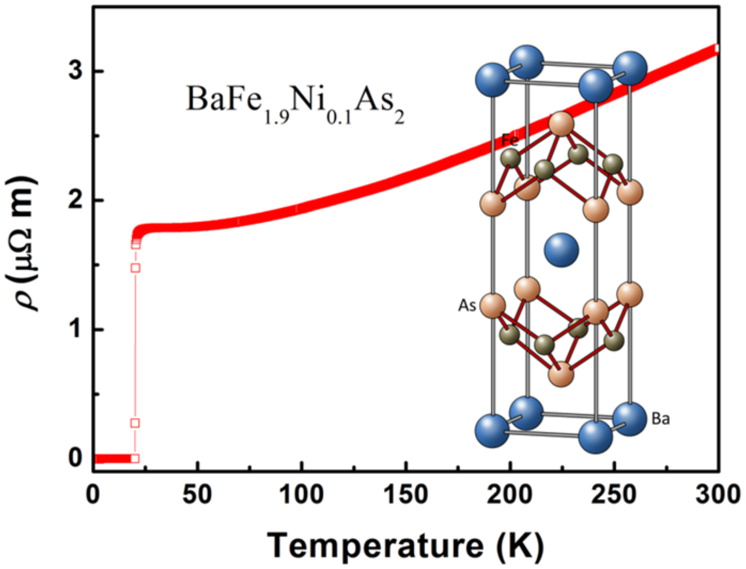

Fig. 3.3 In-plane resistivity of BFNA (empty boxes). The superconducting transition is clearly identified at 20 K. The inset shows the conventional cell structure of $BaFe_2As_2$.

In order to investigate the pairing mechanisms of quasiparticles in the recent discovered iron arsenide superconductors, single crystalline electron-doped superconductors $BaFe_{1.9}Ni_{0.1}As_2$ (sizes ~ 3 × 2 × 0.3 mm^3) and $BaFe_{1.85}Co_{0.15}As_2$ (sizes ~ 6 × 5 × 0. 3 mm^3) were grown by self-flux method [90] in Prof. Zhuan Xu's lab at the Physics Department of the Zhejiang University. The actual Ni and Co concentrations were confirmed to be 0.1 and 0.15 separately by Energy Dispersive X-ray microanalysis. The *ab*-plane resistivity was measured using a standard four-probe method (the result is shown in Fig. 3.3.) The superconducting transition of $BaFe_{1.9}Ni_{0.1}As_2$ single crystal, which takes place at 20 K in the sample, is very sharp with a transition region of < 0.7 K, indicating the excellent quality of the single crystal. The superconductivity in the iron based compound [91] is intriguing because iron and magnetic impurities generally damage the formation of superconductivity. The structure of parent material $BaFe_2As_2$ is shown in the inset of Fig. 3.3. The magnetic phase transition temperature of the parent compound appears at $T_N \sim 140$ K. It remains metallic below the transition temperature [92], which is different from the conventional cuprates superconductors. The superconductivity can be achieved by doping Ni and Co into the parent compound. The close relation between the magnetic order and superconductivity in these compounds [93] suggests that there may be a different origin of the quasiparticle pairing mechanism existing in this kind of materials. In our study, the quasiparticle relaxations in the time domain are investigated as a function of temperature, which helps us to understand the quasiparticle excitation and relaxation mechanism in the $BaFe_{1.9}Ni_{0.1}As_2$ and $BaFe_{1.85}Co_{0.15}As_2$ compound.

3.2 Ferromagnetic resonance technique

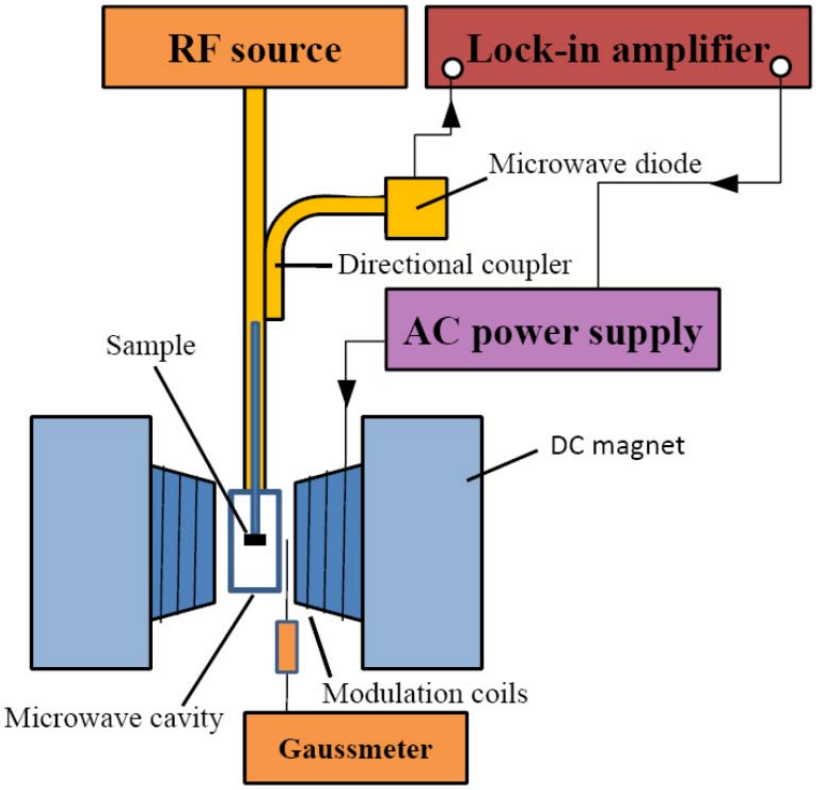

Fig. 3.4 Schematic of the conventional cavity-based FMR. The FMR measures absorption of microwave by magnetic materials under scanning magnetic field. The strong absorption peak is observed when the magnetization precession frequency matches with the applied microwave frequency.

In our experiments, we applied the FMR technique to study spin wave modes, magnetic interlayer coupling and magnetic damping in the FeCoB/Cr/FeCoB multilayer thin films. FMR is an effect based on exciting the uniform magnetization precession in the microwave frequency range in a resonant way, where the absorption of external microwave energy maintains steady precessional amplitude of the magnetization vector. FMR technique was developed in 1940s by Griffiths [94] and Kittel [95]. A static external bias field, H_B, is applied to define the initial direction of the magnetization. The magnetization equilibrium state is then changed by applying a weak, radio-frequency (RF) alternating magnetic field H_{rf}

(t) = $H_{rf} \cdot e^{i\omega t}$ perpendicular to the direction of H_B, where $|H_{rf}| \ll |H_B|$. The magnetization precesses in the effective magnetic field and the resonant absorption takes place when the microwave frequency ω equals the magnetization precession frequency ω_p.

Ordinary cavity-based FMR spectrometer is a device measuring the absorbed RF power by a magnetic sample in a microwave cavity. Fig. 3.4 shows the diagram of the cavity-based FMR setup. For 9.7 GHz cavity operation, a *RF* power is coupled into the cavity through a small hole in the upper end wall of the cavity, which is located about halfway between the cavity axis and the cavity wall. Microwave is absorbed by the sample and the cavity wall. The reflected *RF* power is directed by a 10 dB microwave directional coupler to a negative-type diode crystal detector for FMR signal detection. The external DC applied field is supplied by a pair of electromagnets, where the field strength is measured by a Gauss probe. In order to emphasize the small variations of the diode voltage due to the sample absorption, the applied field is modulated at a frequency of 100 kHz by a pair of Helmholtz coils attached to the pole pieces of the electromagnets. A lock-in amplifier is used to detect and amplify the corresponding AC component of the diode voltage.

In our experiments, a Bruker EMX 200U EPR was used to measure the FMR spectrum, which equipped with an ER4102ST universal X-band resonator, rectangular TE102 cavity. The operating frequency is at 9.74 GHz. A digital Hall field controller was incorporated to sweep the magnetic field with a resolution of 1 mG (0.1 μT). The field was produced by a water-cooled magnet with a pole diameter of 10 inches, 64 mm air gap and a 2.7 kW power supply. In the cavity-based FMR setup, a ferromagnetic sample was located in a strong magnetic field. The applied magnetic field and the magnetic anisotropy field in the sample were combined as an effective field which determines the Eigenfrequencies of magnetization precessions. If the magnetization precession frequency matches with the applied *RF* frequency, the microwave will be strongly absorbed which leads to an absorption peak in the spectrum. By varying the sample orientation in the resonant cavity which provides in-plane angular dependent FMR spectrum, the magnetic anisotropy constants of the sample can be extracted.

3.3 Time-resolved pump-probe optical spectroscopy

Besides microwave FMR technique, we have also used time-resolved pump- probe optical spectroscopy to investigate magnetic anisotropies, ultrafast magnetization excitation and quasiparticle relaxations in the magnetic single layer structure and the iron-based superconductors.

3.3.1 Femtosecond laser systems

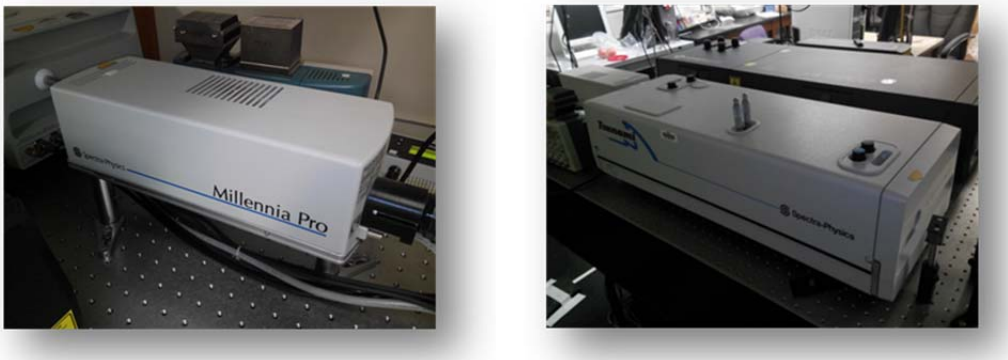

Fig. 3.5 532 nm CW-Nd: vanadate Laser (Millennia Pro, Spectra Physics, left) and *Ti:sapphire* ooscillator system (Tsunami, Spectra Physcis, right). The broad band tunable *Ti:sapphire* oscillator is pumped by the 532 nm CW-Nd: vanadate laser . The system delivers 100 fs, 800 nm laser pulses with a repetition rate 82 MHz.

The femtosecond pulsed laser system in our experiments is incorporated by the Diode-Pumped Frequency-Doubled CW-Nd:vanadate Laser (Millennia Pro, Spectra-Physics) and a Broadband Tunable Ti:sapphire Oscillator (Tsunami, Spectra-Physics). The Ti: Sapphire oscillator, based on Kerr mode locking, produces 100 *fs* pulses with the wavelength centered at 800 nm. The repetition rate of the laser pulse is 82MHz. The energy per pulse is around 1nJ.

3.3.2 Mode-locked Ti: sapphire oscillator

The schematic diagram of the mode-locked Ti:sapphire oscillator is shown in Fig. 3.6 [96]. The focusing mirror $\mathbf{P_2}$ directs the continuous wave from CW-Nd:vanadate Laser through the cavity focus mirror $\mathbf{M_3}$ and focuses the pump beam into the Ti:sapphire rod. The output beam is then collimated and expanded to normal size. The residual pump beam is dumped through the second cavity focus mirror as shown in Fig. 3.6. $\mathbf{M_4}$ and $\mathbf{M_5}$ which are cavity mirrors fold the beam and allow for a compact laser. $\mathbf{M_4}$ directs the cavity beam to $\mathbf{M_5}$, and then $\mathbf{M_5}$ directs it to $\mathbf{Pr_1}$. $\mathbf{Pr_1}$ and $\mathbf{Pr_4}$ prisms together with $\mathbf{Pr_2}$ and $\mathbf{Pr_3}$ are adjustable prism pairs for overall cavity dispersion balance and shortest output pulses. $\mathbf{M_6}$ through $\mathbf{M_9}$ prism mirrors direct the cavity beam from $\mathbf{M_5}$ through the prisms and into the acoustic optical modulator **(AOM)** which is driven by the electronics module to insure proper pulsing at start-up. $\mathbf{M_{10}}$ is output coupler **(OC),** one of two cavity end mirrors. Whereas the high reflector redirects all light back into the cavity, the output coupler allows a small percentage to pass through as the output beam.

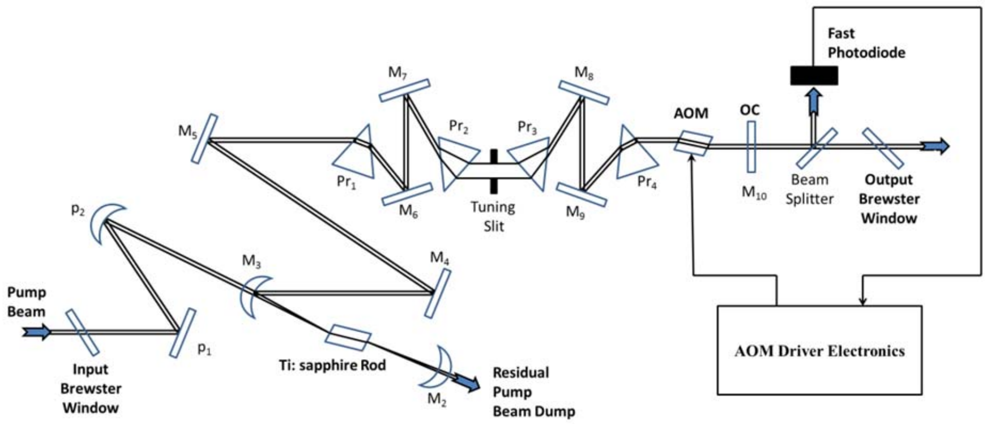

Fig. 3.6 Schematic of the optics and beam path in the Tsunami oscillator.

The alignment of the laser beam is crucial to the pulsed laser generation from the oscillator. By understanding the function of all the components in the oscillator, we optimize the output beam quality from the oscillator in our experiments. In detail, first we tune the dispersion prisms until the bandwidth is increased to the maximum. Then we adjust the mirror system form M_1 to M_{10} to optimize the output power.

The principle to generate the 100-fs laser pulses is based on the so-called mode locking. To understand the mode locking, it is necessary to discuss the conventional continuous wave (CW). In a laser cavity, the oscillating wavelengths must satisfy a standing wave condition. Some frequencies that satisfy this condition are the longitudinal modes of the laser. The longitudinal modes operate independently. Cavity perturbations cause some modes to stop oscillating and restart oscillating with different phases. Therefore, the laser output contains various randomly phased modes. The electrical field which contains N in-phase modes with equal intensity is expressed as:

$$E = \sum_{i=1}^{N} e^{i(\omega_0 + n\Delta\omega)t} = e^{i(\omega_0 + \Delta\omega)t} \frac{1 - e^{iN\Delta\omega t}}{1 - e^{i\Delta\omega t}}. \tag{3.1}$$

where the $\Delta\omega = 2\pi c/2L$, L is the optical length of the laser cavity. The intensity of the combined laser mode is written as:

$$I = E \cdot E^{*} = \left(\frac{\sin \frac{N\Delta\omega t}{2}}{\sin \frac{\Delta\omega t}{2}} \right)^{2} . \tag{3.2}$$

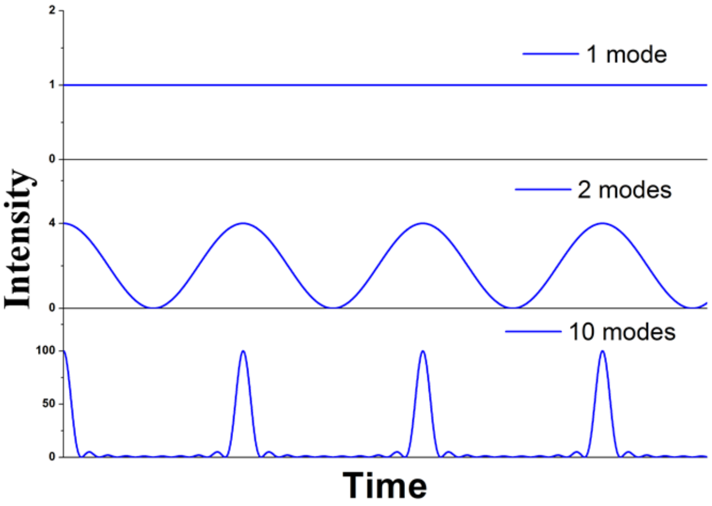

Fig. 3.7 Example of mode locking principle. The laser pulse train is generated by accumulating as many as laser modes with same phase in the cavity. The more in-phase modes are accumulated, the shorter pulse width and higher pulse intensity can be achieved.

Fig. 3.7 shows the simple simulation base on Eq. 3.2. As the in-phase modes adding up, the laser starts pulsing. The intensity of the pulse is proportional to N^2 while the pulse width is proportional to $2\pi/N\Delta\omega$. In a mode locking laser, active mode locking is a common approach used to obtain short optical pulses from solid state or gas lasers. A loss modulation is applied to the laser cavity at the same frequency as the pulse reprate. It is similar to put an optical shutter into the laser cavity: only light that arrives at the shutter at precisely the correct time passes through and is amplified in the gain media. Thus, the longitudinal modes with same phase will accumulate to generate the pulsed laser.

Based on the principle of generating the ultra-short laser pulses, we realized that the adjustment of laser bandwidth are critical to the power and the pulse width of the output ultrafast laser pulses, which is the reason to characterize both the pulse width and the laser bandwidth.

3.3.3 Autocorrelations of laser pulses

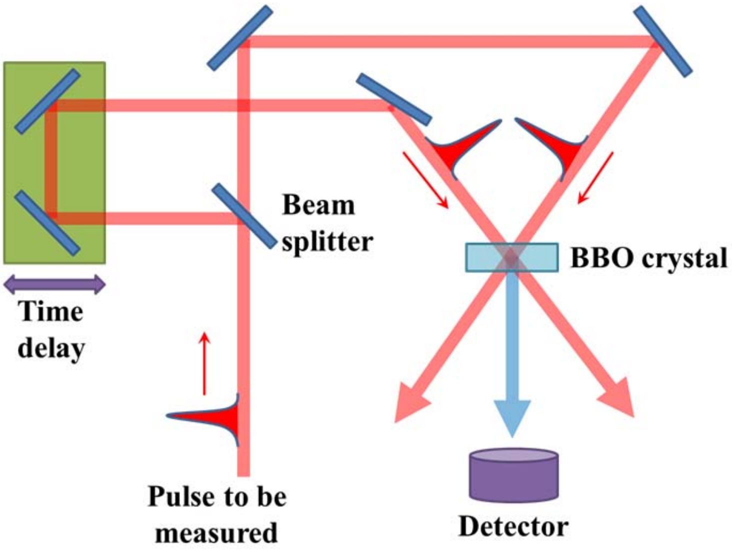

Fig. 3.8 Intensity autocorrelation by second-harmonic generation. The delay stage controls the time delay between two isogenous pulses. The second harmonic generation signal can be detected when the two isogenous pulse reach the second harmonic crystal at the same time.

We characterized the pulse width of the generated laser pulses by the intensity autocorrelation method. The principle of the autocorrelation is to use pulses to measure its pulse spectrum. In our setup (Fig. 3.8), we split an 800 nm laser beam into two by a beam splitter. One of them is input to the retro-reflector on the delay stage for inducing a time delay between two split pulses. We redirected the two split beams by the mirrors to overlap them on a BBO crystal (special cut: $\theta = 28°$, $\varphi = 0°$). We detected a strong 400 nm SHG signal as shown in Fig. 3.8 when two split 800 nm laser pulses overlap in time and space on the crystal.

In SHG process, the BBO crystal absorbs two photons and generates a new photon with the frequency twice as the absorbed one. The generated SHG electric field is written as:

$$
\begin{aligned}
E(2\omega) &\propto |E|\exp(ik_1\cdot r+\omega t)\cdot|E|\exp(ik_2\cdot r+\omega t)\\
&=|E|^2\exp\left[i(k_1+k_2)\cdot r+2\omega t\right]
\end{aligned}
\qquad (3.1)
$$

We see the SHG signal arises in between two 800 beams as shown in Fig. 3.8.

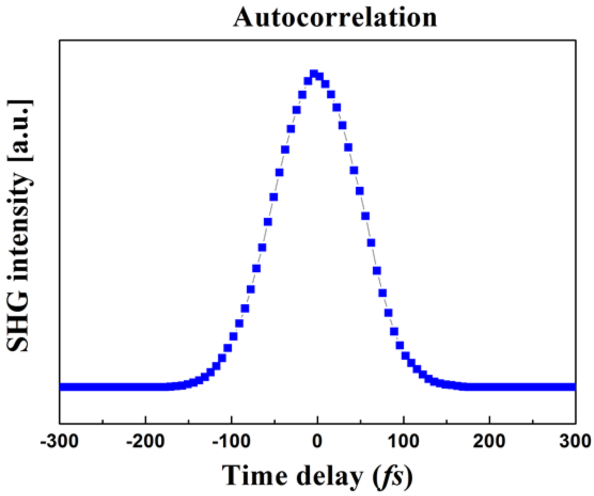

Fig. 3.9 Intensity autocorrelation obtained in our experiment by measuring the second harmonic generation signal as a function of time delay between the two isogenous laser pulses. The pulse width is around 100 femtoseconds.

In addition, the intensity profile of the autocorrelation takes the form:

$$A_c(\tau)=\int_{-\infty}^{+\infty} I(t)I(t-\tau)dt \qquad (3.2)$$

where the τ stands for the time delay between two pulses which is controlled by the delay stage as shown in Fig 3.8. The intensity autocorrelation result in our experiments is shown in Fig. 3.9. The pulse width is around 100 *fs*.

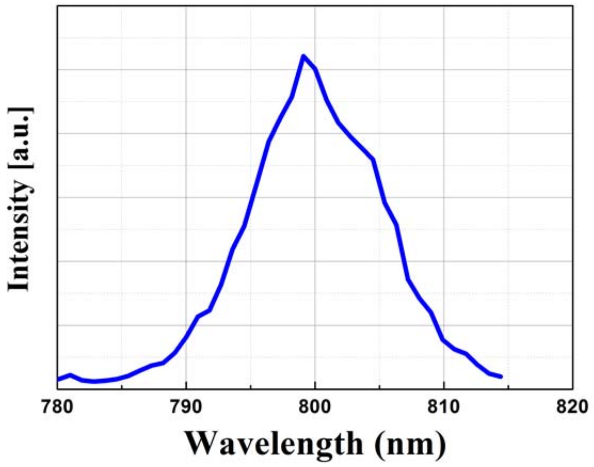

Fig. 3.10 Spectrum distribution of the pulsed laser from an optical spectrum analyzer (Newport OSM-100-VIS/NIR). In our experiments, we tune the wavelength of both the pump an the probe beam to 800 nm and the bandwidth of laser beams were identified to be 15 nm.

In our experiments, we measured the wavelength and bandwidth of the laser pulses by using a NEWPORT OSM-100-VIS/NIR optical spectrum analyzer (OSA) with a resolution of 0.1 nm and a sensitivity of ~100 pW over the range 0.6 – 1.6 μm. We used an optical fiber cable to couple the laser signal into the spectrometer. The spectrum analyzer displays a power spectrum over preset frequency scan range and monitors the change of the laser spectrum in real time. The measured results are shown in Fig. 3.10 in which the wave length is centered at 800 nm while the bandwidth is around 15 nm.

3.3.4 Time-resolved pump-probe optical spectroscopy setups

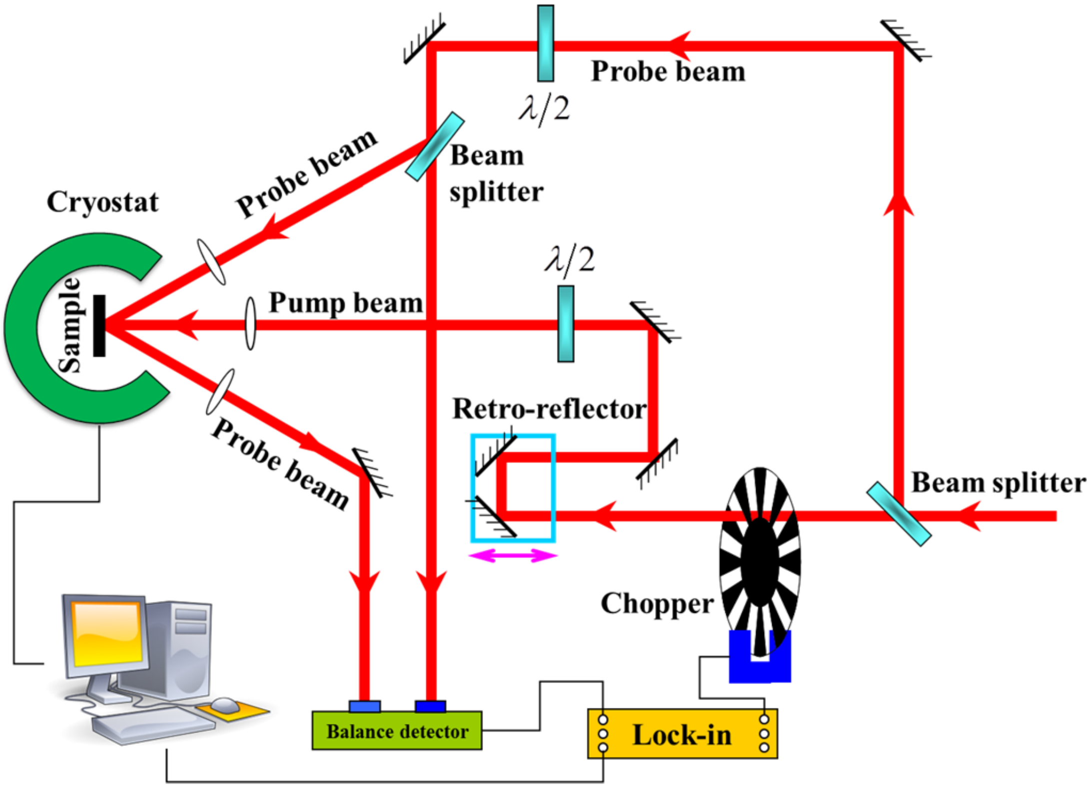

Fig. 3.11 Schematic diagram for the time-resolved pump-probe optical spectroscopy setups. The reflectivity change of the probe beam is measured as a function of time delay between pump pulse and probe pulse.

In our studies, we employed the time-resolved pump-probe optical spectroscopy to study the quasiparticle relaxations in the iron based superconductor. The whole setup is basically measuring the transient change of the optical reflectivity of the probe beam reflected from the sample surface. As shown in Fig. 3.11, the time-resolved pump-probe optical reflectivity measurements are performed with the laser operating at 800 nm. A beam splitter splits the 800 nm pulsed laser from Ti: sapphire oscillator into a stronger pump beam and a weaker probe beam. A mechanical chopper is applied to mark the pump beam with a frequency at 2 KHz in order to make lock-in amplifier recognize the signal in the reflected probe beam generated by the pump beam in the sample. The Retro-reflector provides the variable time delay between the pump and probe pulses. Two lenses (focus length: 25cm) are utilized to collimate the pump and probe pulses into an overlapping region of the sample with spot diameter ~ 0.5 mm. The sample is mounted in a cryostat for temperature dependent measurements (down to 7 K). The typical pump beam power for our experiments is less than 20 mW, and the probe beam power is less than 4 mW.

For the detection, the probe beam reflected from the sample is sent into the ‘signal’ channel of the balance detector. In the meanwhile, another reference probe beam separated by the second beam splitter as shown in Fig. 3.11 is input in the ‘reference’ channel of the balance detector. The output of balance detector is intensity difference between two channels: $I_{signal} - I_{reference}$.

3.3.5 Time-resolved pump-probe MOKE spectroscopy

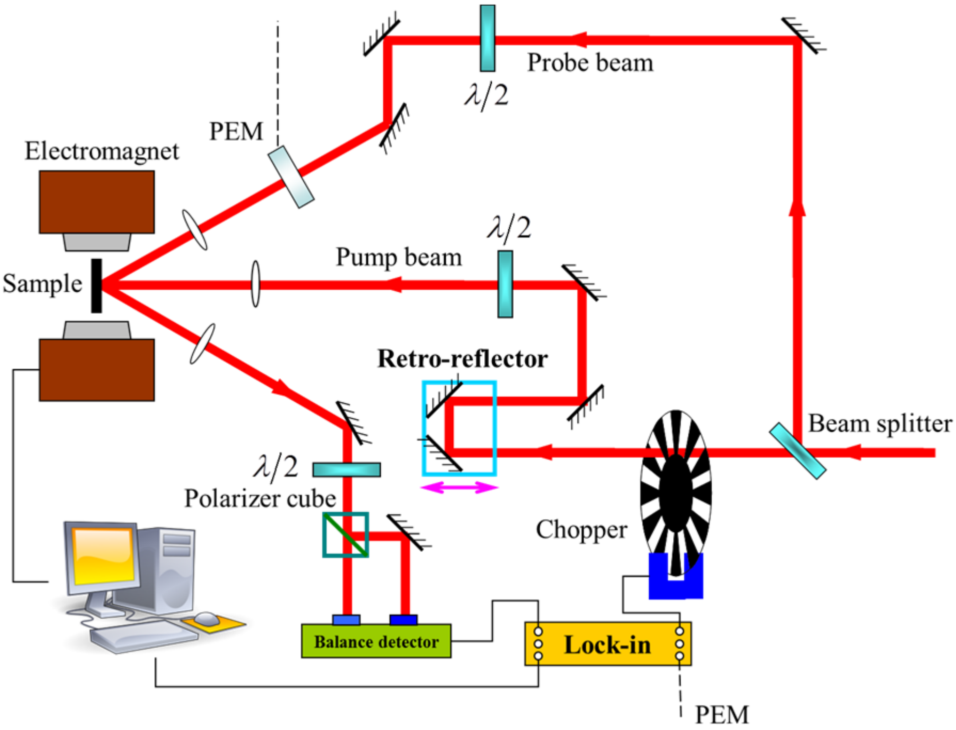

Fig. 3.12 Schematic diagram for the time-resolved pump-probe MOKE spectroscopy setups. The polarization change of the probe beam is measured as a function of time delay between pump pulse and probe pulse.

In our studies, we employed the time-resolved pump-probe MOKE spectroscopy to study the transient spin dynamics in the iron thin film. The whole setup of time-resolved pump-probe MOKE spectroscopy is basically measuring the transient polarization change of the probe beam reflected from the sample surface. The experimental layout of the time-resolved pump-probe MOKE spectroscopy setup in our lab is shown in Fig. 3.11. It differs from the time-resolved pump-probe optical spectroscopy setup in that the sample is mounted in between two poles of the electromagnet for magnetic field dependent measurements. The electromagnet is controlled by the computer and provides a variable magnetic field up to 0.5 Tesla. The balance detector determines the intensity difference between s- and p-polarization components of the reflected probe beam. By this means, we are able to monitor the transient polarization change of the probe beam induced by the pump beam in the iron thin film.

Chapter 4 Magnetization dynamics in magnetic single layer and trilayer structures

Magnetic thin films have been actively explored for applications in microwave, spintronics and high-density magnetic recording devices [2, 4, 97]. It is extremely important to understand and control the magnetic dynamical properties of magnetic thin films that directly affect their performance in technological applications. In this chapter, the magnetization dynamics in both single layer iron thin films and trilayer FeCoB/Cr/FeCoB structures were investigated based on results from the time-resolved MOKE spectroscopy and FMR techniques. In section 4.1, the magnetic anisotropies and control of magnetic damping are studied in the single layer iron thin films. In section 4.2, the control of magnetic dynamical properties by magnetic interlayer coupling in the trilayer FeCoB/Cr/FeCoB structures is discussed according to the theory described in Chapter 2.

4.1 Magnetization dynamics in iron thin film

4.1.1 Brief theoretical description

After femtosecond laser pulse excitation, the magnetization of the film exhibits precessional motion and then relaxes back toward equilibrium orientation. This precession is described by the Eq. (2.11) in chapter 2, where the effective, *H_{eff}*, is derived by differentiating the magnetic free energy [98]:

$$E = -H_0 \cdot M + 2\pi M_z^2 + \frac{K_a M_z^2}{M_s^2} - \frac{K_{\parallel}(M_y^4 + M_y^4)}{2M_s^4} - \frac{K_{\perp} M_z^4}{2M_s^4} - \frac{K_u \left[M_x M_y + 1/2(M_x^2 + M_y^2) \right]}{M_s^2}.$$

(4.1)

where K_a is the uniaxial easy-plane anisotropy constant, $K_{//}$ is the in-plane uniaxial anisotropy constant, $K\perp$ is the perpendicular anisotropy constant, and K_u is the in-plane biaxial anisotropy constant. The first term in Eq. (4.1) represents the Zeeman energy while the others denote the anisotropy energies. The formula shows that the precession dynamics are heavily dependent of the magnetic anisotropies and also rely on the applied magnetic field.

To understand the response of the magnetization precession under different magnetic fields, the Landau-Lifshitz-Gilbert equation [99] is employed as described in Chapter 2: H_{eff} exerts a torque on a magnetic moment and the magnetic moment is driven into precessional motion around the direction of the effective field. The precession is damped by exchanging energy and angular momentum with the environment until the magnetization aligns parallel to H_{eff}. We derive the dispersion relation of the magnetization Eigenfrequencies as:

$$\omega^2 = \gamma^2 \left[H_0 \cos(\delta - \varphi) + 4\pi M_{eff} + \frac{H_u}{2}(1 + \sin 2\varphi) + H_{//}(\sin^4 \varphi + \cos^4 \varphi) \right] \cdot \\ \left[H_0 \cos(\delta - \varphi) + H_u \sin 2\varphi + H_{//} \cos(4\varphi) \right] \tag{4.2}$$

where δ and φ represent the angles of the in-plane applied magnetic field and equilibrium magnetization compared to the in-plane easy axis, $4\pi M_{eff}$ is the effective demagnetization field, and H_u and $H_{//}$ are the in-plane uniaxial and cubic anisotropic fields. When the applied magnetic field is not aligned with the magnetization vector, the equilibrium magnetization vector angle, φ, has to be calculated by minimizing the free energy of the magnetization system[98]:

$$E = -H_0 M_s \cdot \cos(\delta - \varphi) \\ + H_{//} M_s \left[\cos^4 \varphi + \sin^4 \varphi \right] / 4 - H_u M_s \left[\cos\varphi \sin\varphi + 1/2\left(\cos^2 \varphi + \sin^2 \varphi \right) \right] / 2. \tag{4.3}$$

The equilibrium position of magnetization is always in-plane and given by [98]:

$$H_0 \sin(\delta - \varphi) - \frac{H_{//}}{4} \sin 4\varphi + \frac{H_u}{2} \cos 2\varphi = 0. \tag{4.4}$$

In our studies, the time-resolved pump-probe MOKE approach was applied to study the spin dynamics in the single layer iron thin film. By using the Eq. (4.1)-(4.4), we successfully describe distinct behaviors of the spin wave frequency under different magnetization orientations and obtained the magnetic dynamical parameters in the single layer iron thin film.

4.1.2 Magnetization precession spectrum with applied field along [100] axis

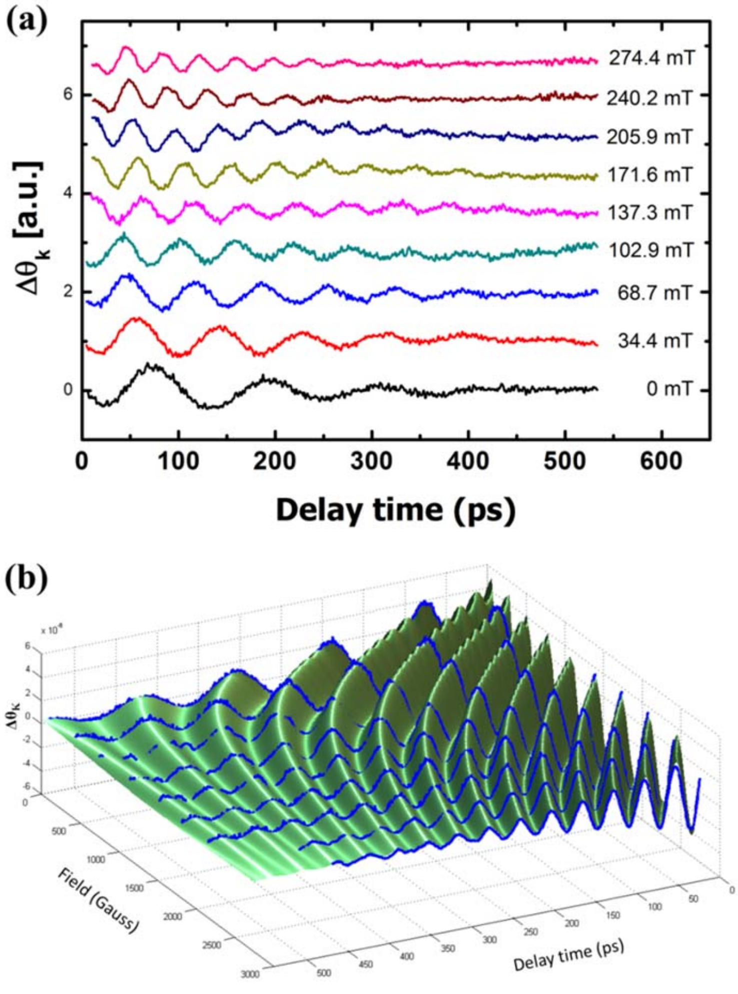

Fig. 4.1 (a) Time-resolved pump-probe MOKE spectra for the Fe/GaAs thin film measured with a magnetic field applied along [100] easy axis. (b) Precessional time-resolved pump-probe MOKE data for various applied fields (solid lines) and simulated time-resolved pump-probe MOKE (surface) according to the Eq. (4.2).

First, we performed time-resolved pump-probe MOKE measurements with the magnetic field applied along [100] crystal axis (easy axis). Fig. 4.1 (a) shows the time-resolved pump-probe MOKE spectra with an applied magnetic field in the sub-nanosecond time scale. The observed oscillations are assigned to the precession of the magnetization around its equilibrium position. We observed that the oscillation frequency increases monotonically as the magnetic field is enhanced. Fig. 4.1 (b) exhibits the 3-D simulation (surface) of the magnetic field dependent time-resolved pump-probe MOKE spectra. Under the laser excitation, the change of magnetic anisotropy induced by the laser pulse alters the total effective field. The magnetization starts to align with the altered effective magnetic field. After the laser pulse, the total effective field recovers to the original value and direction within hundreds femtoseconds. However, the magnetization followed the effective field is still out of equilibrium and starts to relax by precessing around the effective field. The effective field, including the applied magnetic field and all effective anisotropic fields, determines the frequency of the magnetization precession. To investigate the effective anisotropic fields, the time-resolved pump-probe MOKE spectra are recorded under various in-plane magnetic fields.

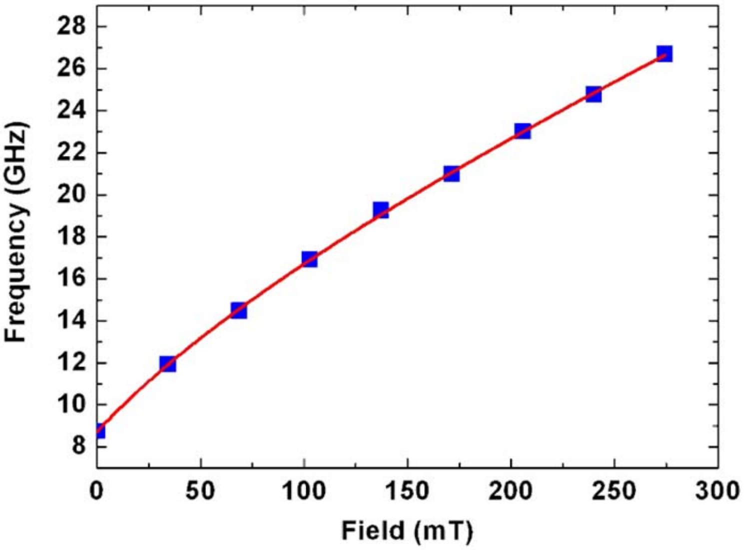

Fig. 4.2 Measured magnetic-field dependence of the precession frequencies and fit. The precession frequency increases monotonically as a function of the applied magnetic field. The results are fit by Eq. (4.2).

Fig. 4.2 shows magnetization precession frequencies as a function of an applied magnetic field. The solid line shows the fit by Eq. (4.2). We obtain the g-factor as of ~ 2.1, the effective in-plane uniaxial anisotropy field H_u as of around 0.003 T, the effective in-plane cubic anisotropy field $H_{//}$ as of ~ 0.04 T, and the effective demagnetization, $4\pi M_{eff,}$ as of ~ 2.1 T.

4.1.3 Magnetization precession spectra with applied field along [1-10] axis

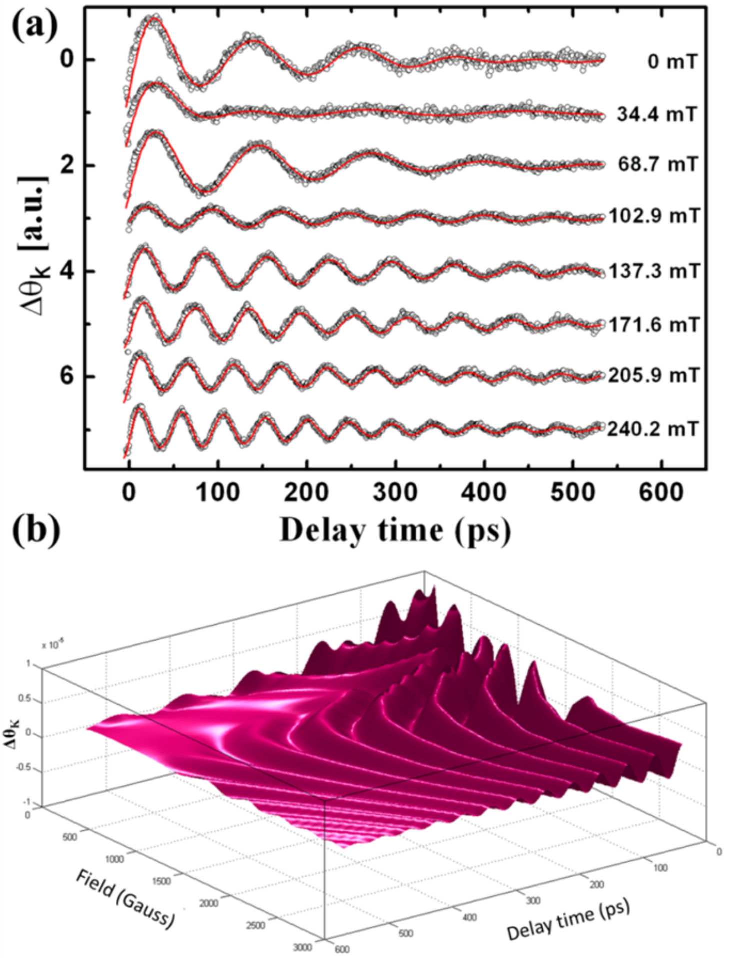

Fig. 4.3 (a) Time-resolved pump-probe MOKE spectra for the Fe/GaAs thin film measured as magnetic field applied along [1-10] hard axis direction and their fit. (b) 3-D simulation (surface) of time-resolved pump-probe MOKE spectra as a function of magnetic field calculated according to Eq. (4.2).

Next, we performed time-resolved pump-probe MOKE measurements with the magnetic field applied along [1-10] crystal axis (hard axis). Fig. 4.3 (a) shows magnetic field dependent time-resolved pump-probe MOKE spectra under the magnetic field along [1-10] crystal axis. Clear oscillations are observed in the spectra. However, compared to the case when the magnetic field is applied in [100] crystal axis, the oscillation frequency does not increase monotonically as a function of magnetic field. The 3-D Simulation of the time-resolved pump-probe MOKE spectra is plot in Fig. 4.3 (b) which gives a continuous evolution of the spectra as a function of field.

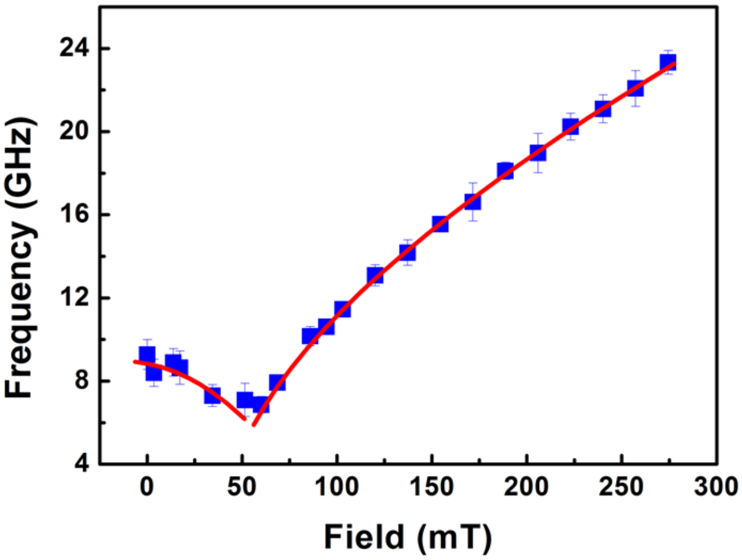

Fig. 4.4 Measured precession frequencies as a function of applied magnetic field. The solid line shows the fit based on Eq. (4.2) by considering the magnetic field dependent equilibrium magnetization angle.

Fig. 4.4 shows the precession frequency as a function of the applied magnetic field. Apparently, the behavior of the field dependent precession frequency is quite different when the magnetic field is applied along the [100] easy axis. To understand this phenomenon, the relative angle of the equilibrium magnetization, φ, has to be considered in Eq. (4.2).

In the case the magnetic field is applied along [100] easy axis, both the magnetic field angle, δ, and magnetization angle, φ, equal to zero. In Eq. 4.2, the precession frequency increases monotonically when the magnetic field is enhanced as shown in Fig 4.2. In the case the magnetic field is applied along the [1-10] hard axis, the equilibrium magnetization vector which initially aligns with [100] axis starts to rotate towards [1-10] axis as the magnetic field is increasing.

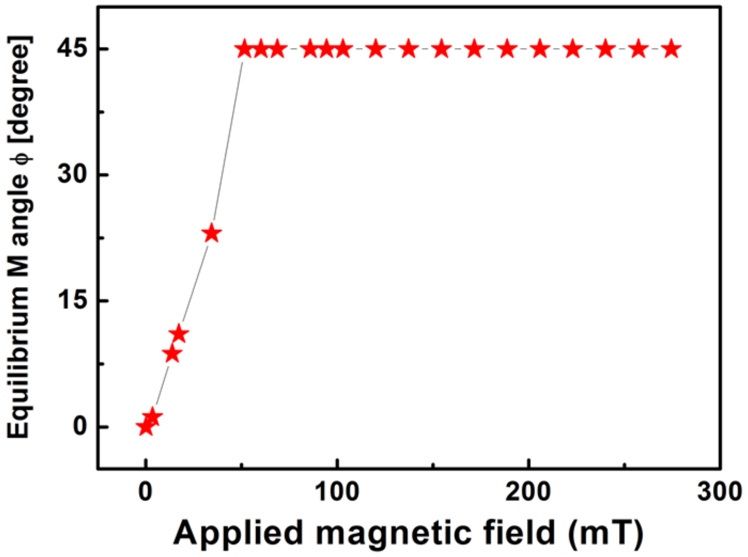

Fig. 4.5 Calculated φ as a function of applied magnetic field. In the case applied magnetic field is applied 45 degree compared to the magnetization vector, the magnetization vector rotates towards the magnetic field orientation as the magnetic field is increasing.

Fig. 4.5 shows the calculated equilibrium magnetization vector angle, φ, as a function of applied magnetic field from Eq. (4.4). By considering the equilibrium magnetization vector angle variation as a function of applied magnetic field in Eq. (4.2), the behavior of the magnetic field dependent precession frequency is described and fit in Fig. 4.4 (solid red line).

4.1.4 Magnetization precession spectra under various applied field orientation

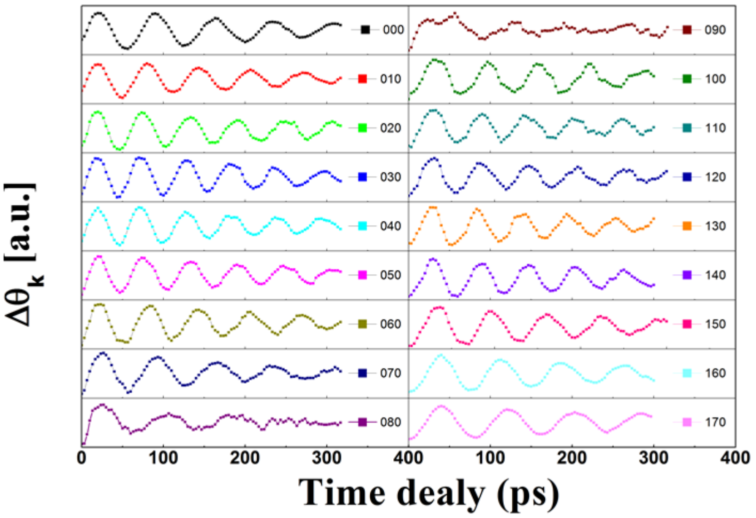

Fig. 4.6 Time-resolved pump-probe MOKE spectra for the Fe/GaAs thin film measured

under various in-plane magnetic field angles (from 0 to 170 degree). The signal evolves periodically as a function of the applied magnetic field orientation.

Further, we performed the time-resolved MOKE measurements by varying the magnetic field orientation to map out the magnetic anisotropy distribution in the sample plane. The applied magnetic field strength was kept at 0.14 T.

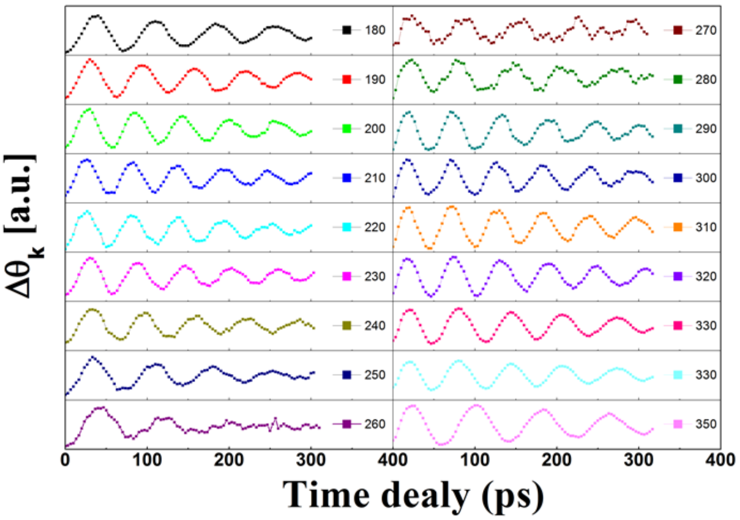

Fig. 4.7 Time-resolved pump-probe MOKE spectra for the Fe/GaAs thin film measured under various in-plane magnetic field angles (from 180 to 350 degree).

Fig. 4.6 and Fig. 4.7 show the time-resolved pump-probe MOKE spectra measured at various in-plane magnetic field orientations relative to the [100] easy axis. The field orientation dependent magnetization precession frequency is plotted in Fig. 4.8.

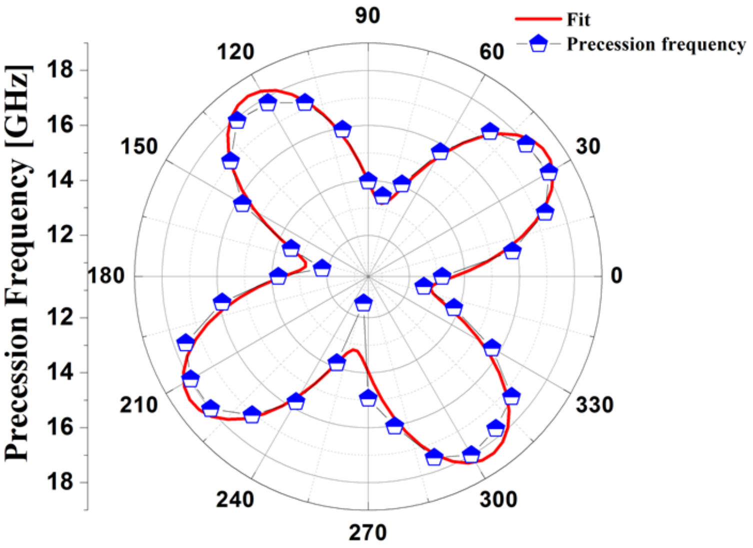

Fig. 4.8 Magnetization precession frequency as a function of in-plane magnetic field orientation, the red solid line is the fit. The four-fold distribution of the magnetization frequency indicates that the in-plane cubic anisotropy is dominative. The results are fit by Eq. (4.2).

The magnetization precession clearly shows four fold rotational symmetry in frequency. The result indicates that the in-plane cubic anisotropic field $H_{//}$ dominates the total magnetic anisotropy in the sample plane. By using Eq. (4.2) and considering the angle of magnetization under various magnetic field orientations, the field orientation dependent precession frequency result is fit and plot with red solid line in Fig. 4.8. The fitting gives the in-plane uniaxial anisotropic field H_u = 0.0029 T, the in-plane cubic anisotropic field $H_{//}$ = 0.0473 T and $4\pi M_{eff}$ = 2.0656 T. The 10 nm epitaxially grown iron thin film is bcc structure, the magnetic crystalline anisotropy is biaxial symmetric for bcc crystal structure. Therefore, we conclude that the in-plane cubic anisotropy arises from the magnetic crystalline anisotropy in the iron thin film. Moreover, the magnetic crystalline anisotropy is dominative in the sample plane. The in-plane uniaxial anisotropy component may results from the magnetic shape anisotropy.

In addition, the damping constant α is calculated based on the time-resolved pump-probe MOKE spectra as a function of in-plane magnetic field orientation.

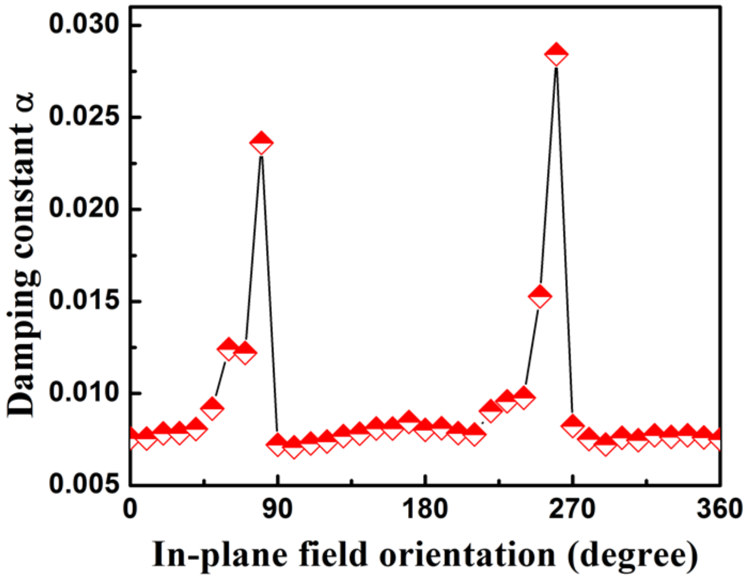

Fig. 4.9 Damping constant *α* as a function of in-plane magnetic field orientation. The distribution of the damping constant shows uniaxial dependence on the applied magnetic field orientation. The result is attributed to the uniaxial anisotropy in the sample plane.

Figure 4.9 shows the calculated damping constant α as a function of in-plane magnetic field orientation [100]. The angular distribution of damping constant α exhibits two sharp peaks as the in-plane field is applied close to 90 and 270 degrees, which is attributed to the in-plane uniaxial anisotropy. The results show the feasibility to tune the damping constant *α* by in-plane magnetic field orientation in the soft magnetic thin film.

In summary, coherent magnetization precessions were generated in iron thin film. By considering the magnetic field dependent equilibrium magnetization rotation, we successfully demonstrated the magnetization precession frequency spectra under various magnetic field strengths and orientations in iron thin film. Our results unveil that the in-plane cubic anisotropy comes from the magnetic crystalline anisotropy of the bcc iron thin film. The in-plane cubic anisotropy is dominated compared to the in-plane uniaxial anisotropy. In addition, the damping constant *α* shows as a uniaxial dependence on the in-plane magnetic field orientation which is attributed to the in-plane uniaxial magnetic anisotropy.

4.2 Magnetization dynamics in FeCoB/Cr/FeCoB trilayer Structures

Compared with the single layer structures, the magnetic multilayer structures attract some attentions most recently because of their interesting interlayer interactions. The interlayer interactions between FM layers and FM/AFM (anti-ferromagnetic) layers can be utilized to control the magnetic properties in multilayer structures. In our study, FMR technique is employed to study magnetic dynamical properties induced by the interlayer coupling between FM layers in the magnetic FeCoB/Cr/FeCoB trilayer structures.

4.2.1 Acoustic and Optical spin wave modes

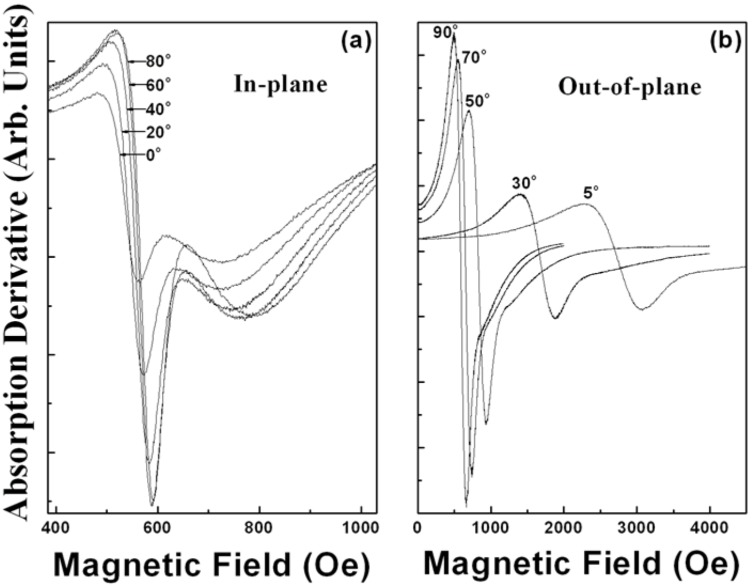

Fig. 4.10 FMR resonance spectra as a function of magnetic field orientations in the sample with the 20-Å *Cr* layers measured under (a) in-plane configuration, (b) out-of-plane configuration.

Fig. 4.10 a) and b) show the FMR spectra of the sample with the 20-Å *Cr* layers under the in-plane and out-of-plane configuration. For the in-plane geometry, the resonant field increases when the applied magnetic field rotates away from the easy axis ($\varphi = 0°$). This corresponds to the uniaxial anisotropic field induced by the magnetic field annealing. In contrast, for the out-of-plane configuration, we observe the shift of the resonance to higher fields as the direction of the magnetic field approaches normal to the sample surface and a significant broadening of FMR linewidth (as a result, its amplitude decreases). The line shift is induced by the demagnetizing field. For a thin film sample, a macroscopic magnetization could produce a field of *4πM*, which usually points along the perpendicular direction of the sample plane. When the sample is rotated with respect to the applied magnetic field, the equilibrium angle of the magnetization vector depends strongly on the external field value. Therefore, a shift of FMR field and an increase in linewidth at an intermediate angle is expected. Moreover, for both configurations, the FMR lines show strong asymmetric behaviors with respect to the base line. The asymmetric behavior of the absorption curve is due to the interlayer coupling of the FM layers. The feature is attributed to the overlap of the in-phase precession and out-of-phase precession resonant modes of the neighboring FM magnetizations, which refers to the acoustic and optical spin wave resonance modes, respectively.

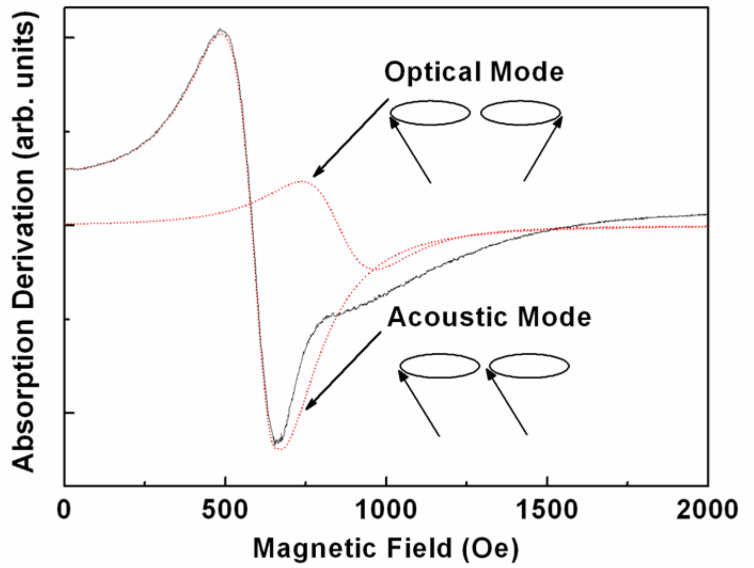

Fig. 4.11 FMR spectrum in the sample with the 20-Å *Cr* layers. The red dashed lines show the deconvolution of the spectrum indicating an acoustic mode and an optical mode. The inset of the figure shows the schematic of these two modes. The in-phase precession refers to the acoustic spin wave resonance; the out-of-phase precession is attributed to the optical spin wave resonance.

Fig. 4.11 shows such a typical FMR spectrum: the broad feature at high magnetic field side of the acoustic spin wave resonance mode can be deconvoluted to yield a weak absorption line that is attributed to an optical mode. The acoustic mode and the optical mode exist together in the spectrum for the multilayer system [8, 101], as they are close enough, the FMR lines will partially overlap and form asymmetric absorption peaks. The optical mode disturbs the main resonance line and introduces an additional contribution of the FMR linewidth and an asymmetric line shape. The acoustic and optical spin wave modes describe the interlayer coupled precession of magnetization vectors, as illustrated in the inset of Fig. 4.11. The nature of the interlayer interactions is studied by estimating the differences in resonance fields between acoustic and optical modes.

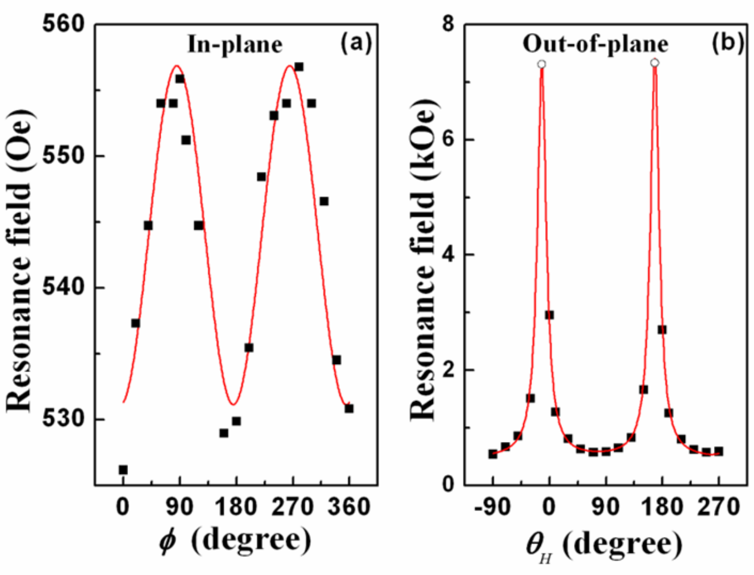

Fig. 4.12 Angular dependencies of resonance fields of the FMR spectrum in both (a) the in-plane and (b) the out-of-plane configurations for the sample with the 20 Å *Cr* layers. The solid lines show the fitting using Eq. (2.18) and (2.19) in chapter 2. The resonant field at $\theta_H \approx 0$ and 180° is a singularity and cannot be reached in our measurements. The two-fold result indicates the uniaxial anisotropic symmetry for the in-plane and the out of plane configurations as the applied field is rotated away from the easy axis.

Eq. (2.18) and (2.19) in chapter 2 is employed to fit the in-plane data and obtain the effective in-plane uniaxial magnetic anisotropy, $2K_{\parallel}/M$ as of ~ 20 Oe and the demagnetization field, $4\pi M\text{-}2K_{\perp}/M$ as of ~ 2.0 T, for the 20-Å *Cr* layer sample as shown in Fig. 4.12 (a). Next, we use the obtained parameters to describe our out-of-plane FMR data.

Fig. 4.12 (b) reveals the measured and calculated resonant fields in the out-of-plane configuration. It is realized that as the applied field moves away from the in-plane orientation, the magnetization does not change at an identical rate to the applied field.

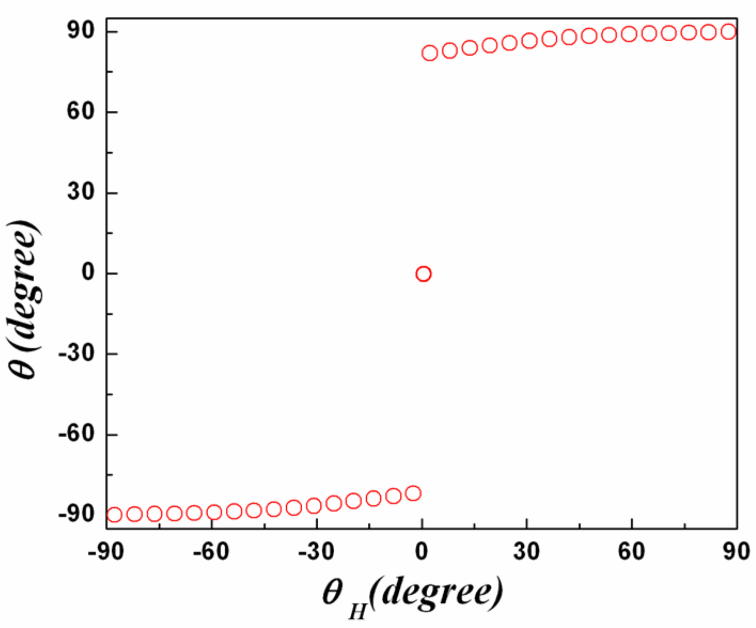

Fig. 4.13 Equilibrium angle of the magnetization, θ, as a function of the angle of the applied field θ_H in the out-of-plane configuration (φ = 0°). In the out-of-plane configuration, the magnetization can only be tilted to a small angle out of the sample plane by the applied magnetic field.

The equilibrium angle of magnetization is calculated by minimizing the free energy. The result is shown in Fig. 4.13. The magnetization, M, immediately begins to seek the easy orientation as the magnetic field is tilted away from the direction normal to the sample surface (the resonant field at $\theta_H = 0^o$ is a "singularity" and cannot be reached). In contrast to the out-of-plane configuration, the resonant magnetic fields are sufficiently high enough to turn the magnetization vector, M, parallel to the applied magnetic field, H, in the in-plane orientations.

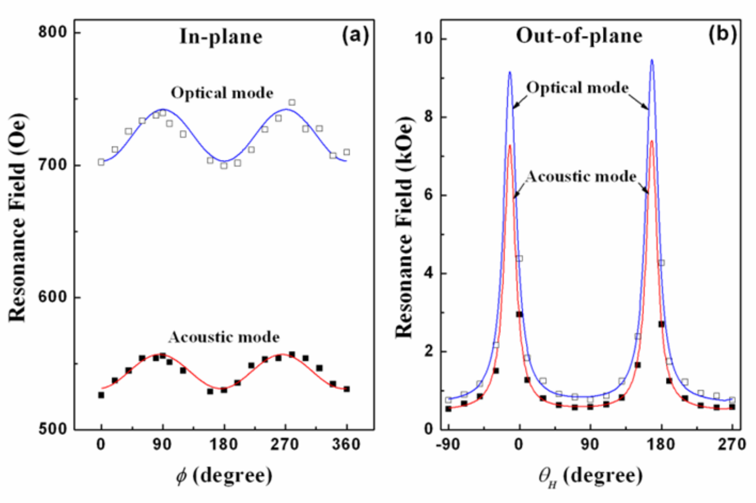

Fig. 4.14 Angular dependence of resonance fields of the acoustic mode and optical mode in both (a) the in-plane and (b) the out-of-plane configurations for the sample with 20 Å *Cr* layers. The solid lines of the optical mode represent the fitting results using Eq. (2.20) and (2.21) in chapter 2.

Fig. 4.14 shows the angular dependences of resonance fields including the acoustic mode and the optical mode in both (a) the in-plane and (b) the out-of-plane configurations for the sample with 20 Å *Cr* layers. Similar to the acoustic mode, the optical mode also shows the two-fold geometry due to the uniaxial anisotropy contribution. Furthermore, the difference in resonant fields of the acoustic mode and optical mode ($\Delta H = H^o - H^a$) shows different behaviors in the in-plane and the out-of-plane configurations.

In the FMR measurement, since $\omega^+ = \omega^-$, the relation between H_R^o and H_R^a can be calculated by combining Eq. (2.18), (2.19) (2.20) and (2.21) in chapter 2 which takes the form:

$$H^o = H^a + \frac{J_{eff}}{\cos(\theta_H - \theta)}, \qquad \text{(out-of-plane)}$$

$$H^o = H^a + J_{eff}. \qquad \text{(in-plane)}$$

(4.8)

The magnetic interlayer coupling is determined by the J_{inter}: the adjacent two FM layers in the sample are ferromagnetically coupled with a positive J_{inter}, but are antiferromagnetically coupled with a negative J_{inter} [95]. In turn, a positive J_{eff} represents the antiferromagnetic coupled FM layers, while a negative J_{eff} represents the ferromagnetic coupled layers (since the J_{eff} is defined as $-2J_{\mathrm{inter}}/dM$). From the data shown in Fig. 4.14, an interlayer coupling constant, J_{eff} as ~179.8 Oe is extracted by fitting the optical branch data using Eq. (2.20) and (2.21) in chapter 2.

Furthermore, in order to understand how the interlayer spacing affects the interactions between FM layers, the J_{eff} is calculated according to the FMR spectra in a series of *FeCoB/Cr/FeCoB* multilayers with different thicknesses of the *Cr* layers; the values are shown in Table 4.1. The adjacent two FM layers are found to be all antiferromagnetically coupled in our sample since the values for J_{eff} are all positive. This is consistent with our original assumption: $\varphi_2 = -\varphi_1$. Moreover, the interlayer coupling constant, J_{eff}, does not increase monotonically with the *Cr* layer thickness, but shows an oscillatory behavior. The result can be explained by the quantum interference between adjacent FM layers [102]. Due to the reflection of Bloch waves on interfaces of FM/AFM layers, multiple interferences could occur in *Cr* spaces and a phase shift is expected for the itinerant electron wave function. The phase shift varies with different interlayer *Cr* thicknesses and therefore changes the density of itinerant electron states. Since the density of the itinerant electron states determines the interlayer coupling strength, an oscillatory change of J_{eff} is observed with increasing the thickness of the spacing *Cr* layer.

Table 4.1 Interlayer coupling constant: Jeff and the effective in-plane uniaxial magnetic anisotropy: 2K∥/M for samples with different Cr layer thicknesses.

***Cr* layer thickness (Å)**	**J_{eff} (Oe)**	**$2K_{\parallel}/M$ (Oe)**
4	120.1±4.9	13.9±1.3
10	160.3±2.2	14.3±0.4
20	179.8±6.8	14.7±0.2
30	280.4±4.3	16.6±1.1
40	220.2±2.9	36.0±3.2

It is important to note that the magnetic parameters are also affected in response to the change of the interlayer coupling between neighboring FM layers. Table 4.1 shows the in-plane uniaxial magnetic anisotropy constant for samples with different *Cr* layer thicknesses from our FMR measurements. The in-plane uniaxial magnetic anisotropy increases monotonically as the *Cr* layer thickness is changed from 4 Å to 40 Å. This is attributed to the redistribution of the magnetic moments in the FM layers by the interlayer interactions. Moreover, the out-of-plane uniaxial anisotropy, $2K_{\perp}/M$ is directly related to the change of the interlayer coupling strength.

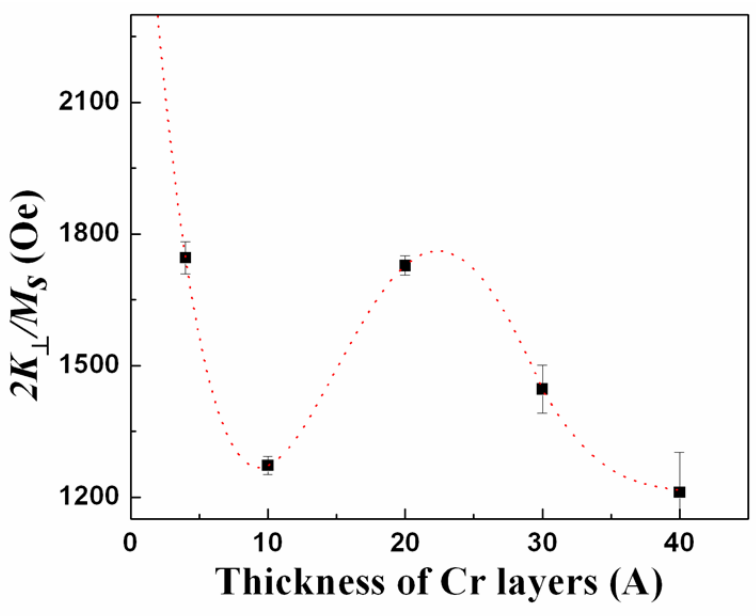

Fig. 4.15 *Cr* layer thickness dependent out-of-plane effective anisotropy *2K⊥/M*. The oscillatory behavior indicates the influence from the interlayer coupling. The dashed line is only meant to guide the eyes.

As shown in Fig. 4.15, an oscillatory change of the out-of-plane uniaxial anisotropy, *2K⊥/M* can be clearly observed with increasing the thickness of the *Cr* spacing layer in the *FeCoB/Cr/FeCoB* multilayers. This could result from the effective modification of surface and interface anisotropic energy as a function of the spacing layer thickness. An effective magnetic anisotropy in the perpendicular direction is introduced into the free magnetic energy density due to the interface and surface contributions, which is directly related to the interlayer interactions and therefore shows an oscillatory change as a result of increasing the thickness of the spacing layers. It is important to mention that the interlayer coupling between the FM layers can be used as an additional means to optimize the magnetic anisotropic parameters in multilayer magnetic structures (simply by tuning the thickness of the spacing AFM layer.)

4.2.2 FMR linewidth and spin wave relaxation

Magnetic relaxation dynamics (damping) are of paramount importance for rf/microwave applications such as microwave band stop filters and more. Large FMR linewidth leads to a reduced quality factor and increased insertion loss, which are among the major problems associated with microwave band stop filters. So far, significant progress has been made regarding the understanding of the FMR behavior of exchange-coupled FM/AFM bilayers and the physical contribution to the FMR linewidth. However, a relatively small amount of work has been done on the exchange coupled FM/AFM/FM trilayers, and their microwave performances are not well understood. FMR linewidth in our spectra is measured, peak to peak field separation, ΔH_{pp}, as a function of in-plane applied field angle. The intrinsic FMR linewidth can be derived from the free energy density, F by the relation [103]:

$$\Delta H_{in} = \frac{2}{\sqrt{3}} \cdot \frac{1}{\left|\dfrac{\partial \omega}{\partial H_{res}}\right|} \cdot \frac{\alpha \gamma}{M} \left(\frac{\partial^2 F}{\partial \theta^2} + \frac{1}{\sin^2 \theta} \cdot \frac{\partial^2 F}{\partial \varphi^2} \right). \tag{4.5}$$

where α is a Gilbert damping parameter which determines how fast the energy of the magnetization precession is dissipated from the system.

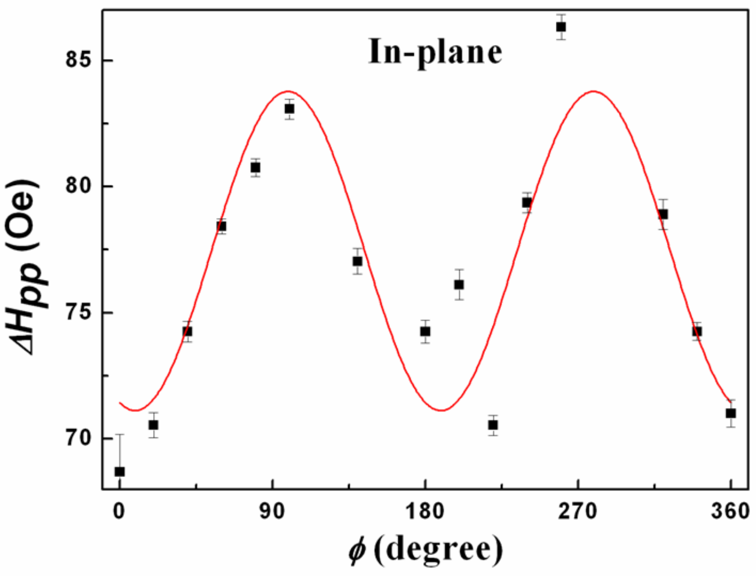

Fig. 4.16 FMR linewidth as a function of the in-plane applied field angle, φ, for the sample with 20 Å *Cr* layers. The solid red line shows the fitting result using Eq. (4.9)

Fig. 4.16 illustrates the FMR linewidth as a function of the in-plane angle, Φ, between the applied field and the easy axis in the sample with 20-Å *Cr* layers. The solid line shows a fit by using Eq. (4.5). The Gilbert damping parameter α is calculated according to the above equation which yields $\alpha = 0.0101 \pm 0.0005$.

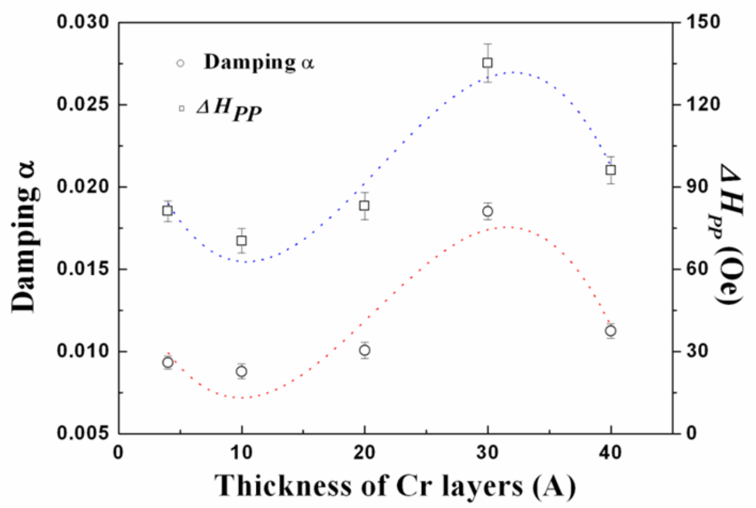

Fig. 4.17 FMR linewidth and magnetization damping constant α as a function of the thickness of *Cr* layers. Both of them show the oscillatory change, which is consistent with the variation of interlayer constant J_{eff}. This suggests that the interlayer coupling plays an important role in determining the magnetization relaxation dynamics in multilayer materials. The dashed line is only meant to guide the eyes.

Fig. 4.17 shows the FMR linewidth and α as a function of *Cr* layer thickness for the *FeCoB/Cr/FeCoB* multilayer samples. The magnetic field is applied along their in-plane easy axis direction. As illustrated in Fig. 4.17, there is an oscillation for both the damping constant α as well as FMR linewidth which is consistent with the variation of interlayer constant J_{eff}. The result suggests that the interlayer coupling plays an important role in determining the magnetization relaxation dynamics in multilayer materials. The itinerant electrons introduce an extra exchange interaction. An extra relaxation torque will be added into the system and contributes to the FMR linewidth in the multilayer structures [104]. An oscillatory change of the FMR linewidth is expect with increasing the thickness of the spacing layer, since the exchange interaction is determined by the density of itinerant electron states. Thus, compared with single and bilayer structures, multilayer structures show an additional degree of freedom to control the magnetic anisotropic and relaxation properties (simply by varying the interlayer coupling between the neighboring FM layers) in addition to a higher effective magnetization.

In summary, the FMR measurements were carried out for multilayer FeCoB/Cr/FeCoB films with the Cr layer thicknesses varying from 4 to 40 Å. the magnetic dynamical properties were investigated including magnetic anisotropies, spin wave modes, interlayer coupling and magnetization damping. Our results reveal that the interlayer coupling between the FM layers in the magnetic multilayer structure can be used as an additional means to optimize the magnetic anisotropy and magnetic relaxation properties in multilayer magnetic structures.

Chapter 5 Non-thermal excitation and control of magnetization in Fe/GaAs thin film by femtosecond laser pulses

A challenging issue in the modern field of magnetic materials is the study of dynamical magnetism under ultra-short external excitation, which has the potential to impact both fundamental science and technological applications [27, 29, 30, 105-107]. The use of femtosecond laser light in the time-resolved pump-probe MOKE spectroscopy is very desirable for investigating ultrafast magnetism on the picosecond and sub-picosecond time scale [34, 38, 108-110]. The thermal excitation of the magnetization by laser pulses has been well studied [32, 111-114], however, laser induced non-thermal magnetization excitation is still not completely understood.

In this chapter, we present our study on magnetism within the time scale of a few picoseconds. We investigated the non-thermal excitation and manipulation of magnetization in Fe/GaAs thin film by time-resolved pump-probe MOKE spectroscopy. Our results reveal a coherent control of the magnetization reorientation by the femtosecond laser pulse. The samples and experiment setup are described in chapter 3.

5.1 Pump polarization dependent time-resolved pump-probe MOKE spectra

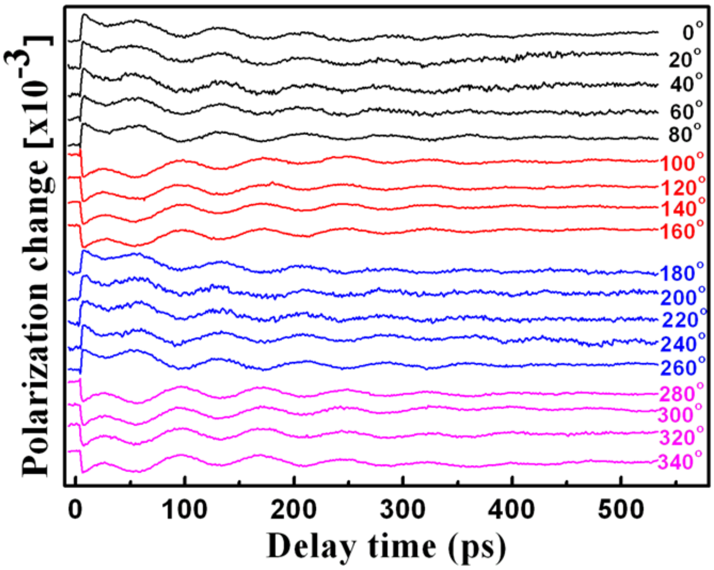

Fig. 5.1 Time-resolved pump-probe MOKE spectrum at various pump polarization angle. The rapid jump in the first few picosecond of the time-resolved MOKE signal periodically appears as a function of the pump polarization.

The time-resolved MOKE technique was first applied to the Fe/GaAs thin film. Fig. 5.1 shows the evolution of the time-resolved MOKE spectrum measured at various pump polarization angles respect to the [010] easy axis. The oscillations in the spectra show π phase shift periodically as the pump polarization is tuned from 0 degree to 340 degree. In addition, we are more interested in the initial signal on a few picoseconds scale after time-zero (t = 0). Within this time domain, the signal shows a sharp jump-up when the pump polarization is oriented in between 0 and 80 degree (also between 180 and 260 degree). In the meanwhile, a rapid jump-down in the signal is monitored when the pump polarization is oriented in between 100 and 160 degree (also between 280 and 340 degree). A four-fold switch in time-resolved MOKE signal is clearly observed.

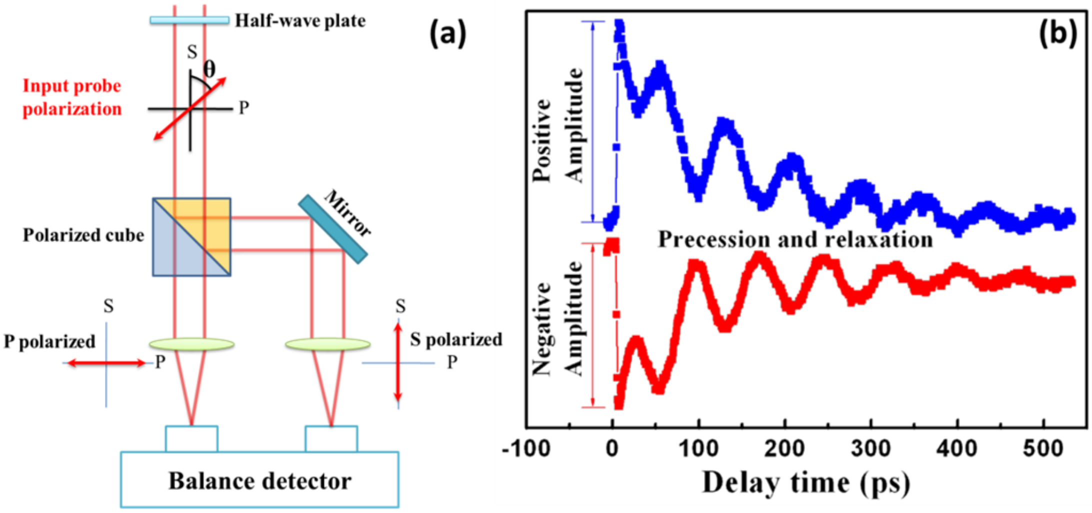

Fig. 5.2 (a) Schematic diagram of the signal collection system. The output signal represents the rotation of reflected probe beam induced by the interaction between the sample and pump beam. (b) Definition of positive and negative excitation amplitude in the time-resolved pump-probe MOKE spectra. The positive excitation stands for the clockwise rotation of the reflective probe polarization, while the negative excitation is because of the counter-clockwise rotation of the reflected probe beam after pump pulse hits the sample.

The sharp jump-up and jump-down in the signal are due to the rotation of the reflected probe polarization induced by the pump in the sample. As shown in Fig. 5.2 (a), the reflected probe beam is input in a polarized cube. The polarized cube divides reflected probe beam into two beams with the electrical fields along *P* and *S* directions. The electrical field relations are described as $E_P = E_{probe} \cdot sin\theta$, $E_S = E_{probe} \cdot cos\theta$ where E_{probe} is the electrical field of reflected probe beam. The output signal from the balanced detector is $I_{output} = I_p - I_s = {E_{probe}}^2 \cdot sin^2\theta - {E_{probe}}^2 \cdot cos^2\theta$. Therefore, if the polarization of reflected probe rotates clockwise, the output signal will increase; while the output signal will decrease if the polarization of reflected probe rotates counter-clockwise. As shown in Fig. 5.2 (b), the initial single represents the I_{output} before the pump pulse interacts with the sample. After the pump pulse hits the sample, the signal in blue spectrum shows a sharp increase which means the polarization of probe beam rotating clockwise. The signal in red spectrum shows a sharp decrease which means the polarization of probe beam rotating counter-clockwise.

The sharp increasing or decreasing in the time-resolved pump-probe MOKE signal right after time zero reaches the maximum at 3 picoseconds. We define the excitation amplitude as the subtraction between the signal at t = 3 ps and t = -3 ps as shown in Fig. 5.2 (b). Therefore, the excitation amplitude is positive for the blue spectrum but negative for the red spectrum. In addition, it is noticed that there is a π oscillation phase shit between the positive and negative excitation spectra. The variation of MOKE signal indicates the change of magnetization projection in the incident plane of probe beam. Therefore, the positive and negative excitations represent the variation of the magnetization vector in the sample plane. As discussed in chapter 4, the oscillation in the MOKE signal is because of the precession of the magnetization vector. Thus, the π oscillation phase shift in our results indicates that the magnetization vector precesses in the opposite direction after the positive or negative magnetization excitation.

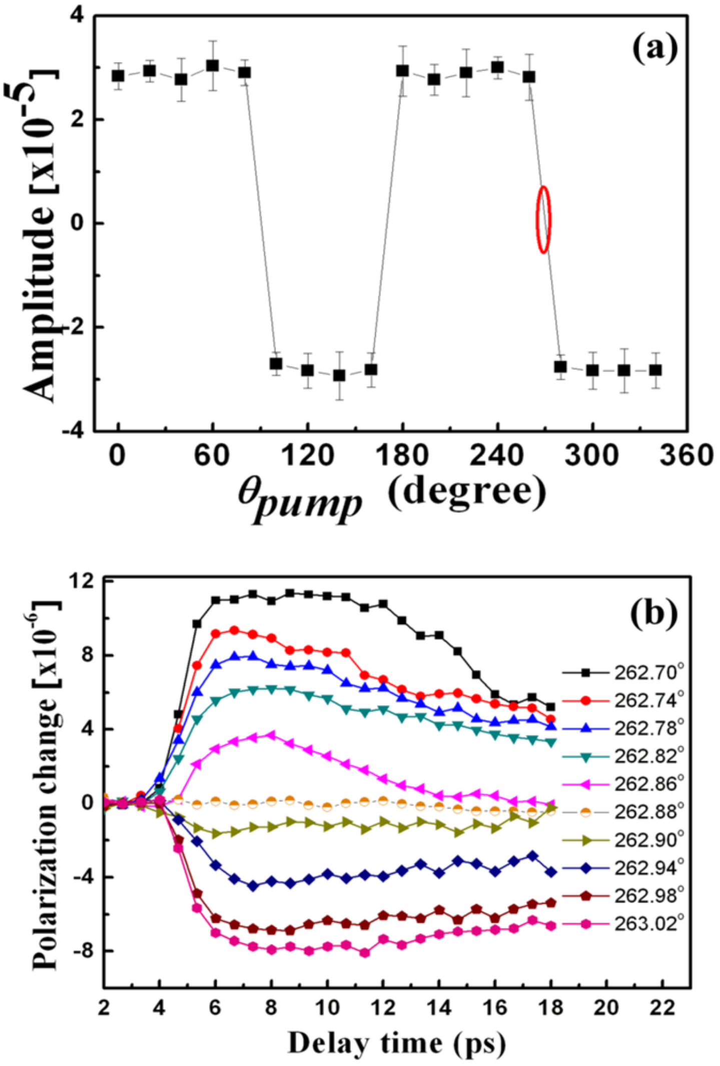

Fig. 5.3 (a) Excitation amplitudes plot as a function of pump beam polarization angle. The excitation amplitudes show four-fold distribution as a function of the pump polarization. The reversal of the excitation from positive to negative appears close to the crystal axis. (b) Evolution of time-resolved MOKE spectra around the [-100] axis. The excitation gradually evolves from positive to negative as the pump polarization is rotated from the 262.70 to 263.02 .

The magnetization excitation amplitudes are plotted as a function of pump polarization angle in Fig. 5.3 (a). A clear four-fold distribution of the excitation amplitude is observed as pump polarization is rotated in the sample plane. The positive and negative excitation amplitude periodically appears as a function of pump polarization angle. Moreover, the switch of the magnetization excitation amplitude only appears when the pump polarization is placed close to the crystal axis. To unveil the evolution of the spectrum within this small angle, a fine scan is carried out as shown in Fig. 5.3(b). When the pump polarization sweeps across the [-100] axis, the magnetization excitation amplitude gradually varies from positive to negative. The results reveal that the reversal of the magnetization excitation amplitude is a continuous process. It turns out that the direction of the magnetization excitation and reorientation is closely related to the polarization of pump pulse which indicates a non-thermal origin of magnetization dynamics in Fe thin films.

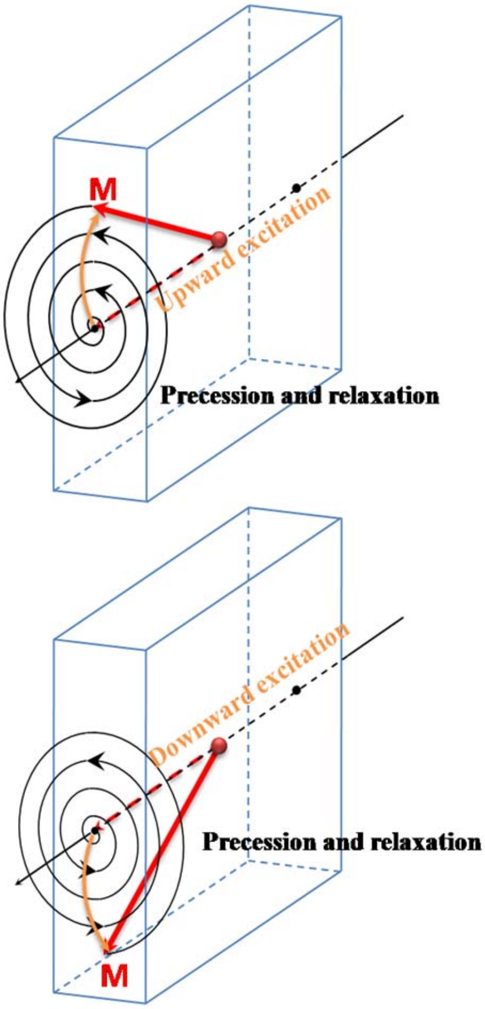

Fig. 5.4 Magnetization excitation and reorientation mechanism. Under pump laser different polarization, the magnetization vector is excited and reoriented to the different direction followed by the precession and relaxation.

We propose a model to explain the dramatic change of the time-resolved pump-probe MOKE signal as shown in Fig. 5.4. The dashed line represents the equilibrium position of the magnetization, the red arrow stands for the magnetization vector, and the solid orange line is the trajectory of the magnetization excitation. The solid black spiral represents the precessional trajectory of the magnetization. When pump pulses are applied along the in-plane hard axis direction, the vector of magnetization rotates away from its equilibrium position. The magnetization vector relaxes back to its original position by precessional motion after the pump pulse disturbance. It is noticed that the precessional traces have π phase difference between each other which is due to the opposite magnetization excitation. This phenomenon is also observed in the ultrafast study of garnet films [110, 115]. The magnetization excitation is significantly weaker and becomes difficult to observe if the external field is applied close to the easy axes along which the magnetization is pinned as indicated in Fig. 5.3 (b).

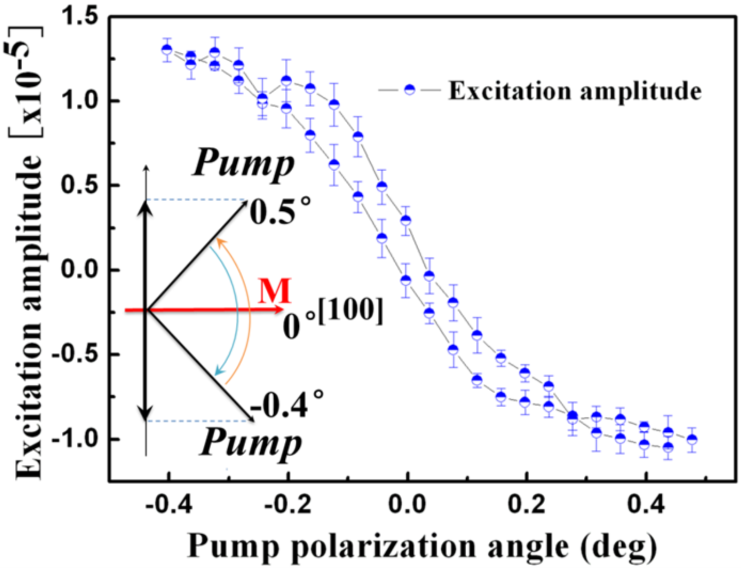

Fig. 5.5 Excitation amplitude vs. pump polarization angle from -0.4° to 0.5° compared to the [-100] axis. The hysteresis loop like result indicates that the magnetization is driven by an effective field induced by the femtosecond laser pulse in the sample. Inset shows the measurement configurations.

Moreover, the fine scan of time-resolved pump-probe MOKE spectra is carried out by sweeping the pump polarization angle from -0.4° to 0.5° back and forth, relative to the [100] axis as shown in the inset of Fig. 5.5. The excitation amplitudes (blue dots) are plotted as a function of the pump beam polarization angle. We observe a hysteresis-like loop curve. The results are explained as follows: the sample is magnetized and demagnetized along the [010] or [0-10] axis by the effective pulsed magnetic field induced by the polarization of the pump laser pulses. The hysteresis-like loop is not saturated since the effective field is not strong enough to fully magnetize the sample.

5.2 Double Pump pulses induced magnetization excitation

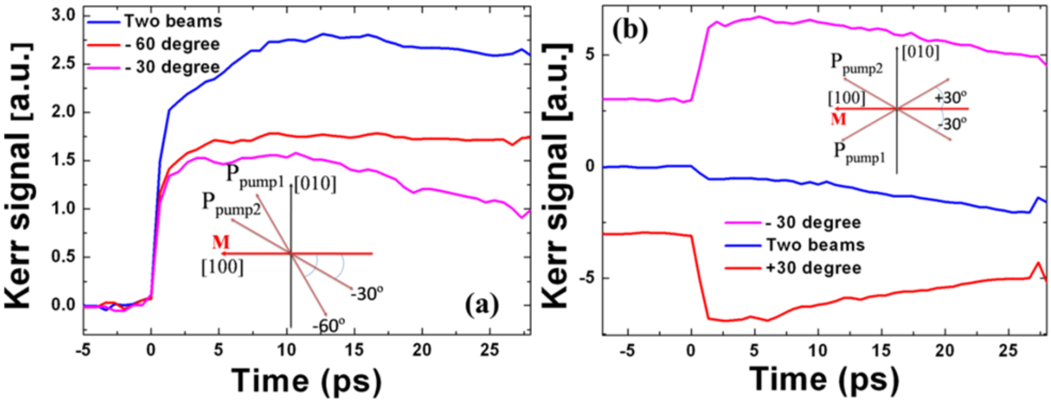

Fig. 5.6 (a) Time-resolved pump-probe MOKE spectra under the applied single pump polarization angle at -30º (pink) and -60º (red). The solid blue curve is the result when two pump beams were applied simultaneously. (b) Time-resolved pump-probe MOKE spectra under the applied single pump polarization angle at -30º (pink) and +30º (red). The solid blue curve is the result when two pump pulses were applied simultaneously. The three curves are offset for a better view. The polarizations of the double pump excitations are displayed in the inset.

Next, we employed double pump beams to investigate the magnetization excitation amplitude. Fig. 5.6 shows the results while the pump polarizations are shown in the inset figure. In Fig. 5.6 (a), under the pump polarization angle at -30º and -60º, the time-resolved pump-probe MOKE spectrum both show upward excitation which is consistent with the former results. If the orientation of two pulsed magnetic fields induced by the two pump beams are at the same side of the equilibrium magnetization, as shown in the inset of Fig. 5.6 (a), both an enhanced magnetization rotation and therefore an enhanced upward excitation are expected when the two pump polarizations applied to the sample simultaneously. The blue curve in Fig. 5.6 (a) is the experimental result when double pumps are applied simultaneously. This enhancement satisfies our expectation. What if the double pump beams are applied in the opposite orientation, as shown in the inset of Fig. 5.6 (b), the polarization angles are at -30º and +30º compared to equilibrium magnetization direction? Individually, the two pump pulses create the upward (pink) and downward (red) excitation. When the orientations of the two ultrafast magnetic fields induced by the two pump beams are opposite to the equilibrium magnetization as shown in the inset of Fig. 5.6 (b), there is no rotation of magnetization correspondingly. Therefore no magnetization excitation should be observed in the time-resolved pump-probe MOKE signal. The experimental result is shown in Fig. 5.6 (b) by the blue curve. Although the excitation amplitude doesn't completely disappear, the greatly dampened magnetization excitation result agrees with our anticipation. The tiny excitation amplitude may result from the slight misalignment of the laser polarizations.

The origin of this laser polarization dependent magnetization excitation may lie in the metal/semiconductor junction of our sample. Recent studies showed that the laser induced spin-orbit interaction is capable to manipulate the electron spin [116, 117]. Especially in the metal/semiconductor junction structure, spin-orbit coupling appears as a effectively magnetic field acting on the electron spin [118]. In our experiments, the ultrafast laser pulses strongly enhanced the spin-orbital coupling [75] leading to a pulsed anisotropic field in the metal/semiconductor junction which excited the magnetization in the iron layer.

In summary, time-resolved pump-probe MOKE spectroscopy was used to study ultrafast magnetization dynamics in the 10 nm epitaxially grown Fe/GaAs thin film. The magnetization excitation and reorientation exhibit strong dependence on the polarization of the pump beam. The result suggests a non-thermal origin of magnetization dynamics in the Fe/GaAs thin film in which there is a pulsed magnetic field induced by pump pulses. Our results show the feasibilities of non-thermal ultrafast optical control of magnetization responses in soft magnetic thin films.

Chapter 6 Ultrafast demagnetization in Fe/GaAs thin films

The femtosecond laser pulses induced ultrafast demagnetization emerges to be a hot topic because of its direct application in the magnetic recording devices. Such effect was first reported in the Ni sample by Beaurepaire *et al*. [119], where they observed a sharp signal loss in the time-resolved pump-probe MOKE spectra within one picosecond after the pump pulses were absorbed. Although many investigations [32, 111-114] have been carried out to understand the underlying mechanism of this intriguing phenomenon. However, the understanding of femtosecond laser induced ultrafast demagnetization is still debating.

In this chapter, we present our studies combining the time-resolved pump-probe MOKE technique with transient magnetic hysteresis loops to investigate the ultrafast demagnetization in the 10 nm *Fe* thin film samples. The demagnetization time is found to be shorter than the electron-phonon thermalization time. We discuss the ultrafast demagnetization mechanism according to the electron-thermalization and spin-orbital interactions.

6.1 Time-resolved pump-probe MOKE results

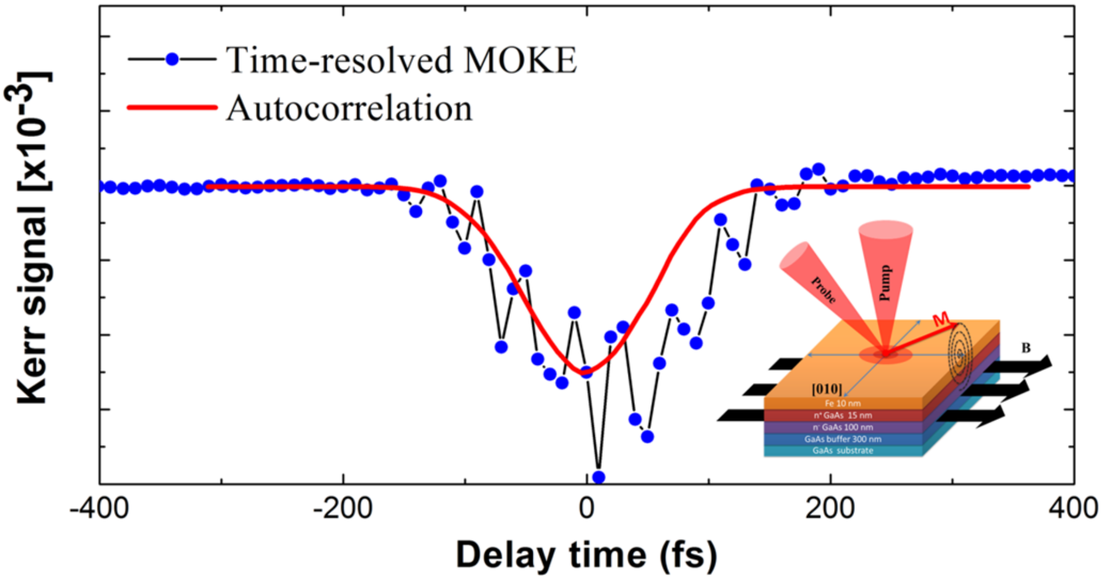

Fig. 6.1 Time-resolved MOKE trace from -400 to 400 femtoseconds (blue dots). The autocorrelation is shown in red solid line. The inset shows the sample structure and the experimental geometry. The rapid decrease of the MOKE signal represents the ultrafast demagnetization process.

Our interest is within the hundreds femtoseconds scale as the laser pulse is starting to interact with the sample. The time-resolved MOKE spectroscopy is utilized to unveil the magnetization dynamics on this time scale. The sample and measurement set up are the same as described in chapter 3. As shown in Fig. 6.1, the time interval for the scan is 10 femtoseconds, a huge vibration of the time-resolved MOKE signal close to time-zero is observed. The time-zero is defined as the moment (t = 0) when pump and probe pulse completely overlap with each other as shown by the autocorrelation in Fig. 6.1.

6.2 Femtosecond demagnetization

As described by Eq. (2.37) in chapter 2, time-resolved MOKE signal provides information on the magnetic state of a material. The magnitude of the Kerr rotation is directly proportional to the magnetization of the sample. Therefore, the magnetization change can be monitored by measuring MOKE signal as a function of external magnetic.

In addition, the time-resolved MOKE hysteresis loops measurements are employed to investigate the magnetization dynamics as a function of time. The measurement is performed by recording full hysteresis loops in longitudinal configuration at every time delay. By this means, the shape of the hysteresis loop can be used as a monitor of the magnetization excitation and relaxation [120]. The time-resolved hysteresis loop measurements are applied within 300 femtoseconds around the time-zero position to monitor the ultrafast variation of the magnetization.

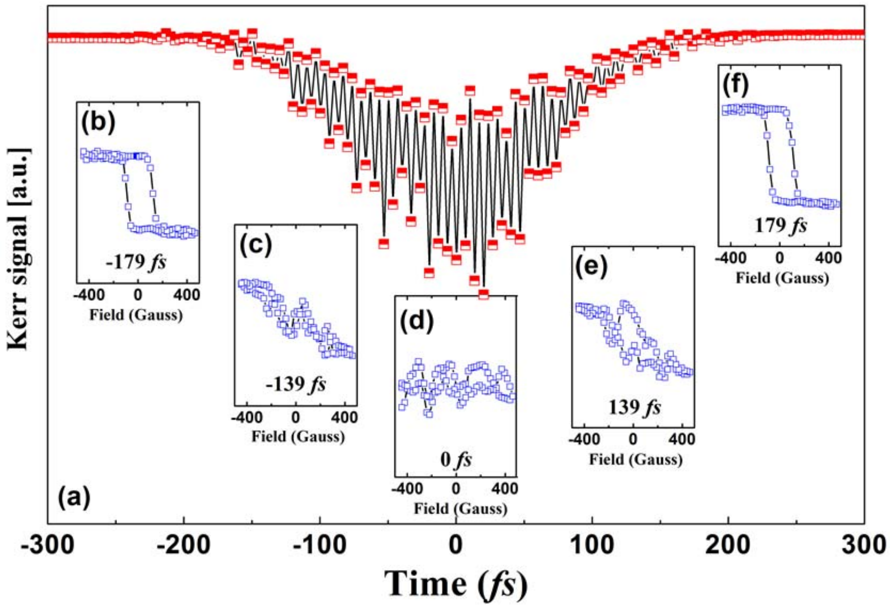

Fig. 6.2 (a) Time-resolved MOKE signal with step size 3.3 *fs*. The inset figures (b), (c), (d), (e), (f) show the time-resolved hysteresis loops at various time delays. The evolution of the time resolved hysteresis loops show an ultrafast demagnetization happens with in hundreds femtoseconds time scale.

First, close to the time-zero, the ultrafine scan with the step size 3.3 femtoseconds and 50 times average is carried out as shown in Fig. 6.2 (a). The purpose is to map out the clear profile of the time-resolved pump-probe MOKE response and then choose different time locations to record the hysteresis loops.

The vibrating time-resolved MOKE signal starts around -200 *fs* which indicates the laser pulse starts to deposit the energy into the magnetic system. As the time is approaching the time-zero, the maximum laser pulse energy is input into the sample which causes the most furious vibration of the MOKE signal. We use the time resolved magnetic hysteresis loops at different time delays as shown in Fig. 6.2 (b)-(f) to further identify the magnetic origin of the time resolved MOKE signal [121, 122]. We observed that, At t = -197 *fs*, the magnetic hysteresis loop is still the square shape similar to that from the vibrating sample magnetometer, which indicates the magnetic moments have not yet been disturbed by the pump laser pulse. At t = -139 *fs*, a significant change in the shape of the hysteresis loop is observed. Both the coercivity and saturate-to-saturate magnetization of the hysteresis loop are being quenched even before time zero. Because the energy has already started to be deposited, the sample has absorbed small amount of photons and starts to be demagnetized as described in Si and Zhang's work [123]. Between t = -129 and 129 *fs*, the absorption of the pump energy reaches the maximum which causes the maximum quenching of the magnetization. This leads to hysteresis loop shown in Fig. 6.2 (d). The hysteresis loop trends to recover to its original square shape at t = 139 *fs*. This indicates that the magnetic moments start to restore their ordered distribution after laser excitation. At t = 179 *fs*, the hysteresis loop recoveries its original square shape as shown in Fig. 6.2 (f).

In the demagnetization process, the longitudinal MOKE signal is proportional to the magnetization in the in-plane field direction[124]. In the meantime, the intensity of the hysteresis loop is the direct indictor of the magnetization which participates in the reversal process under an applied in-plane magnetic field. The intensity of the hysteresis is defined as the signal difference of hysteresis loop as the magnetic field is swept from -400 Gauss to + 400 Gauss.

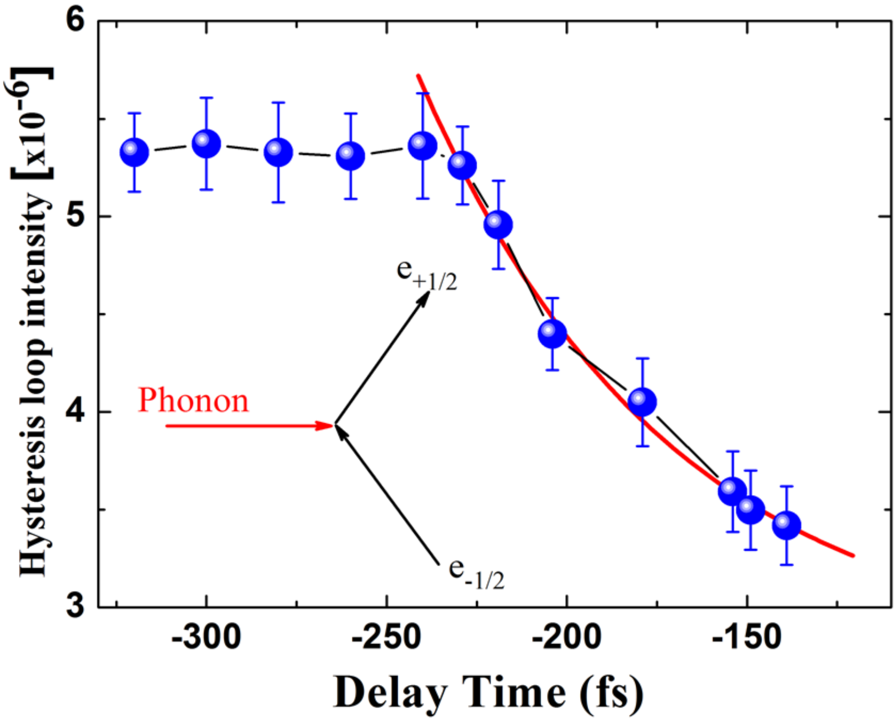

Fig. 6.3 Intensity of the magnetic hysteresis loops as a function of time. Red solid line is the fitting to the intensity curve with exponential decay function. Inset shows the schematic diagram of the Elliot–Yafet type of spin scattering.

Fig. 6.3 shows the intensity of the time-resolved hysteresis loops plot as a function of time in demagnetizing section. Apparently the hysteresis loop intensity remains the same value before the laser pulses hit the sample. Around - 229 *fs* when the laser pulse begins to interact with the sample, the hysteresis loop intensity starts to decrease until -129 *fs*. The hysteresis loop intensity between -229 to -139 *fs* is fit with the exponential decay function. The demagnetization time $\tau_M \sim 70$ *fs* is obtained. We explain the observed results based on the Koopmans' model [125] which considers the probability that an electron flips its spin on emission or absorption of a phonon (inset of Fig. 6.3). The model predicted the possibility to obtain a demagnetization time shorter than the electron–phonon equilibration time. The demagnetization time τ_M is directly related to the Gilbert damping constant α [70]:

$$\tau_M = c_0 F(T) \frac{\hbar}{k_B T_c} \cdot \frac{1}{\alpha} \approx c_0 \frac{\hbar}{k_B T_c} \cdot \frac{1}{\alpha} \ . \tag{6.2}$$

where the function $F(T) \sim 1$ at room temperature and the last approximation is valid for T well below T_C. The coefficient$c_0 = 1/4$ for $\tau_M >> \tau_E$, , while $c_0 = 1/8$ for $\tau_M << \tau_E$, where τ_E is the electron-phonon equilibrium time.

All our measurements are carried out under room temperature. The T_C for *Fe* is 1043 K, therefore the approximation is satisfied. By using the damping constant $\alpha \sim 0.012$, $c_0 = 1/8$, the estimated τ_M = 76 *fs matches with* our experimental result which is 70 *fs.* The result indicates that the demagnetization completes before electron-phonon equilibration is achieved in our sample.

6.3 Laser power dependent time-resolved hysteresis loops

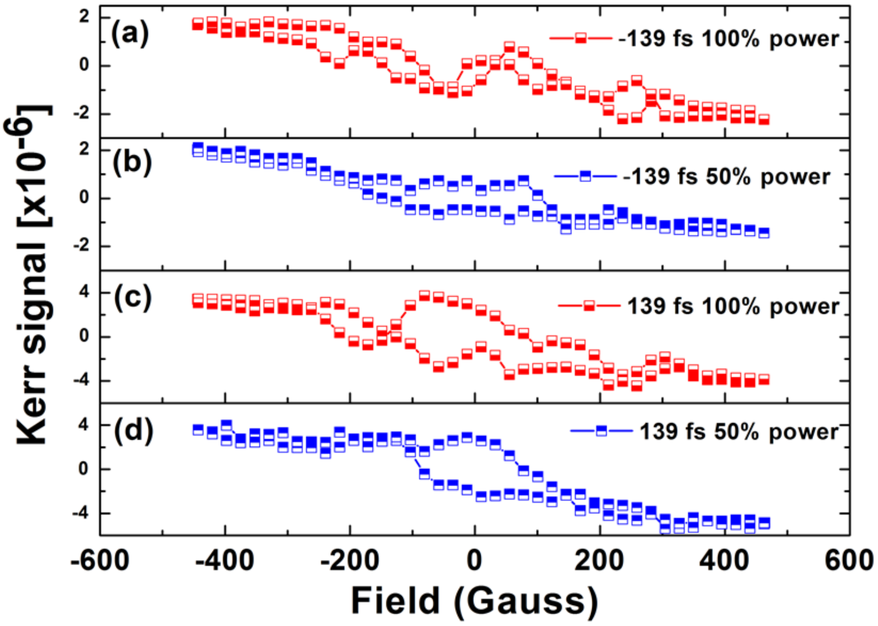

Fig. 6.4 (a), (b), (c), (d) show the hysteresis loops at ± 139 *fs* with various pump powers. The variation of the time-resolved hysteresis loop profile indicates that the electron thermalization

model cannot fully explain the ultrafast demagnetization in our sample.

Fig. 6.4 (b) and (d) show the hysteresis loops at -139 *fs* and +139 *fs*, respectively with 50 % pump power. Compared to the hysteresis loops at the same time delays with 100% pump power which are shown in Fig. 6.4 (a), (c), the hysteresis loops measured by 50% pump power hold more square-like shape which means they are quenched much less than hysteresis loops with 100% pump power. This result is consistent with the Si and Zhang's work [123] which reveals that the demagnetization depends on the pump intensity. Moreover, a clear evaluation in hysteresis loop shape is observed towards the quenching of the magnetization. The result cannot be simply understood by the electron thermalization mechanism. The evolution shows a strong dependence of the pump power and time delay between pump and probe pulses.

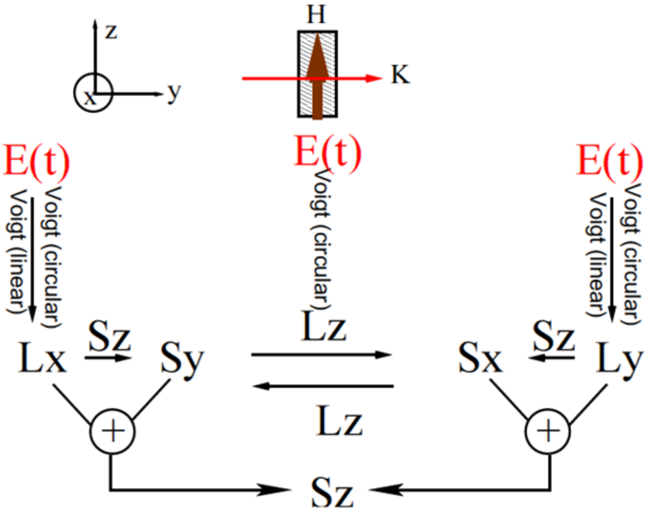

Fig. 6.5 Illustration of laser changing the magnetization under spin-orbital coupling mechanism. The electric field of the laser pulse alters the orbital momentum of the electrons. With the spin-orbital coupling, the spin momentum is changed corresponding to the orbital momentum.

In addition to the laser induced electron thermalization mechanism, spin-orbital coupling model described by G. P. Zhang *et al*, [73-75] explains the ultrafast demagnetization by considering the interaction between the spin momentum and the orbital momentum. In which the spin-orbital coupling term is added into the Hamiltonian [126]:

$$H = \frac{p^2}{2m} + \lambda\left(L_x S_x + L_y S_y + L_z S_z\right) + \boldsymbol{r} \cdot \boldsymbol{E}(t). \tag{6.3}$$

where the first term is the kinetic energy of the electron, P is the electron momentum operator, m is the effective mass of electrons. One single electron spin is considered. λ is the spin-orbital coupling constant. The second term is the spin-orbit coupling and $S_{x(y,z)}$ is the spin operator. $L_{x(y,z)}$ is the orbital momentum operator. $\boldsymbol{r}$ is the electron position and $\boldsymbol{E(t)}$ is the laser field. Under the Heisenberg picture, the time evolution of the orbital momentum is written as:

$$\begin{aligned} \dot{L}_x &= -\lambda(L_y S_z - L_z S_y) - yE_z(t), \\ \dot{L}_y &= -\lambda(L_z S_x - L_x S_z) + xE_z(t), \\ \dot{L}_x &= -\lambda(L_x S_y - L_y S_x). \end{aligned} \tag{6.4}$$

Combining with Eq. (6.4), the spin-orbital coupling effect participates in the ultrafast demagnetization process is shown in Fig. 6.5. (1) The magnetization quantization is along the z axis (2) The light propagates along the *y* axis; (3) The light polarization is within the *x-z* plane. There are two equivalent channels to change the spin momentum along the *z*-direction. One is from the orbital momentum L_y and the other is from the orbital momentum L_x. Taking L_y as an example, when L_y is excited under the pump laser, without the spin-orbital coupling, S_x will remain zero. However, under the spin-orbital coupling effect, S_x starts to change which leads to the spin momentum change in *z*-direction. This explains the variation of the hysteresis loop profiles in our time and pump power dependent experimental results. Therefore, the spin-orbital coupling effect should be also included in addition to the electron thermalization effect to explain our demagnetization results.

In summary, both the time-resolved pump-probe MOKE spectroscopy and time-resolved hysteresis loop measurements were employed to study the ultrafast demagnetization in the 10 nm iron thin film. According to Koopmans' model, our result show that the demagnetization completes before electron-phonon equilibration is achieved in our sample. Based on the variation of the time-resolved hysteresis loops, we concluded that the spin-orbital coupling mechanism needs to be included in addition to the electron-thermalization mechanism to explain our ultrafast demagnetization results.

Chapter 7 Ultrafast quasiparticle relaxation dynamics in electron-doped superconductor $BaFe_{1.9}Ni_{0.1}As_2$ and $BaFe_{1.85}Co_{0.15}As_2$

Understanding the complex behavior of electron and phonon systems, especially in high-temperature superconductors, is one of the most important challenges in condensed matter physics. The recent discovery of iron pnictides superconductor [91] with $T_c = 26$ K, attracted a lot of attention from the research community. The transition temperature in this class of superconductors has been increased over 50 K. The phase diagram of iron pnictides suggests an unconventional pairing mechanism. Until now, a lot investigations have been made to this class of compound [127-130] , however the detailed mechanism is not completely clear.

In this chapter, the time-resolved pump-probe optical spectroscopy is employed to study the relaxation dynamics in the electron-doped superconductor, $BaFe_{1.9}Ni_{0.1}As_2$ (BFNA) and $BaFe_{1.85}Co_{0.15}As_2$ (BFCA). Distinct quasiparticle relaxations are observed in our transient reflectivity spectra. The quasiparticle relaxation mechanisms are discussed based on Kabanov’s theory described in chapter 2.

7.1 Temperature dependent transient reflectivity spectra in BFNA

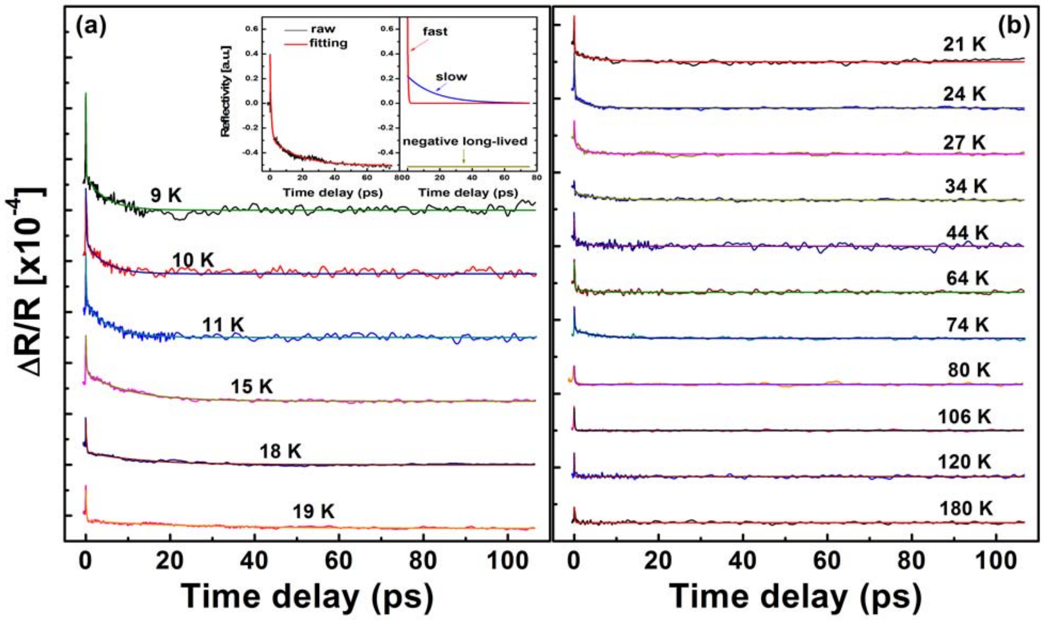

Fig. 7.1 Transient reflectivity spectra under different temperature. Inset shows the fitting procedure. Two distinct quasiparticle relaxations and one long lived relaxation component are identified in our measured transient reflectivity signal.

By applying the time-resolved pump-probe reflectivity measurement, the response of the electron-phonon system is studied in the time domain. Fig. 7.1 shows typical temporal traces of the transient reflectivity change at various temperatures in BFNA. The temporal evolution of the transient reflectivity spectrum is fitted by two exponentials: $\Delta R / R = A_0 + A_{fast} \exp(-t / \tau_{fast}) + A_{slow} \exp(-t / \tau_{slow})$. The inset of Fig. 7.1 (a) demonstrates the three components in the reflectivity signal. Below T_C, The fast component, τ_{fast}, is on the order of 0.2 *ps* while the slow component, τ_{slow}, is on the order of 10 ps. In addition, a very long-lived relaxation component is clearly observable. It has negative amplitude and a sub-nanosecond relaxation time.

7.2 Distinct quasiparticle relaxations in BFNA

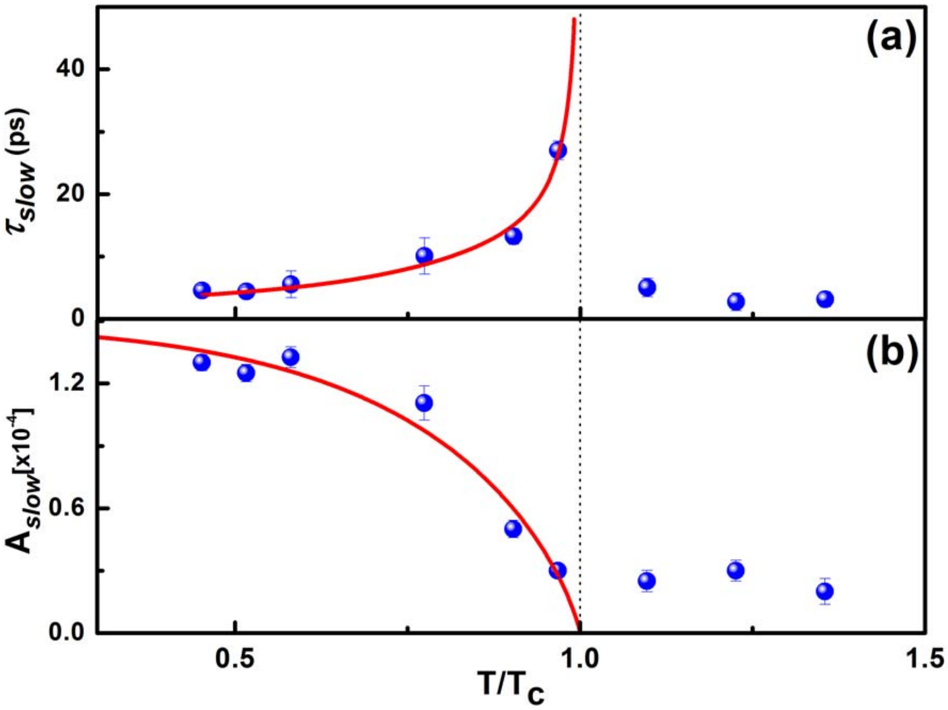

Fig. 7.2 (a) Temperature dependent relaxation time, τ_{slow}, and (b) Temperature dependent relaxation amplitude, A_{slow}. The SC gap is extracted from the temperature dependent relaxation time, τ_{slow}, according to Kabanov's model. By using the extracted SC gap, the temperature dependent relaxation amplitude , A_{slow}, is well fitted.

The slow relaxation process is evidently related to superconducting phase transition since its lifetime changes sharply and its amplitude remarkably decreases when the temperature is approaching T_C from below. This component is attributed to the Cooper-pair recombination after the photo-excitation. The relaxation time, τ_{slow}, and photoinduced reflectivity amplitude, A_{slow}, are extracted as shown in Fig. 7.2 (a) and (b). According to the Kabanov model [60], the temperature dependence of the relaxation time, τ_{slow}, is described as:

$$\tau_{slow} \propto \frac{\ln\left\{1/\left(\frac{E_I}{2N(0)[\Delta(0)]^2}+e^{-\Delta(T)/k_BT}\right)\right\}}{[\Delta(T)]^2}. \tag{7.1}$$

where E_I is the incident energy density, $N(0)$ is the density of the state at E_f, and $\Delta(T)$ is the superconducting gap obeying the BCS temperature dependence. Fig. 7.2 (a) shows the fit of τ_{slow}. The superconducting gap, $\Delta(0)$, is obtained to be ~ 3.3 k_BT_c. The result is further confirmed by the temperature dependence of A_{slow}. Based on the $N(0) \cong 2$ eV^{-1}cell^{-1}spin^{-1} [131], the E_I is estimated as of ~ 4.8 × 10^{-5} eV^{-1}cell^{-1}spin^{-1}. The signal amplitude is proportional to the photo-induced QP density by considering the bottleneck condition and the energy conservation law. The density of the thermally excited QPs is defined by: $n_T \propto \sqrt{\Delta(T)T} \cdot \exp(-\frac{\Delta(T)}{T})$. The slow relaxation below T_C is ascribed to the QP relaxation across the superconductor gap. As a result, the significant drop of A_{slow} near T_C can be understood as the annihilation of the QPs as the temperature increases. The temperature dependent relaxation amplitude takes the form:[60]

$$A_{slow} \propto \frac{E_I / \left(\Delta(T) + k_B T / 2\right)}{1 + \frac{2\nu}{N(0)\hbar\Omega_c} \cdot \sqrt{\frac{2k_BT}{\pi\Delta(T)}} \cdot \exp\left[-\Delta(T)/k_BT\right]}. \qquad (7.2)$$

where Ω_c is the photon frequency cut off and ν is the effective number of phonon modes per unit cell participating in the relaxation. By using $\Delta(0) \sim 3.3k_BT_c$ obtained from the fitting of τ_{slow} and $\Omega_c \cong 60$ meV, [131] a theoretical fit (red solid line) of A_{slow} is obtained in Fig. 7.3 (b), which gives the $\nu = 2.6 \pm 0.5$.

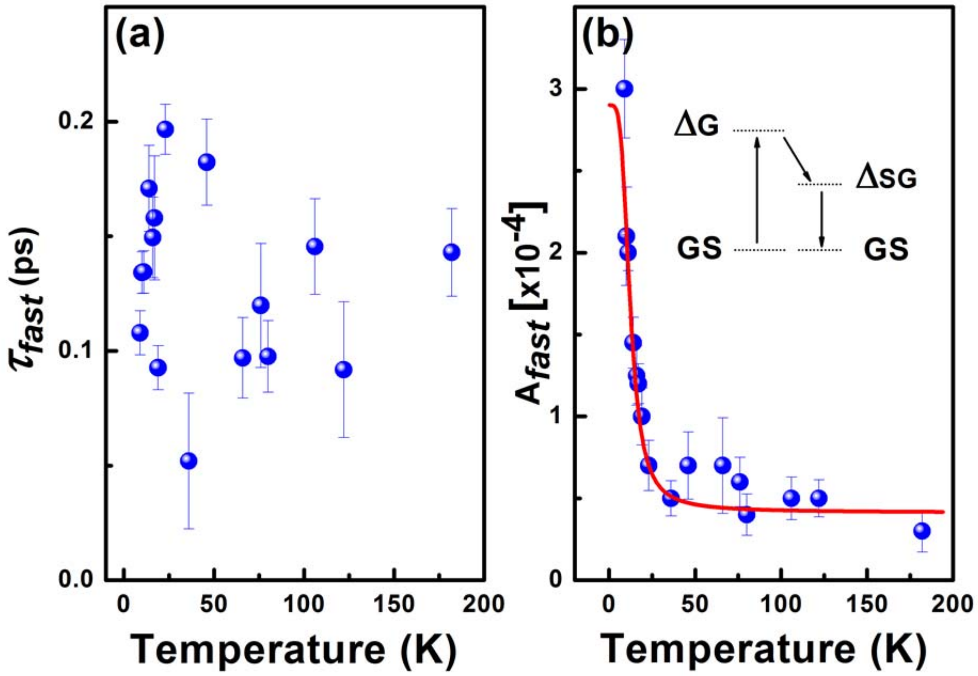

Fig. 7.3 (a) Temperature dependent relaxation time, τ_{fast}, and (b) Temperature dependent relaxation amplitude, A_{fast} for the fast relaxation. The quasiparticle gap is extracted from the fitting to $A_{fast.}$ The inset demonstrates that fast relaxation process is governed by a cascade relaxation from the upper bound of Δ_G to that of the SC gap

Fig. 7.3 shows the photo-induced quasiparticle (a) relaxation time, τ_{fast}, and (b) amplitude, A_{fast}, of the fast relaxation component in BFNA. The amplitude of the fast relaxation component, A_{fast}, presents a clear T-dependent behavior but the relaxation time τ_{fast} has no obvious dependence on temperature. The fast relaxation component is ascribed to the quasiparticle relaxation from a range of large gap states to the state above the superconducting gap. The photo-induced reflectivity amplitude, which is related to the QP density in the excited state under bottleneck condition, takes the form:

$$A_{fast} \propto [1+\frac{2\nu}{N(0)\hbar\Omega_c}\cdot\exp(-\frac{\Delta_G}{k_B T})]^{-1}. \qquad (7.3)$$

where Δ_G is the effective energy of the bandgap (the fit is shown in Fig. 7.3 (b)). By taking the parameters estimated in the slow relaxation, Δ_G is obtained to be 9 ± 1meV. Due to the fact that the relaxation time, τ_{fast}, is much faster than that of SC gap, Δ_G is attributed to a higher lying excited state. One possible explanation is that the relaxation process is governed by a relaxation cascade from the upper bound of Δ_G to that of the SC gap shown in the inset of Fig. 7.3 (b) and then relaxes to the ground state via the SC gap. However, it is hard to rule out the possibility of the direct relaxation form Δ_G to the ground state. Therefore, it is possible that the two relaxation channels coexisted in parallel in the relaxation process.

Moreover, the electron-phonon coupling constant, λ, is estimated from the relaxation dynamics of photo-excited QPs at room temperature by assuming that the electron-phonon interaction dominates the relaxation process in BFNA. In our time-resolved experiments, the electrons are driven to a state of inequilibrium when the pump pulse is absorbed by the sample. Subsequently the electron temperature rises far above that of the lattice. As a result, the electrons lose energy to the lattice through phonon emission. The electron temperature equilibrates with a rate ruled by the strength of electron-phonon coupling. According to the relation between the electron temperature, T_e, and lattice temperature T_l [132], a nonlinear differential equation for T_e is written as:

$$T_e(t)\frac{d^2T_e(t)}{dt^2}+\left[\frac{dT_e(t)}{dt}\right]^2+\frac{3\hbar}{\pi k_B}\lambda<\omega^2>\left[1+\frac{\gamma}{C_l}T_e(t)\right]\frac{dT_e(t)}{dt}=0\,. \qquad (7.4)$$

where C_l is the lattice specific heat and γ is a constant which can be obtained from the electron specific heat $C_e = \gamma T$. The differential equation can be solved analytically by $T_e(t)=Ae^{-\frac{3\hbar\gamma}{2\pi k_B C_l}\lambda<\omega^2>t}+B$ where A and B are determined by $T_e(0)$ and $T_e(\infty)$. ΔR varies in response to both ΔT_e and ΔT_l as $\Delta R=a\Delta T_e(t)+b\Delta T_l(t)$. However, the specific heat of the lattice is much larger than that of electrons and thereby only the electron heating effect is considered in ΔR (the contribution of T_l variation in ΔR should be very weak and decay much longer (>> 10 ps)). The relaxation rate is about 1 picosecond at room temperature. By substituting the parameters: C_l = 25.5 J/mol·K, γ = 23.8 mJ/mol·K^2 [133], $\lambda\langle\omega^2\rangle$ is estimated to be ~ 84.8 meV^2. Based on the mean phonon frequency $\langle\hbar\omega\rangle$ = 23 meV [134], the electron-phonon coupling constant, λ, is extract as of ~ 0.16. Here the approximation: $\langle\omega^2\rangle \approx \langle\omega\rangle^2$ is used.

Within the strong-coupling theory, the McMillan formula for the SC transition temperature in a s-wave superconductor is [135]:

$$T_c = \frac{\theta_D}{1.45}\exp\left[-\frac{1.04(1+\lambda)}{\lambda-\mu^*(1+0.62)}\right]. \tag{7.5}$$

where the renormalization factor, (1 + λ) arises from the s-wave channel of the electron-phonon coupling. The value θ_D ~140 K from a recent thermal conductivity measurement [136] was used in the calculation. Thus, the Coulomb pseudopotential, μ^*, is estimated to be ~ − 0.4. The negative μ^* implies that the electron-phonon interaction alone is not strong enough to induce a SC transition in BFNA. It is possible that both the electron-phonon interactions and non-phonon dominating interactions, such as spin mediated pairing mechanisms, should be included for describing the SC transition in BFNA.

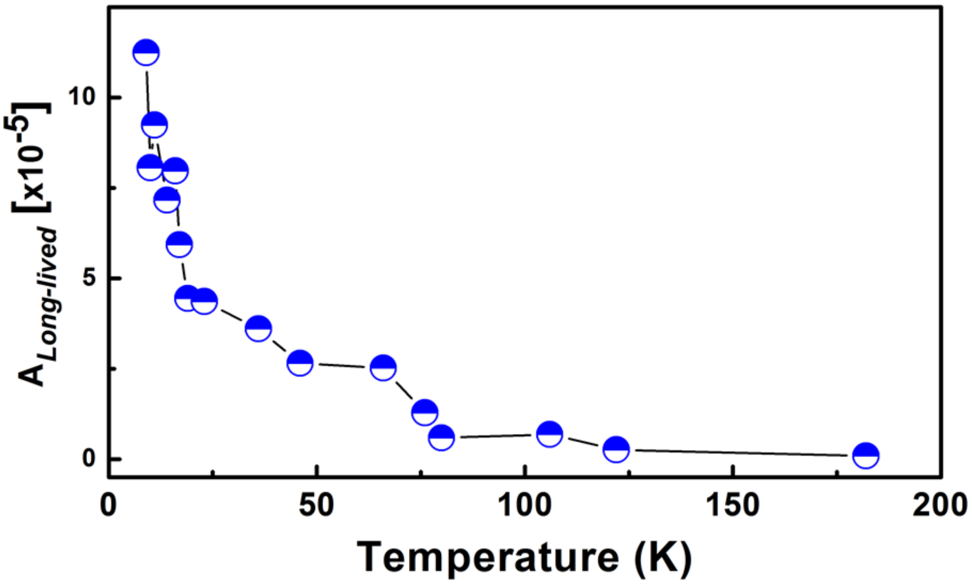

Fig. 7.4 Amplitude of long-lived relaxation component vs temperature. The long-lived relaxation component is attributed to the relaxation of heat via diffusion.

Fig. 7.4 shows the amplitude of the long-lived component, A_{Long}, plotted as a function of temperature. The A_{Long} reaches the maximum at low temperatures and drops quickly to the minimum at high temperature, which is roughly inverse to the behavior of overall specific heat. Therefore, the slow decay process is attributed to the relaxation of heat via diffusion.

7.4 Distinct quasiparticle relaxations in BFCA

We also performed the transient optical reflectivity measurements to the BFCA sample with T_c ~25 K. Similarly, two distinct relaxations and one long lived component were observed in the spectra which yields two quasiparticle gaps $\Delta_1(0) = 3.5 \pm 0.4$ meV and $\Delta_2(0) = 7.4 \pm 1.2$ meV. The results support the multi-gap characteristic in iron based superconductor as observed in BFNA sample. In addition, the estimate of the electron-phonon coupling constant from quasiparticle relaxation rate in time domain gives a value of ~ 0.17 that is much too small to give a T_C of 25 K. The result agrees with the conclusion that the electron-phonon interaction is not strong enough to induce the SC transition in the iron-based superconductor as discussed in BFNA sample.

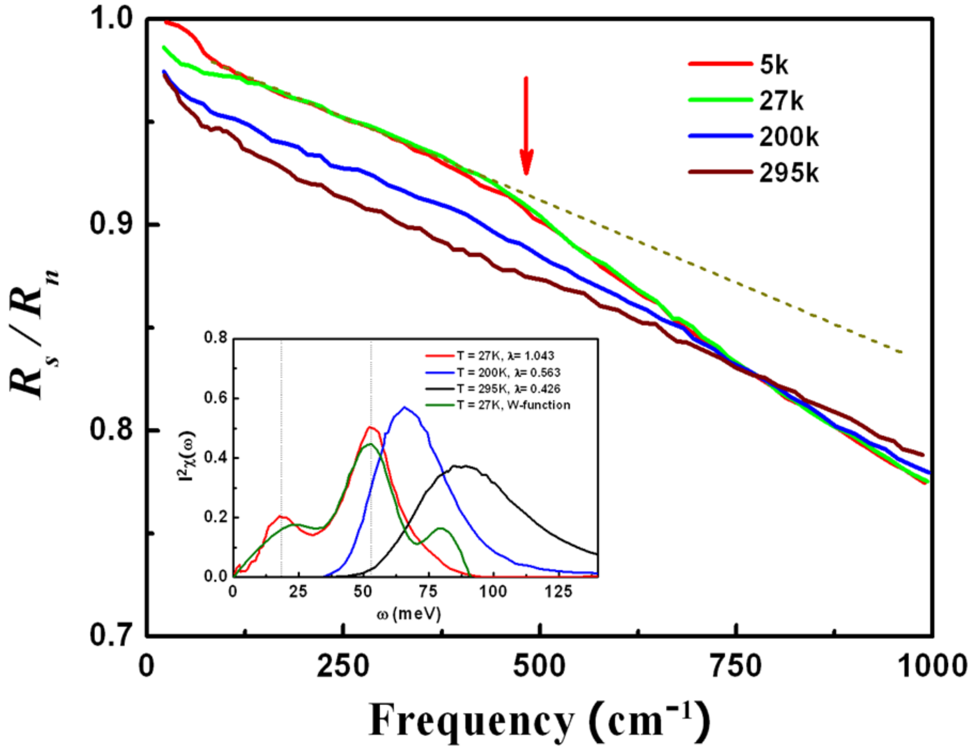

Fig. 7.5 Experimental R_s/R_n ratio at three temperatures together with BCS single gap and two-gap fits at 5 K. $T = 27$ K data is used for R_n .The inset shows the temperature dependent $I^2\chi(\omega)$, the inverted electron boson spectral function in $BaFe_{1.85}Co_{0.15}As_2$.

The conclusion is further verified by frequency domain measurements at Prof. Jiufeng Tu's group. We obtained the electron boson spectral function, referred to generically as $I^2\chi(\omega)$, by inverting the frequency dependent optical scattering rate based on Eliashberg theory [137]. The result for the normal state is shown in the inset of Fig. 7.5. $I^2\chi(\omega)$ has two peaks located at ~ 18.5 and ~ 53 meV at 27 K (just above T_C). It is important to point out that the deduced electron-boson spectral function, $I^2\chi(\omega)$, is strongly temperature dependent and contains significant contribution beyond the highest of phonon frequencies [138], and thereby it rules out electron phonon interaction as the dominant pairing mechanism in BFCA. In particular, the 18.5 meV peak in $I^2\chi(\omega)$ matches the spin resonance peak (12.5 − 17.5 meV) observed in $Ba_{0.6}K_{0.4}Fe_2As_2$ [139] and the 53 meV peak coincides with a spin wave peak in $CaFe_2As_2$ in inelastic neutron scattering [140], which indicates a spin origin for $I^2\chi(\omega)$. In fact, recent spin relaxation measurements on a number of iron pnictides show an antiferromagnetic energy scale of ~ 50 meV which is also theoretically predicted. Therefore, electron coupling to AF spin fluctuations provides a natural explanation for our experimental observations.

In summary, we investigated the QP relaxation dynamics in BFNA and BFCA by optical spectroscopy in both time and frequency domains. We reveal that the electron-doped BFNA and BFCA are multi-gap superconductors. Moreover, we show that electron pairing in BFNA and BFCA is unconventional and not dominated by electron phonon interaction based on our experimental results. From the frequency domain results, a spin mediated pairing mechanism is necessary to include for describing the SC phase transition in iron based superconductor.

Chapter 8 Summary

We used ferromagnetic resonance and time-resolved pump-probe optical techniques to study the spin and quasiparticle dynamics in the epitaxially grown iron thin films, multilayer FeCoB/Cr/FeCoB thin films, and iron based superconductors.

First, the FMR measurements were carried out to study the spin dynamics both in frequency and time domains in single layer iron thin film and FeCoB/Cr/FeCoB multilayer samples. In the single layer iron thin films, we employed magnetization precessions to characterize the magnetic crystalline anisotropies and magnetization damping. We reveal that the magnetic crystalline anisotropy is dominative and the magnetic damping shows a strong dependence of the in-plane magnetic field orientation. In the FeCoB/Cr/FeCoB multilayer thin films, we identified both the acoustic and optical spin wave modes and reveal that the adjacent magnetic layers in the trilayer structures are antiferromagnetic coupled with an effective interlayer coupling constant J_{eff}. Our investigations show that the magnetic anisotropy parameters and magnetic damping can be accurately tuned and controlled by the interlayer coupling constant J_{eff}.

Next, we utilized the time-resolved pump-probe magneto-optical MOKE spectroscopy to study the spin dynamics in the iron thin film at the picosecond time scale. We combined the time resolved MOKE results with static magnetic hysteresis loops at various time delays to understand the ultrafast demagnetization dynamics. The demagnetization relaxation time was estimated to be of ~ 70 *fs*. The demagnetization process is completed before electron-phonon equilibration is achieved and therefore the dynamics cannot be solely explained by the electron thermalization model. The spin-orbital coupling was included to explain our results. Moreover, we showed that the ultrafast magnetization reorientation can be coherently controlled by the pump polarizations. The magnetization excitation and reorientation is attributed to the laser pulse induced effective field in the sample.

Finally, the quasiparticle relaxation dynamics were studied in the $BaFe_{1.9}Ni_{0.1}As_2$ and $BaFe_{1.85}Co_{0.15}As_2$ superconductor using time-resolved pump-probe optical spectroscopy. Two distinct relaxation components and one sub-nanosecond long-lived component are observed in our transient reflectivity spectra. The picosecond scale relaxation component is attributed to the recombination of quasiparticles in the superconducting state. The sub picoseconds scale relaxation component is ascribed to the quasiparticle relaxation from a range of large gap states to the state above the superconducting gap. Our results support the multi-gap characteristics of the iron based superconductors. Furthermore, the electron-phonon coupling constant and the Coulomb pseudopotential are estimated from the quasiparticle relaxation lifetime. The negative Coulomb pseudopotential suggests that the electron-phonon interaction is not the dominative contribution of the SC transition in iron based superconductor. By combining the frequency domain measurement results, we conclude that it is necessary to combine the electron-phonon interaction and a spin mediated pairing mechanism to understand the SC phase transition in iron based superconductor.

References

[1] M. Yamaguchi, S. Arakawa, H. Ohzeki, Y. Hayashi, and K. I. Arai, "Characteristics and analysis of a thin film inductor with closed magnetic circuit structure," *IEEE Trans. Magn.* , vol. 28, p. 3015 1992.

[2] A. M. Crawford, D. Gardner, and S. X. Wang, "High-frequency microinductors with amorphous magnetic ground planes," *IEEE Trans. Magn.* , vol. 38, p. 3168 2002.

[3] B. Kuanr, Z. Celinski, and R. E. Camley, "Tunable high-frequency band-stop magnetic filters," *Appl. Phys. Lett.* , vol. 83, p. 3969 2003.

[4] B. Viala, A. S. Royet, R. Cuchet, M. Aid, P. Gaud, O. Valls, M. Ledieu, and O. Acher, "RF planar ferromagnetic inductors on silicon," *IEEE Trans. Magn.* , vol. 40, p. 1999 2004.

[5] B. Kuanr, D. L. Marvin, T. M. Christensen, R. E. Camley, and Z. Celinski, "High-frequency magnetic microstrip local bandpass filters," *Appl. Phys. Lett.* , vol. 87, p. 222506 2005.

[6] M. Gruyters and D. Riegel, "Strong exchange bias by a single layer of independent antiferromagnetic grains: The CoO/Co model system," *Phys. Rev.* ***B*** vol. 63, p. 052401 2000.

[7] M. Ali, C. H. Marrows, M. Al-Jawad, B. J. Hickey, A. Misra, U. Nowak, and K. D. Usadel, "Antiferromagnetic layer thickness dependence of the IrMn/Co exchange-bias system," *Phys. Rev.* ***B****,* vol. 68, p. 214420, Dec 2003.

[8] P. Blomqvist, K. M. Krishnan, and E. Girt, "Magnetization processes in exchange-biased MnPd/Fe bilayers," *J. Appl. Phys,* vol. 95, pp. 8487-8489, Jun 15

2004.

[9] Kohji Nakamura, A. J. Freeman, and S. W. D, "Magnetic structures at the ferromagnetic NiFe and antiferromagnetic NiMn interface in exchange-biased films: Role of noncollinear magnetism and roughness," *Phys. Rev.* ***B*** vol. 65, p. 012402 2001.

[10] S. M. Zhou and C. L. Chien, "Dependence of exchange coupling on magnetization in Co-Ni/FeMn bilayers," *Phys. Rev.* ***B,*** vol. 63, p. 104406, Mar 1 2001.

[11] S. X. Wang, N. X. Sun, M. Yamaguchi, and S. Yabukami, "Sandwich films - Properties of a new soft magnetic material," *Nature,* vol. 407, pp. 150-151, Sep 14 2000.

[12] Y. H. Ren, C. Wu, Y. Gong, C. Pettiford, and N. X. Sun, "Ultrafast optical study of spin wave resonance and relaxation in a CoFe/PtMn/CoFe trilayer film," *J. Appl. Phys,* vol. 105, p. 073910 Apr 1 2009.

[13] C. Bellouard, J. Faure-Vincent, C. Tiusan, F. Montaigne, M. Hehn, V. Leiner, H. Fritzsche, and M. Gierlings, "Interlayer magnetic coupling in Fe/MgO junctions characterized by vector magnetization measurements combined with polarized neutron reflectometry," *Phys. Rev.* ***B,*** vol. 78, p. 134429 Oct 2008.

[14] S. Blomeier, P. Candeloro, B. Hillebrands, B. Reuscher, A. Brodyanski, and M. Kopnarski, "Micromagnetism and magnetization reversal of embedded ferromagnetic elements," *Phys. Rev.* ***B,*** vol. 74, p. 184405 Nov 2006.

[15] Z. Celinski and B. Heinrich, "Exchange Coupling in Fe/Cu, Pd, Ag, Au/Fe Trilayers," *Journal of Magnetism and Magnetic Materials,* vol. 99, pp. L25-L30, Sep 1991.

[16] M. E. Filipkowski, J. J. Krebs, G. A. Prinz, and C. J. Gutierrez, "Giant near-90-Degrees Coupling in Epitaxial Cofe/Mn/Cofe Sandwich Structures," *Phys. Rev. Lett,* vol. 75, pp. 1847-1850, Aug 28 1995.

[17] W. E. Bailey, S. E. Russek, X. G. Zhang, and W. H. Butler, "Experimental separability of channeling giant magnetoresistance in Co/Cu/Co," *Phys. Rev.* ***B,*** vol. 72, p. 012409 Jul 2005.

[18] D. Tripathy, A. O. Adeyeye, and S. Shannigrahi, "Effect of spacer layer thickness on the magnetic and magnetotransport properties of $Fe_3O_4/Cu/Ni_{80}Fe_{20}$ spin valve structures," *Phys. Rev.* ***B,*** vol. 75, p. 012403 Jan 2007.

[19] P. M. Haney, D. Waldron, R. A. Duine, A. S. Nunez, H. Guo, and A. H. MacDonald, "Ab initio giant magnetoresistance and current-induced torques in Cr/Au/Cr multilayers," *Phys. Rev.* ***B,*** vol. 75, p. 174428 May 2007.

[20] S. M. Valvidares, T. Schroeder, O. Robach, C. Quirós, T.-L. Lee, and S. Ferrer, "Structural and magnetic properties of bcc Co films on Pt(001) studied by magnetic resonant surface x-ray diffraction, STM, and magneto-optical Kerr effect," *Phys. Rev.* ***B,*** vol. 70, p. 224413 2004.

[21] N. Planckaert, C. L'abbe, B. Croonenborghs, R. Callens, B. Laenens, A. Vantomme, and J. Meersschaut, "Spin dynamics in the spacer of an interlayer-coupled Fe/Fe0.57Si0.43/Fe trilayer probed with nuclear resonant scattering of synchrotron radiation," *Phys. Rev.* ***B,*** vol. 78, p. 144424 Oct 2008.

[22] B. Heinrich, Y. Tserkovnyak, G. Woltersdorf, A. Brataas, R. Urban, and G. E. W. Bauer, "Dynamic exchange coupling in magnetic bilayers," *Phys. Rev. Lett,* vol. 90, p.

187601 May 9 2003.

[23] B. Heinrich, Z. Celinski, J. F. Cochran, W. B. Muir, J. Rudd, Q. M. Zhong, A. S. Arrott, K. Myrtle, and J. Kirschner, "Ferromagnetic and Antiferromagnetic Exchange Coupling in Bcc Epitaxial Ultrathin Fe(001)/Cu(001)/Fe(001) Trilayers," *Phys. Rev. Lett,* vol. 64, pp. 673-676, Feb 5 1990.

[24] J. J. Kerbs, P. Lubitz, A. Chaiken, and G. A. Prinz, "Magnetic resonance determination of the antiferromagnetic coupling of Fe layers through Cr," *Phys. Rev. Lett. ,* vol. 63, p. 1645 1989.

[25] A. Brambilla, P. Biagioni, M. Portalupi, M. Zani, M. Finazzi, L. Duo, P. Vavassori, R. Bertacco, and F. Ciccacci, "Magnetization reversal properties of Fe/NiO/Fe(001) trilayers," *Phys. Rev.* ***B,*** vol. 72, p. 174402 Nov 2005.

[26] T. J. Klemmer, K. A. Ellis, L. H. Chen, B. van Dover, and S. Jin, "Ultrahigh frequency permeability of sputtered Fe-Co-B thin films," *J. Appl. Phys,* vol. 87, pp. 830-833, Jan 15 2000.

[27] C. H. Back, R. Allenspach, W. Weber, S. S. P. Parkin, D. Weller, E. L. Garwin, and H. C. Siegmann, "Minimum Field Strength in Precessional Magnetization Reversal," *Science,* vol. 285, p. 864, 1999.

[28] S. Kaka and S. E. Russek, "Precessional switching of submicrometer spin valves," *Appl. Phys. Lett. ,* vol. 80, p. 2958, 2002.

[29] T. Devolder, A. Tulapurkar, Y. Suzuki, C. Chappert, P. Crozat, and K. Yagami, "Temperature study of the spin-transfer switching speed from dc to 100 ps," *J. Appl. Phys. ,* vol. 98, p. 053904, 2005.

[30] Y. Acremann, J. P. Strachan, V. Chembrolu, S. D. Andrews, T. Tyliszczak, J. A. Katine, M. J. Carey, B. M. Clemens, H. C. Siegmann, and J. Stöhr, "Time-Resolved Imaging of Spin Transfer Switching: Beyond the Macrospin Concept," *Phys. Rev. Lett.,* vol. 96, p. 217202, 2006.

[31] E. Beaurepaire, J. C. Merle, A. Daunois, and J. Y. Bigot, "Ultrafast Spin Dynamics in Ferromagnetic Nickel," *Phys. Rev. Lett.,* vol. 76, p. 4250, 1996.

[32] J. Hohlfeld, E. Matthias, R. Knorren, and K. H. Bennemann, "Nonequilibrium magnetization dynamics of nickel " *Phys. Rev. Lett.,* vol. 78, p. 4861, 1997.

[33] B. Koopmans, M. van Kampen, J. T. Kohlhepp, and W. J. M. de Jonge, "Ultrafast Magneto-Optics in Nickel: Magnetism or Optics?," *Phys. Rev. Lett.* , p. 844, 2000.

[34] A. V. Kimel, A. Kirilyuk, F. Hansteen, R. V. Pisarev, and Th. Rasing, "Nonthermal optical control of magnetism and ultrafast laser-induced spin dynamics in solids," *J. Phys.: Condens. Matter,* vol. 19, p. 043201, 2007.

[35] K. Vahaplar, A. M. Kalashnikova, A.V. Kimel, D. Hinzke, U. Nowak, R. Chantrell, A. Tsukamoto, A. Itoh, A. Kirilyuk, and Th. Rasing, "Ultrafast Path for Optical Magnetization Reversal via a Strongly Nonequilibrium State," *Phys. Rev. Lett.* , vol. 103, p. 117201, 2009.

[36] J. Shah and U. S. o. S. a. S. Nanostructures, "Ultrafast Spectroscopy of Semiconductors and Semiconductor Nanostructures," *Springer Series in Solid-State Sciences (Springer, Berlin),* vol. 115, 1996.

[37] F. Hansteen, A. V. Kimel, A. Kirilyuk, and Th. Rasing, "Femtosecond Photomagnetic Switching of Spins in Ferrimagnetic Garnet Films," *Phys. Rev. Lett.,* vol. 95, p.

047402, 2005.

[38] Q. Zhang, A. V. Nurmikko, A. Anguelouch, G. Xiao, and A. Gupta, "Coherent Magnetization Rotation and Phase Control by Ultrashort Optical Pulses in CrO_2 Thin Films," *Phys. Rev. Lett.,* vol. 89, p. 177402, 2002.

[39] C. D. Stanciu, F. Hansteen, A. V. Kimel, A. Kirilyuk, A. Tsukamoto, A. Itoh, and Th. Rasing, "All-Optical Magnetic Recording with Circularly Polarized Light," *Phys. Rev. Lett. ,* vol. 99, p. 047601, 2007.

[40] A. V. Kimel, A. Kirilyuk, P. A. Usachev, R. V. Pisarev, A. M. Balbashov, and Th. Rasing, "Ultrafast non-thermal control of magnetization by instantaneous photomagnetic pulses," *Nature (London)* vol. 435, p. 655, 2005.

[41] Y. Kamihara, T. Watanabe, M. Hirano, and H. Hosono, "Iron-based layered superconductor La[O1-xFx]FeAs (x=0.05-0.12) with T-c=26 K," *Journal of the American Chemical Society,* vol. 130, pp. 3296-3297, Mar 19 2008.

[42] S. L. B. N. Ni, A. Kreyssig, S. Nandi, G. E. Rustan, A. I. Goldman, S. Gupta, J. D. Corbett, A. Kracher, and P. C. Canfield, "Anisotropic thermodynamic and transport properties of single-crystalline $Ba_{1-x}K_xFe_2As_2$ (x=0 and 0.45)," *Phys. Rev.* ***B,*** vol. 78, p. 014507, 2008.

[43] G. Wu, R. H. Liu, H. Chen, Y. J. Yan, T. Wu, Y. L. Xie, J. J. Ying, X. F. Wang, D. F. Fang, and X. H. Chen, "Transport properties and superconductivity in $Ba_{1-x}M_xFe_2As_2$ (M=La and K) with double FeAs layers," *Europhys. Lett.,* vol. 84, p. 27010, 2008.

[44] S. X. Chi, A. Schneidewind, J. Zhao, L. W. Harriger, L. J. Li, Y. K. Luo, G. H. Cao, Z. A. Xu, M. Loewenhaupt, J. P. Hu, and P. C. Dai, "Inelastic Neutron-Scattering

Measurements of a Three-Dimensional Spin Resonance in the FeAs-Based BaFe1.9Ni0.1As2 Superconductor," *Physical Review Letters,* vol. 102, p. 107006, Mar 13 2009.

[45] M. R. Norman, "High-temperature superconductivity in the iron pnictides," *Physics,* vol. 1, 2008.

[46] M. Tortello, D. Daghero, G. A. Ummarino, V. A. Stepanov, J. Jiang, J. D. Weiss, E. E. Hellstrom, and R. S. Gonnelli, "Multigap Superconductivity and Strong Electron-Boson Coupling in Fe-Based Superconductors: A Point-Contact Andreev-Reflection Study of $Ba(Fe_{1-x}Co_x)_2As_2$ Single Crystals," *Phys. Rev. Lett.,* vol. 105, p. 237002 2010.

[47] K. Hashimoto, T. Shibauchi, T. Kato, K. Ikada, R. Okazaki, H. Shishido, M. Ishikado, H. Kito, A. Iyo, H. Eisaki, S. Shamoto, and Y. Matsuda, "Microwave penetration depth and quasiparticle conductivity of PrFeAsO1-y single crystals: evidence for a full-gap superconductor," *Phys. Rev. Lett.* , vol. 102, p. 017002 2009.

[48] M. Rotter, M. Tegel, and D. Johrendt, *arXiv:0805.4630.,* 2008.

[49] M. Rotter, M. Tegel, and D. Johrendt, "Superconductivity at 38 K in the Iron Arsenide $(Ba_{1-x}K_x)Fe_2As_2$," *Phys. Rev. Lett.,* vol. 101, p. 107006 2008.

[50] R. J. McQueeney, Y. Petrov, T. Egami, M. Yethiraj, G. Shirane, and Y. Endoh, "Anomalous dispersion of LO phonons in La1.85Sr0.15CuO4 at low temperatures," *Physical Review Letters,* vol. 82, pp. 628-631, Jan 18 1999.

[51] L. J. Li, Y. K. Luo, Q. B. Wang, H. Chen, Z. Ren, Q. Tao, Y. K. Li, X. Lin, M. He, Z. W. Zhu, G. H. Cao, and Z. A. Xu, "Superconductivity induced by Ni doping in

BaFe2As2 single crystals," *New Journal of Physics,* vol. 11, p. 025008, Feb 27 2009.

[52] A. Lanzara, P. V. Bogdanov, X. J. Zhou, S. A. Kellar, D. L. Feng, E. D. Lu, T. Yoshida, H. Eisaki, A. Fujimori, K. Kishio, J. I. Shimoyama, T. Noda, S. Uchida, Z. Hussain, and Z. X. Shen, "Evidence for ubiquitous strong electron-phonon coupling in high-temperature superconductors," *Nature,* vol. 412, pp. 510-514, Aug 2 2001.

[53] J. Rossat-Mignodi, L. P. Regnault, C. Velqqer, P. Bourges, P. Burlet, J. Bossy, J. Y. Henry, and G. Lapertot, "Neutron Scattering Study of The $YBa_2Cu_3O_{6+x}$ System," *Physica C* vol. 86, p. 185, 1991.

[54] M. R. Norman, H. Ding, J. C. Campuzano, T. Takeuchi, M. Randeria, T. Yokoya, T. Takahashi, T. Mochiku, and K. Kadowaki, "Unusual dispersion and line shape of the superconducting state spectra of Bi2Sr2CaCu2O8+delta," *Phys. Rev. Letts,* vol. 79, pp. 3506-3509, Nov 3 1997.

[55] S. G. Han, Z. V. Vardeny, K. S. Wong, O. G. Symko, and G. Koren, "Femtosecond Optical-Detection of Quasi-Particle Dynamics in High-Tc Yba2cu3o7-Delta Superconducting Thin-Films," *Phys. Rev. Letts,* vol. 65, pp. 2708-2711, Nov 19 1990.

[56] C. J. Stevens, D. Smith, C. Chen, J. F. Ryan, B. Podobnik, D. Mihailovic, G. A. Wagner, and J. E. Evetts, "Evidence for two-component high-temperature superconductivity in the femtosecond optical response of YBa2Cu3O7-delta," *Phys. Rev. Letts,* vol. 78, pp. 2212-2215, Mar 17 1997.

[57] D. C. Smith, P. Gay, C. J. Stevens, C. Chen, G. Yang, S. J. Abell, D. Z. Wang, J. H. Wang, Z. F. Ren, and J. F. Ryan, "Femtosecond Dynamics of BSCCO-2212 in the weak and strong excitatin limit," *Physica C* vol. 341, p. 2221, 2000.

[58] R. D. Averitt, G. Rodriguez, A. I. Lobad, J. L. W. Siders, S. A. Trugman, and A. J. Taylor, "Nonequilibrium superconductivity and quasiparticle dynamics in YBa2Cu3O7-delta," *Phys.Rev* ***B,*** vol. 6314, p. 140502(R), Apr 1 2001.

[59] M. L. Schneider, J. Demsar, Y. Glinka, A. Klimov, A. Krapf, S. Rast, Y. H. Ren, W. D. Si, Y. Xu, X. H. Zeng, I. Bozovic, G. Lupke, R. Manzke, R. Sobolewski, A. T. Taylor, N. H. Tolk, X. X. Xi, R. Joynt, and M. Onellion, "Ultrafast carrier relaxation dynamics in single-layer cuprates," *Europhysics Letters,* vol. 60, pp. 460-466, Nov 2002.

[60] V. V. Kabanov, J. Demsar, B. Podobnik, and D. Mihailovic, "Quasiparticle relaxation dynamics in superconductors with different gap structures: Theory and experiments on $YBa_2Cu_3O_7$-delta," *Phys. Rev.* ***B,*** vol. 59, pp. 1497-1506, Jan 1 1999.

[61] E. E. M. Chia, J. X. Zhu, D. Talbayev, R. D. Averitt, A. J. Taylor, K. H. Oh, I. S. Jo, and S. I. Lee, "Observation of competing order in a High-T_c superconductor using femtosecond optical pulses," *Phys. Rev. Letts,* vol. 99, p. 147008, Oct 5 2007.

[62] E. E. M. Chia, D. Talbayev, J. X. Zhu, H. Q. Yuan, T. Park, J. D. Thompson, C. Panagopoulos, G. F. Chen, J. L. Luo, N. L. Wang, and A. J. Taylor, "Ultrafast Pump-Probe Study of Phase Separation and Competing Orders in the Underdoped (Ba, K)Fe2As2 Superconductor," *Phys. Rev. Letts,* vol. 104, p. 027003, Jan 15 2010.

[63] L. Landau and E. Lifshitz, "On the Theory of the Dispersion of Magnetic Permeability in Ferromagnetic Bodies," *PhyS. Z. Sowjetunion.,* vol. 8, pp. 153-169, 1935.

[64] T. L. Gilbert, "A Lagrangian Formulation of the Gyromagnetic Equation of the Magnetization Field," *Phys. Rev. ,* vol. 100, p. 1243 1955.

[65] T. L. Gilbert, "A phenomenological Theory of Damping in Ferromagnetic Materials," *IEEE Trans. Mag.,* vol. 40, p. 3443 2004.

[66] J. Smit and H.G. Beljers, "Ferromagnetic resonance absorption in $BaFe_{12}O_{19}$, a high anisotropy crystal," *Philips Res. Rep. ,* vol. 10, p. 113, 1955.

[67] J. Lindner and K. Baberschke, "Ferromagnetic resonance in coupled ultrathin films," *Journal of Physics-Condensed Matter,* vol. 15, pp. S465-S478, Feb 12 2003.

[68] T. E. Stevens, J. Kuhl, and R. Merlin, "Coherent phonon generation and the two stimulated Raman tensors," *Phys. Rev.* ***B****,* vol. 65, p. 144304 2002.

[69] W. Hayes and R. Loudon, "Scattering of Light by Crystals," *(Wiley, New York, 1978).*

[70] B. Koopmans, J. J. M. Ruigrok, F. Dalla Longa, and W. J. M. de Jonge, "Unifying Ultrafast Magnetization Dynamics," *Phys. Rev. Lett.,* vol. 95, p. 267207 2005.

[71] Y. Yafet, vol. in Solid State Physics, edited by F. Seit and D. Turnbull (Academic, New York, 1963), Vol. 14, pp. 1-98.

[72] B. Koopmans, G. Malinowski, F. D. Longa, D. Steiauf, M. Faehnle, T. Roth, M. Cinchetti, and M. Aeschlimann, "Explaining the paradoxical diversity of ultrafast laser-induced demagnetization," *Nature Materials,* vol. 9, pp. 259-265, Mar 2010.

[73] G. P. Zhang and W. Hubner, "Laser-induced ultrafast demagnetization in ferromagnetic metals," *Phys Rev Lett,* vol. 85, pp. 3025-3028, Oct 2 2000.

[74] G. P. Zhang, W. Hubner, E. Beaurepaire, and J. Y. Bigot, "Laser-induced ultrafast demagnetization: Femtomagnetism, a new frontier?," *Spin Dynamics in Confined Magnetic Structures I,* vol. 83, pp. 245-288, 2002.

[75] G. P. Zhang, "Microscopic theory of ultrafast spin linear reversal," *J. Phys.: Condens.*

Matter., vol. 23 p. 206005 2011.

[76] S. G. Han, Z. V. Vardeny, K. S. Wong, O. G. Symko, and G. Koren, "Femtosecond optical detection of quasiparticle dynamics in High-T_c $YBa_2Cu_3O_{7-x}$ superconducting thin films," *Phys.Rev.Lett,* vol. 65, p. 2708 1990.

[77] J. M. Chwalek, C. Uher, J. F. Whitaker, G. A. Mourou, J. Agnostinelli, and M. Lelental, "Femtosecond optical absorption studies of nonequilibrium electronic prosesses in high T_c superconductors," *Appl. Phys. Lett.,* vol. 57, p. 1696 1990.

[78] G. L. Eesley, J. Heremans, M. S. Meyer, G. L. Doll, and S. H. Liou, "Relaxation Time of the Order Parameter in a High-Temperature Superconductor," *Phys. Rev. Lett.,* vol. 65, p. 3445 1990.

[79] V. V. Kabanov, J. Demsar, B. Podobnik, and D. Mihailovic, "Quasiparticle relaxation dynamics in superconductors with different gap structures: Theory and experiments on $YBa_2Cu_3O_{7-x}$," *Phys. Rev. Lett.,* vol. 59, p. 1497, 1999.

[80] A. G. Aronov, M. A. Zelikman, and B. Z. Spivak, "Properties of superconductors with nonequilibrium excitations," *Sov. Phys. Solid State,* vol. 18, p. 1286 1976.

[81] A. G. Aronov and B. Z. Spivak, "Nonequilibrium distribution in superconductors," *J. Low Temp. Phys. ,* vol. 29, p. 149, 1977.

[82] J. M. Ziman, "Electrons and Phonons," *(Oxford University Press, London, 1960).*

[83] O. Madelung, "Introduction to Solid State Theory," *(Springer Verlag, Berlin, 1978).*

[84] P. B. Allen, "Theory of thermal relaxation of electrons in metals," *Phys. Rev. Lett.,* vol. 59, p. 1460, 1987.

[85] E. M. Kneedler, B. T. Jonker, P. M. Thibado, R. J. Wagner, B. V. Shanabrook, and L. J.

Whitman, "Influence of substrate surface reconstruction on the growth and magnetic properties of Fe on GaAs(001)," *Phys. Rev. B,* vol. 56, 1997.

[86] J. J. Krebs, B. T. Jonker, and G. A. Prinz, "Properties of Fe single‐crystal films grown on (100) GaAs by molecular‐beam epitaxy," *J. Appl. Phys.,* vol. 61, p. 2596, 1987.

[87] M. Gester, C. Daboo, R. J. Hicken, S. J. Gray, A. Ercole, and J. A. C.Bland, . "Continuous evolution of the in‐plane magnetic anisotropies with thickness in epitaxial Fe films," *J. Appl. Phys.,* vol. 80, p. 347 1996.

[88] M. Zolfl, M. Brockmann, M. Kohler, S. Kreuzer, T. Schweinbock, S. Miethaner, F. Bensch, and G. Bayreuther, "Magnetic films epitaxially grown on semiconductors," *J. Magn. Magn. Mater.* , vol. 175, p. 16, 1997.

[89] O. Thomas, Q. Shen, P. Schieffer, N. Tournerie, and B. Lépine, "Interplay between Anisotropic Strain Relaxation and Uniaxial Interface Magnetic Anisotropy in Epitaxial Fe Films on (001) GaAs," *Phys. Rev. Lett.* , vol. 90, 2003.

[90] C. Wang, Y. K. Li, Z. W. Zhu, S. Jiang, X. Lin, Y. K. Luo, S. Chi, L. J. Li, Z. Ren, M. He, H. Chen, Y. T. Wang, Q. Tao, G. H. Cao, and Z. A. Xu, "Effects of cobalt doping and phase diagrams of LFe1−xCoxAsO (L=La and Sm)," *Phys. Rev.* ***B,*** vol. 79, p. 054521, 2009.

[91] Y. Kamihara, T. Watanabe, M. Hirano, and H. Hosono, "Iron-Based Layered Superconductor La[$O_{1-x}F_x$]FeAs (x = 0.05 - 0.12) with Tc = 26 K," *J. Am. Chem. Soc.* , vol. 130, p. 3296 2008.

[92] M. Rotter, M. Tegel, D. Johrendt, I. Schellenberg, W. Hermes, and R. Pöttgen,

"Spin-density-wave anomaly at 140 K in the ternary iron arsenide $BaFe_2As_2$," *Phys. Rev.* ***B**,* vol. 78, p. 020503(R), 2008.

[93] C. de la Cruz, Q. Huang, J. W. Lynn, J. Li, W. Ratcliff II, J. L. Zarestky, H. A. Mook, G. F. Chen, J. L. Luo, N. L. Wang, and P. Dai, "Magnetic order close to superconductivity in the iron-based layered $LaO_{1-x}F_xFeAs$ systems," *Nature (London),* vol. 453, p. 899 2008.

[94] J. H. E. Griffiths, "Anomalous High-Frequency Reistance of Ferromagnetic Metals," *Nature,* vol. 158, pp. 670-671, 1946.

[95] C. Kittel, "Interpretation of Anomalous Larmor Frequencies in Ferromagnetic Resonance Experiment," *Phys. Rev.,* vol. 71, pp. 270-271, 1947.

[96] *Tsunami Manual, Spectra-Physics*.

[97] E. Šimánek and B. Heinrich, "Gilbert damping in magnetic multilayers," *Phys. Rev.* ***B*** vol. 67, p. 144418 2003.

[98] D. Talbayev, H. Zhao, G. Lüpke, A. Venimadhav, and Q. Li, "Photoinduced coherent magnetization precession in epitaxial $La_{0.67}Ca_{0.33}MnO_3$ films," *Phys. Rev.* ***B*** vol. 73, p. 014417 2006.

[99] L. Landau and E. Lifshitz, "On the Theory of the Dispersion of Magnetic Permeability in Ferromagnetic Bodies," *Phys. Z. Sowjetunion,* vol. 8, 1935.

[100] S. Mizukami, E. P. Sajitha, D. Watanabe, F. Wu, T. Miyazaki, H. Naganuma, M. Oogane, and Y. Ando, "Gilbert damping in perpendicularly magnetized Pt/Co/Pt films investigated by all-optical pump-probe technique," *Appl. Phys. Lett.,* vol. 96, p. 152502 2010.

[101] J. Nogues, C. Leighton, and I. K. Schuller, "Correlation between antiferromagnetic interface coupling and positive exchange bias," *Phys. Rev.* ***B,*** vol. 61, pp. 1315-1317, Jan 1 2000.

[102] P. Bruno, "Theory of Interlayer Magnetic Coupling," *Phys. Rev.* ***B,*** vol. 52, pp. 411-439, Jul 1 1995.

[103] H. Suhl, "Ferromagnetic Resonance in Nickel Ferrite between One Kilomegacycle and 2 Kilomegacycles," *Physical Review,* vol. 97, pp. 555-557, 1955.

[104] R. Urban, G. Woltersdorf, and B. Heinrich, "Gilbert damping in single and multilayer ultrathin films: Role of interfaces in nonlocal spin dynamics," *Phys Rev Lett,* vol. 87, p. 217204 Nov 19 2001.

[105] B. C. Choi, M. Belov, W. K. Hiebert, G. E. Ballentine, and M. R. Freeman, "Ultrafast Magnetization Reversal Dynamics Investigated by Time Domain Imaging," *Phys. Rev. Lett.,* vol. 86, p. 728, 2001.

[106] Th. Gerrits, H. A. M. van den Berg, J. Hohlfeld, L. Bär, and Th. Rasing, "Ultrafast precessional magnetization reversal by picosecond magnetic field pulse shaping," *Nature (London)* vol. 418, p. 509, 2002.

[107] I. Tudosa, C. Stamm, A. B. Kashuba, F. King, H. C. Siegmann, J. Stöhr, G. Ju, B. Lu, and D. Weller, "The ultimate speed of magnetic switching in granular recording media," *Nature (London)* vol. 428, p. 831, 2004.

[108] U. Bovensiepen, "Coherent and incoherent excitations of the Gd(0001) surface on ultrafast timescales," *J. Phys.: Condens. Matter* vol. 19, p. 083201, 2007.

[109] J. Wang, C. Sun, Y. Hashimoto, J. Kono, G. A. Khodaparast, L. Cywin´ ski, L. J.

Sham, G. D. Sanders, C. J. Stanton, and H. Munekata, "Ultrafast magneto-optics in ferromagnetic III–V semiconductors," *J. Phys.: Condens. Matter,* vol. 18, p. R501, 2006.

[110] A. Kirilyuk, A. V. Kimel, F. Hansteen, R. V. Pisarev, and Th. Rasing, "Ultrafast all-optical control of the magnetization in magnetic dielectrics," *Low Temp. Phys.,* vol. 32, p. 748, 2006.

[111] A. Scholl, L. Baumgarten, R. Jacquemin, and W. Eberhardt, "Ultrafast Spin Dynamics of Ferromagnetic Thin Films Observed by fs Spin-Resolved Two-Photon Photoemission," *Phys. Rev. Lett.,* vol. 79, p. 5146, 1997

[112] B. Koopmans, M. van Kampen, J. T. Kohlhepp, and W. J. M. de Jonge, "Ultrafast Magneto-Optics in Nickel: Magnetism or Optics?," *Phys. Rev. Lett. ,* vol. 85, p. 844 2000.

[113] H. Regensburger, R. Vollmer, and J. Kirschner, "Time-resolved magnetization-induced second-harmonic generation from the Ni(110) surface," *Phys. Rev.* ***B****,* vol. 61, p. 14716 2000.

[114] L. Guidoni, E. Beaurepaire, and J.-Y. Bigot, "Magneto-optics in the ultrafast regime: thermalization of spin populations in ferromagnetic films, ," *Phys. Rev. Lett. ,* vol. 89, p. 017401 2002.

[115] F. Hansteen, A. Kimel, A. Kirilyuk, and T. Rasing, "Femtosecond Photomagnetic Switching of Spins in Ferrimagnetic Garnet Films," *Phys. Rev. Lett. ,* vol. 95, p. 047402 2005.

[116] G. P. Zhang, "Laser-Induced Orbital and Spin Excitations in Ferromagnets: Insights

from a Two-Level System," *Phys. Rev. Lett.* , vol. 101, p. 187203 2008.

[117] D. Awschalom and N. Samarth, "Trend: Spintronics without magnetism," *Physics* vol. 2, p. 50, 2009.

[118] J. Fabian, A. Matos-Abiague, C. Ertler, P. Stano, and I. Zutic, "Semiconductor Spintronics " *Acta Phys. Slovaca,* vol. 57, p. 565 2007.

[119] E. Beaurepaire, J. C. Merle, A. Daunois, and J. Y. Bigot, "Ultrafast Spin Dynamics in Ferromagnetic Nickel," *Phys. Rev. Lett.,* vol. 76, pp. 4250–4253, 1996.

[120] T. Roth, D. Steil, D. Hoffmann, M. Bauer, M. Cinchetti, and M. Aeschlimann, "Dynamics of the coercivity in ultrafast pump–probe experiments " *J. Phys. D: Appl. Phys.,* vol. 41, p. 164006, 2008

[121] J.-Y. Bigot, M. Vomir, L.H.F. Andrade, and E. Beaurepaire, "Ultrafast magnetization dynamics in ferromagnetic cobalt: The role of the anisotropy," *Chem. Phys.,* vol. 318, pp. 137-146, 2005.

[122] G. P. Zhang, W. Hubner, G. Lefkidis, Y. H. Bai, and T. F. George, "Paradigm of the time-resolved magneto-optical Kerr effect for femtosecond magnetism," *Nature Physics,* vol. 5, pp. 499-502 2009.

[123] M. S. Si and G. P. Zhang, "Resolving photon-shortage mystery in femtosecond magnetism," *J. Phys.: Condens. Matter* vol. 22, pp. 076005-076022, 2010.

[124] A. Vernes, I. Reichl, P. Weinberger, L. Szunyogh, and C. Sommers, "Longitudinal Kerr effect in ultrathin Fe films on Pd(100)," *Phys. Rev.* ***B,*** vol. 70, p. 195407 2004.

[125] B. Koopmans, H. H. J. E. Kicken, M. van Kampen, and W. J. M. de Jonge, "Microscopic model for femtosecond magnetization dynamics," *J.M.M.M,* vol. 286, p.

271, 2005.

[126] G. P. Zhang, "Simple explanations for the laser-induced magnetization change in magnetic nanostructures (to be published)."

[127] I. I. Mazin, D. J. Singh, M. D. Johannes, and M. H. Du, "Unconventional superconductivity with a sign reversal in the order parameter of $LaFeAsO_{1-x} F_x$," *Phys. Rev. Lett.,* vol. 101, p. 57003 2008.

[128] T. A. Maier and D. J. Scalapino, "Theory of neutron scattering as a probe of the superconducting gap in the iron pnictides," *Phys. Rev.* ***B*** vol. 78, p. 020514 2008.

[129] A. V. Chubukov, D. V. Efremov, and I. Eremin, "Magnetism, superconductivity and pairing symmetry in iron-based superconductors," *Phys. Rev.* ***B,*** vol. 78, p. 134512, 2008.

[130] T. Y. Chen, Z. Tesanovic, R. H. Liu, X. H. Chen, and C. L. Chien, "A BCS-like gap in the superconductor $SmFeAsO_{0.85} F_{0.15}$," *Nature,* vol. 453, p. 1224, 2008.

[131] T. Mertelj, V. V. Kabanov, C. Gadermaier, N. D. Zhigadlo, S. Katrych, J. Karpinski, and D. Mihailovic, "Distinct Pseudogap and Quasiparticle Relaxation Dynamics in the Superconducting State of Nearly Optimally Doped $SmFeAsO_{0.8}F_{0.2}$ Single Crystals," *Phys. Rev. Lett.,* vol. 102, p. 117002 2009.

[132] S. D. Brorson, A. Kazeroonian, J. S. Moodera, D. W. Face, T. K. Cheng, E. P. Ippen, M. S. Dresselhaus, and G. Dresselhaus, "Femtosecond Room-Temperature Measurement of the Electron-Phonon Coupling Constant-Lambda in Metallic Superconductors," *Phys. Rev. Lett.,* vol. 64, pp. 2172-2175, Apr 30 1990.

[133] F. Hardy, T. Wolf, R. A. Fisher, R. Eder, P. Schweiss, P. Adelmann, H. von Lohneysen,

and C. Meingast, "Calorimetric evidence of multiband superconductivity in $Ba(Fe_{0.925}Co_{0.075})_2As_2$ single crystals," *Phys. Rev.* ***B,*** vol. 81, p. 060501, Feb 2010.

[134] B. Mansart, D. Boschetto, A. Savoia, F. Rullier-Albenque, F. Bouquet, E. Papalazarou, A. Forget, D. Colson, A. Rousse, and M. Marsi, "Ultrafast transient response and electron-phonon coupling in the iron-pnictide superconductor $Ba(Fe_{1-x}Co_x)_2As_2$," *Phys. Rev.* ***B,*** vol. 82, p. 024513, 2010.

[135] W. L. Mcmillan, "Transition Temperature of Strong-Coupled Superconductors," *Phys. Rev.,* vol. 167, p. 331, 1968.

[136] C. Kant, J. Deisenhofer, T. Rudolf, F. Mayr, F. Schrettle, A. Loidl, V. Gnezdilov, D. Wulferding, P. Lemmens, and V. Tsurkan, "Optical phonons, spin correlations, and spin-phonon coupling in the frustrated pyrochlore magnets $CdCr_2O_4$ and $ZnCr_2O_4$," *Phys. Rev.* ***B,*** vol. 80, p. 014529, Dec 2009.

[137] E. Schachinger, J. J. Tu, and J. P. Carbotte, "Angle-resolved photoemission spectroscopy and optical renormalizations: Phonons or spin fluctuations," *Phys. Rev.* ***B,*** vol. 67, p. 214508 2003.

[138] Note. The 53 meV peak falls outside the range of phonon energies and indicates the electron-boson coupling is due to non-phononic excitations.

[139] A. D. Christianson, E. A. Goremychkin, R. Osborn, S. Rosenkranz, M. D. Lumsden, C. D. Malliakas, I. S. Todorov, H. Claus, D. Y. Chung, M. G. Kanatzidis, R. I. Bewley, and T. Guidi, "Unconventional superconductivity in $Ba_{0.6}K_{0.4}Fe_2As_2$ from inelastic neutron scattering," *Nature* vol. 456, p. 930 2008.

[140] S. O. Diallo, V. P. Antropov, T. G. Perring, C. Broholm, J. J. Pulikkotil, N. Ni, S. L.

Bud'ko, P. C. Canfield, A. Kreyssig, A. I. Goldman, and R. J. McQueeney, "Itinerant Magnetic Excitations in Antiferromagnetic $CaFe_2As_2$," *Phys. Rev. Lett.* , vol. 102, p. 187206 2009.